Structural, magnetic, and electronic properties of electrodeposited Co and Fe based Heusler alloy films

A thesis submitted in partial fulfillment of the requirement for the award of the degree of

Doctor of Philosophy in Physics

By

Pushpesh Pathak

Under the supervision of

Prof. A. Srinivasan

Department of Physics

Indian Institute of Technology Guwahati

Guwahati – 781039, India

August 2025

Dedicated to my Parents and Teachers

Declaration statement

I, Pushpesh Pathak, hereby declare that the research work presented in the thesis, entitled "**Structural, magnetic, and electronic properties of electrodeposited Co and Fe based Heusler alloy films**" has been carried out by me under the supervision of Prof. A. Srinivasan, at the Department of Physics, Indian Institute of Technology Guwahati. I further confirm that no part of this work has been submitted elsewhere for the award of any other degree/diploma or any other academic award.

6th August 2025

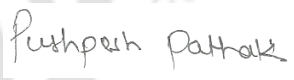

Pushpesh Pathak
Roll No.: 186121019
Department of Physics
Indian Institute of Technology Guwahati
Guwahati – 781039, India

Certificate

It is certified that the work contained in the thesis entitled "**Structural, magnetic, and electronic properties of electrodeposited Co and Fe based Heusler alloy films**" submitted by Pushpesh Pathak (Roll No. 186121019), a Ph.D. student of the Department of Physics, Indian Institute of Technology Guwahati for the award of the degree of Doctor of Philosophy has been carried out under the supervision of Prof. A. Srinivasan. This work has not been submitted elsewhere for the award of any degree.

6th August 2025

Prof. A. Srinivasan
Professor
Department of Physics
Indian Institute of Technology Guwahati
Guwahati – 781039, India

Acknowledgments

Looking back, I am overwhelmed with profound gratitude to all those who have played a vital role in helping me reach this significant milestone in my academic journey.

First and foremost, I express my deepest gratitude to my supervisor, Prof. A. Srinivasan, for his exceptional mentorship, unwavering support, and inspiring guidance throughout my Ph.D. His encouragement for open discussions and intellectual debates nurtured my curiosity and laid the foundation for developing a scientific mindset. His insightful advice, innovative ideas, and broad academic vision profoundly expanded my understanding of the subject. I am especially grateful for the academic freedom he provided, which allowed me to express my thoughts and pursue my ideas independently. His faith in my abilities and the autonomy he granted played a crucial role in shaping me from a research scholar into an independent researcher. Beyond academic mentorship, his energetic spirit and relentless dedication have been a constant source of inspiration and have left an enduring impact on my scholarly pursuits.

I extend my sincere gratitude to my doctoral committee members, Prof. S. Ravi, Prof. D. Pal, and Prof. P. S. Robi, for their continuous academic guidance and thoughtful evaluation of my research progress throughout the course of my Ph.D. Their valuable suggestions, insightful remarks, and constructive feedback not only strengthened the quality of my work but also provided clarity and direction at crucial stages of my research journey.

I would also like to express my sincere appreciation for the weekly group meetings and discussions with Prof. A. Srinivasan and Prof. A. Perumal, which greatly enriched my understanding of various concepts and principles in Physics. I was deeply inspired by the profound depth of their knowledge and exceptional expertise, which laid a strong foundation for my research career. I am also grateful to Dr. B. K. Hazra for his valuable guidance in transport measurements and insightful discussions on various research topics, which significantly enhanced my experimental understanding.

I am grateful to both the current and former Heads of the Department of Physics for their generous administrative support and for granting me the freedom to make full use of the departmental resources throughout my Ph.D. journey. I also extend my sincere thanks to all the faculty members of the Department of Physics at IIT Guwahati for their encouragement and support during the course of my doctoral studies.

I express my sincere gratitude to the Council of Scientific and Industrial Research (CSIR), Government of India, for funding the project (Project No: 03(1431)/18/EMR-II), and to the Ministry of Education, Government of India, for awarding the fellowship that allowed me to pursue my Ph.D. without financial constraints. I extend my heartfelt appreciation to the Department of Physics, including the facilities developed under the support of the Department of Science and Technology (DST), Government of India (Project No: SR/FST/PSII-037/2016), the Central Instrument Facility (CIF), IIT Guwahati for providing essential experimental infrastructure, and the Computer Centre, IIT Guwahati, for access to the high-performance computing resources PARAM-ISHAN and PARAM-KAMRUPA.

I would like to express my heartfelt gratitude to Dr. Sidananda Sarma for his unwavering support throughout various stages of my Ph.D. journey. His presence on campus was like that of a family member, always approachable and ever willing to help me to overcome challenges in my research.

I am especially thankful to Mr. Aditya Kalita, Mr. Lokesh Chakraborty Mr. Basab B. Purkayastha, Mr. Atul Deka, and other technical staff of the Department of Physics for their constant technical assistance during my experimental work. I also express my sincere thanks to Mr. Chandan Borgohain, Dr. Kula Kamal Senapati, Dr. Kh. Kesho Singh, Mr. Sujit Kumar Deb, and Dr. Dolly Gogoi for granting me access to XRD, VSM, FESEM, FETEM, and other instruments whenever required, even during odd hours.

I was particularly inspired by the enthusiastic demonstrations of Physics experiments for school students by Lokesh Sir, Sida Sir, and Aditya Da at IIT Guwahati. Their genuine dedication and outreach efforts awakened in me a deeper appreciation for the importance of nurturing young minds and fostering intellectual curiosity from an early age.

I also gratefully acknowledge the non-teaching staff of the Department of Physics and the wider IIT Guwahati community for their kind support and assistance in various capacities. I appreciate the technical contributions of Mr. Bhaskar, Mr. Kishor, Mr. Milan, Mr. Rupak, and other instrument operators for their efforts in ensuring accurate measurements under the desired conditions. Special thanks to Alok and Dinesh for their dedicated support with FETEM and EDS, even during non-office hours.

I am thankful to my seniors, Dr. Rajkumar Modak, Dr. Aneeta Manjari Padhan, Dr. Dolly Taparia, Dr. Manisha Srivastava, Dr. Nitu, Mr. Subrata Biswas, and Mr. Amritava Sarkar, for enriching my research journey with their valuable insights and constant encouragement. My

knowledge was significantly enhanced through engaging discussions with Manisha didi, Nitu didi, Subrat Bhaiya, Madhav, Alok, Debraj, Dinesh, Harekrishna, Aritra, Sourav, Tandrima, Nidhi, and Pratibha on a wide range of topics.

I am deeply grateful to all my professors from my undergraduate and postgraduate studies, especially Dr. Devendra Singh and Dr. Anil Kumar Yadav, whose teachings laid the foundation of my academic pursuits. I am also thankful to my seniors, Dr. Vivek Nautiyal and Dr. Suresh Kumar, for their constant guidance and motivation during my M.Sc. days and beyond.

I express my deep sense of gratitude to my friends Trayambak, Arun, Sudhanshu bhaiya, Satish, Mahendra, Anwesh, Somo, Guddu, Pawan, Sachin, Sarvesh, and many others for their constant moral support and motivation throughout this journey. I would also like to acknowledge my IITG friends Akanshu, Sayan, Pushpanjali, Shubhangi, Sudeshna, Suchit, Debabrata, Monu, Sourav, Pathav, Dinesh and others for contributing to a healthy, engaging, and intellectually stimulating research environment. From my very first day at the IIT Guwahati campus, my bond with Akanshu and Sayan grew as naturally as that of childhood friends. Their unwavering support and caring nature helped me navigate numerous challenges with ease, and for that, I remain deeply thankful. I would also like to acknowledge my hostel friends Vikas, Deepak, Sumit, and others for their helpful nature and moral support.

I feel extremely fortunate to have been part of a wonderful lab group that provided a comfortable, supportive, and stress-free working environment. I would like to take this opportunity to sincerely thank Amritava bhaiya, Sunil bhaiya, Nitu didi, Manisha didi, Subrata bhaiya, Alok, Madhav, Dev, Didwmsha, Debraj, Dinesh, Aritra, Harekrushna, Sourav, Tandrima, Nidhi, Praduman, Pratibha, Abul, Sanjay, Abhinath, and Franky. Their warmth, homely care, and selfless support both in research and in personal matters have been truly invaluable. They stood by me in moments of joy and difficulty, and with them, I found a second family within the lab. The time we shared together brought calm and joy to my life, making this long journey smoother and more memorable. I am especially grateful to Madhav, Alok, and Debraj for their engaging discussions, which greatly enhanced my understanding of various theoretical and experimental aspects of research. Celebrating Rakshabandhan with Manisha didi, Nitu didi, Sudeshna, Tandrima, Nidhi, and Pratibha brought a sense of home and tradition to campus life. The caring nature of each and every lab member made the lab feel like home, and for that, I am deeply thankful.

I would like to express my sincere gratitude to Amritava bhaiya for his constant support during the initial days of my Ph.D. in the Materials Science lab and at the Central Workshop. His guidance in preparing various electrodes and helping me to operate optical microscopes and other instruments was invaluable. I am also thankful to seniors, Deep bhaiya and Saptarshi bhaiya, for their encouraging words and assistance at various stages of my research. I feel truly fortunate to have had seniors like Manisha didi and Subrat bhaiya, whose time, support, and guidance were instrumental in helping me become familiar with various instrument facilities in the department and at CIF, such as the VSM, profilometer, and many more.

I am deeply grateful to Srinivasan Sir and his family for providing a warm, homely environment during festivals and other occasions, ensuring that we never felt far from home. Beyond the joyful celebrations, their constant motivation, kindness, and blessings created a positive and encouraging atmosphere for me and all labmates, which greatly enriched our experience throughout this journey.

I consider myself truly fortunate to be surrounded by a loving and supportive family. I owe everything to my parents, whose countless sacrifices, unwavering encouragement, and unconditional love have shaped me into the person I am today. Their tireless efforts and constant motivation at every step of life made it possible for me to pursue this Ph.D. journey, something I could not have even imagined without them. I am deeply grateful to my grandparents for their blessings, which have always been a source of strength. I also extend my heartfelt thanks to my elder brother and sisters for their continuous love, care, and encouragement, and to my younger brother, Ujjwal, for his affectionate and supportive nature. I am also thankful to my sister-in-law for her moral support throughout my academic journey. During the stressful periods of my research work in the lab, phone conversations with my niece, Prisha, and my nephew, Shlok, brought me immense comfort. Their innocent chatter and joyful energy often helped me momentarily forget my stress and regain focus on my work

Finally, I would like to express my heartfelt gratitude to everyone who has supported me directly or indirectly throughout this journey and contributed in some way to my accomplishments. To those whose names I may have inadvertently missed, please know that your support has been deeply valued, and I sincerely thank you all for helping me reach this important milestone.

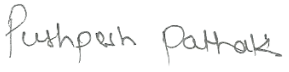

Pushpesh Pathak

Preface

Development of multifunctional materials is the prime focus of contemporary materials science research. Magnetic materials find a special place among these exotic materials due to their unique physical properties and wide-ranging technological applications. Starting from the bulk and extending down to nanostructures, magnetic materials continue to serve as a foundation for modern technological innovations. In particular, magnetic thin films are vital for advancing solid-state micro and nanoelectronics, with ongoing research being driven by demands for high performance, sustainable, and energy efficient devices. In this context, the emerging field of spintronics offers significant advantages over conventional electronics by utilizing both the charge and spin of electrons. Spintronic materials, especially half-metals, are of great interest due to their ability to exhibit 100% spin polarization (P) at the Fermi level (E_F), thereby enabling the generation and manipulation of spin-polarized currents. Among the half-metallic materials, Heusler alloys have garnered attention owing to their excellent structural, magnetic, and electronic characteristics. Ferromagnetic Heusler alloys, in particular, are promising candidates for spintronic applications such as magnetic tunnel junctions and spin valves.

Among the family of Heusler alloys identified so far, Co and Fe based Heusler alloys are particularly appealing due to their superior properties, including high saturation magnetization (M_s), elevated Curie temperature (T_C), large effective anisotropy constant (K_{eff}), low Gilbert damping constant (α), and high P. Among Co based Heusler alloys, Co_2FeSn with a highly ordered $L2_1$-type structure has emerged as a promising material for spintronic applications due to high M_s, elevated T_C, and high P value. However, synthesizing Co_2FeSn *via* conventional methods like arc melting is challenging, due to unavoidable phase segregation of Co_3Sn_2 and CoFe phases. To harness the magnetic and electronic properties for nanomagnetic devices, single phase Co_2FeSn must be synthesized in thin film form. In this regard, electrodeposition offers a simple, non-equilibrium, cost-effective, and easily scalable solution for the synthesis of Co_2FeSn alloys. In addition to Co_2FeSn, Fe_2CoSn is a notable member of the Fe based Heusler alloy. Fe_2CoSn exhibits a highly ordered X-type stable crystal structure, along with high M_s, elevated T_C, and high K_{eff} value. Despite their potential, the few existing literatures on Co-Fe-Sn and Fe-Co-Sn Heusler alloy films reveal several critical gaps. These need to be addressed to fully assess them and harness their potential for developing efficient nanomagnetic devices.

The key limitation of the earlier studies is the poor crystalline ordering achieved in the synthesized Co_2FeSn films, which has resulted in low M_s and T_C. A survey of the literature

shows that structural, morphological, and magnetic properties of Co_2FeSn films have not been systematically investigated as a function of film thickness. Likewise, there is a lack of studies on highly ordered Fe_2CoSn films. On the theoretical front, the role of electron correlations has not been considered in the computational studies of Co-Fe-Sn and Fe-Co-Sn alloys containing *d*-group transition metals. Additionally, the impact of atomic substitution in tailoring the minority band gap near E_F has not been explored in these ternary Heusler alloys. This thesis work aims to bridge the existing gaps in the literature on electrodeposited Co-Fe-Sn and Fe-Co-Sn Heusler alloy films by focusing on the following aspects: (a) Synthesis of highly ordered, stoichiometric Co_2FeSn and Fe_2CoSn alloy thin films *via* electrodeposition, followed by a detailed assessment of their structural, morphological, electronic, and magnetic properties. (b) Systematic investigation of the influence of film thickness on the structural, morphological, and magnetic properties of Co_2FeSn thin films. (c) Exploration of strategies to enhance the half-metallicity of Co_2FeSn films involving controlled variation of the stoichiometric ternary alloy composition and atomic substitution of a fourth element in the ternary alloy.

The thesis consists of eight chapters. Chapter 1 presents an introduction to the crystal structure and properties of Heusler alloys and a comprehensive review of the relevant literature. This is followed by a discussion on electrodeposition as a viable technique for synthesizing Sn based Heusler alloys such as Co-Fe-Sn and Fe-Co-Sn. It also presents the motivation behind this thesis work, the objectives undertaken, and a brief outline of the content of the thesis. Chapter 2 of the thesis outlines the synthesis technique employed, *viz*., electrodeposition, for the deposition of the proposed Heusler alloy films. It also provides detailed information on the basic principles and theory behind experiments and characterization techniques used in the investigations. At the end of this chapter, details of the *ab initio* calculations performed to evaluate the magnetic and electronic properties are discussed. Chapters 3 to 7 present the core research work carried out in this thesis towards the objectives mentioned above. Chapter 8 provides a summary of the work done, highlighting the key findings and briefly outlining potential directions for future research in this area.

With respect to the objectives cited above, this thesis work has achieved the following: Demonstrated (a) the relevance of electrodeposition in the synthesis of Sn based alloy films, (b) a methodology to synthesize phase pure Heusler alloy films with high crystalline order and good control on composition and thickness, (c) improved magnetic and electronic properties in Co-Fe-Sn and Fe_2CoSn alloy films through improved atomic ordering, and (d) strategies to induce half-metallicity in ternary Co_2FeSn alloy film by tuning alloy composition and by atomic substitution of Cr for Fe.

Table of Contents

Chapter 1

Introduction

The pursuit of new materials with diverse and multifunctional properties has consistently been the top priority of materials scientists [DOBR2006, HUMM2004, OHRI1992, MODA2018a]. Among the broad spectrum of materials, magnetic materials have emerged as leading candidates owing to their intriguing physical properties and wide range of applications. Magnetic materials have evolved over time, transitioning from bulk forms to nanostructures to meet the growing demands of modern technologies [COEY2001, SCHE2016, SHEN2018]. Contemporary advancements prioritize devices that are faster, more efficient, cost-effective, and miniaturized, spanning from the microscale down to the nanoscale [INIE2015, INIG1999]. In this context, magnetic thin films play a crucial role in advancing solid-state micro and nanoelectronics technologies. Research on these two-dimensional nanostructures has opened new frontiers in solid-state physics and related fields, largely influenced by their elemental composition, structural characteristics, and thickness-dependent properties. The widespread application of thin films in various fields such as space science, defence, automobile industry, research instrumentation and various industrial sectors has driven researchers to focus intensively on thin film development [MODA2018a]. This has resulted in numerous innovations in terms of active devices and passive components such as sensor elements, micro transducers, microelectronic devices, microelectromechanical systems, magnetic read heads, magnetic sensors, micro actuators, etc. [KAUN2008, MODA2018a, TEIC2015] The current emphasis on high-performance, sustainability, and energy efficiency serves as the guiding principle for cutting-edge technological advancements. Aligned with these objectives, the emerging field of spintronics offers several advantages over traditional semiconductor-based electronics. While conventional semiconductors primarily rely on the charge of the electron, spintronics adds the spin component to conventional charge-based electronics by exploiting the intrinsic spin of charge carriers. To harness the spin component effectively, a reliable source of spin current is essential. For this purpose, materials that exhibit high spin polarization (P) are essential to maximize the efficiency of spin-based electronic devices [FELS2007]. One

effective approach to achieving a high *P* is through the use of half-metallic materials. Among half-metallic materials, Heusler alloys stand out due to their tunable structural, magnetic, and electronic properties [GALA2006]. In this context, ferromagnetic Heusler alloys are more in demand for use in various spin-based electronics (spintronics) applications such as magnetoresistive random-access memory, magnetic tunnel Junctions, spin light-emitting diodes, and thermoelectric devices [SUKE2014, ARAV2022]. Apart from half-metallicity, Heusler alloys have fascinated researchers due to their capability to display exceptional properties such as spin-gapless semiconducting behaviour [OUAR2013], shape memory effect [DEBR2024], magnetocaloric effect, and thermoelectricity [HINT2019].

Among various Heusler alloys discovered so far, Co and Fe based Heusler alloys have demonstrated exceptional properties, including high saturation magnetization (M_s), elevated Curie temperature (T_C), high effective anisotropy constant (K_{eff}), and high *P* [ARAV2022, HUKU2023, PATH2022, PATH2023, PATH2024, SHAK2021]. Taking all these factors into account, this thesis focuses on exploring the diverse functionalities of stoichiometric and non-stoichiometric Co and Fe based Heusler alloy films electrodeposited on cost-effective polycrystalline Cu substrates.

1.1. Heusler alloys

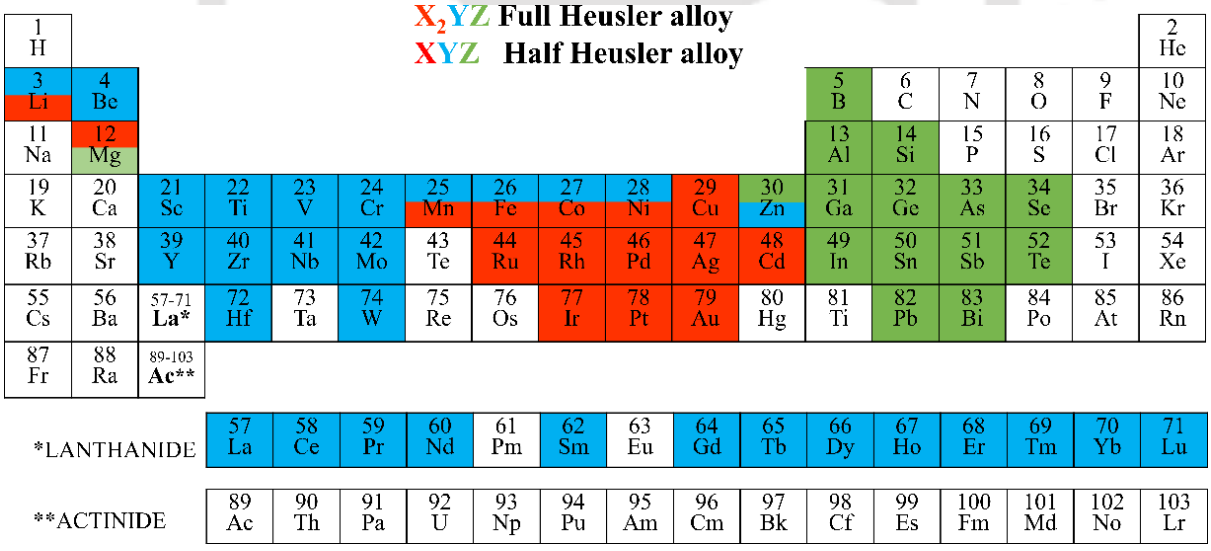

Figure 1.01. Periodic table displaying the choice of elements for X, Y, and Z in HAs.

Heusler alloys (HAs) are typically ternary intermetallic alloys having the chemical formula X_2YZ [FONG2013], where X and Y are transition metals, and Z is typically an element from *p*-block, as illustrated in Figure 1.01. In 1903, F. Heusler was the first to investigate the compounds Cu_2MnAl and Cu_2MnSn, later known as Heusler alloys, and found that these

materials exhibited ferromagnetic behaviour despite containing no inherently ferromagnetic elements. This unexpected finding captivated the minds of both theorists and experimentalists [FELS2016, HEUS1903]. The crystal structure of HAs, however, remained unknown until 1934, waiting for Otto Heusler [HEUS1934] and Bradley *et al.* [BRAD1934] to reveal it. The remarkable properties and phenomena exhibited by HAs stem primarily from their distinctive crystal structure. This led to the emergence of a new class of materials possessing a wide range of properties in the field of materials research [BAIZ2013].

1.1.1. Ordered Heusler alloy crystal structure

The unit cell of a fully ordered X_2YZ Heusler alloy (HA) consists of four interpenetrating face-centred cubic (fcc) sublattices located at Wyckoff positions of (0, 0, 0), (¼, ¼, ¼), (½, ½, ½), and (¾, ¾, ¾) [FELS2016, MATS2017] as shown in Figure 1.02 (a). Depending upon the selection of X and Y transition metal atoms, the fully ordered HAs can be characterized into the following categories:

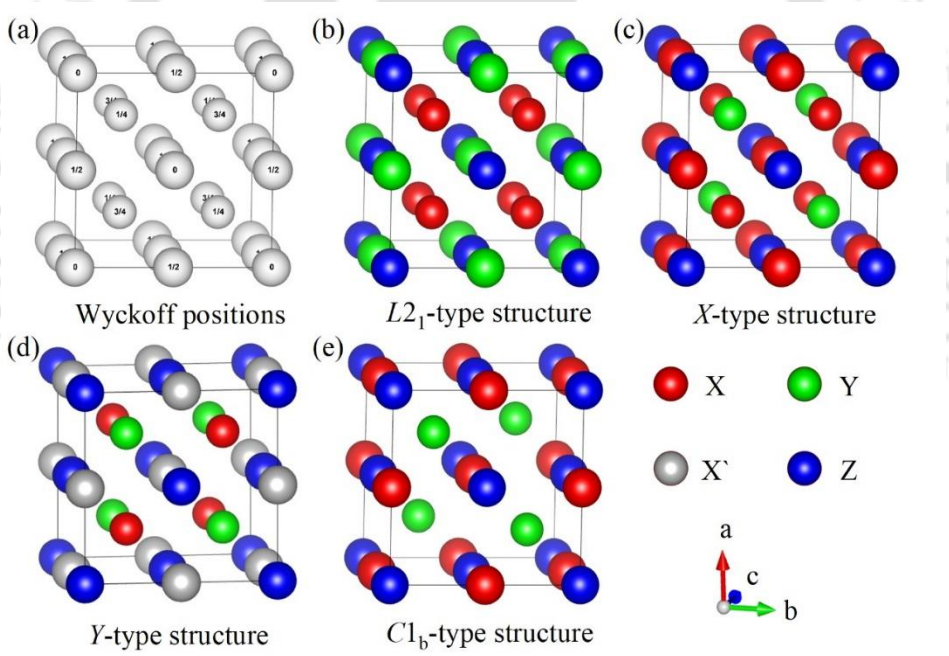

Figure 1.2. (a) Wyckoff positions of HA structure. Crystal structures of fully ordered (b) $L2_1$-type, (c) *X*-type, (d) *Y*-type, and (e) $C1_b$-type HA.

*L*2₁-type structure

In $L2_1$-type full HA structure (Cu_2MnAl-like), which crystallizes in the space group $Fm\bar{3}m$ (No. 225), in which X atom possesses a higher valence electron number than that of Y atom. In this structure, the X atoms occupy the equivalent Wyckoff sites (¼, ¼, ¼) and (¾, ¾, ¾),

the Y atom is located at (½, ½, ½), and the Z atom resides at (0, 0, 0) [FELS2016, MATS2017], as shown in Figure 1.02 (b).

_X_-type structure

If the valence electron number of the Y transition metal atom is higher than that of the X atom, then the structure is known as *X*-type inverse HA structure. In the *X*-type inverse HA structure ($CuHg_2Ti$-like), with the space group $F\bar{4}3m$ (No. 216), the X atoms are positioned at the non-equivalent Wyckoff sites (½, ½, ½), and (¾, ¾, ¾), Y atom occupies the position (¼, ¼, ¼), and Z atom is located at (0, 0, 0) [FELS2016], as demonstrated in Figure 1.02 (c).

_Y_-type structure

In the $L2_1$-type structure, if all four distinct Wyckoff sites are occupied by different elements, the resulting quaternary (XX'YZ) alloy is referred to as a *Y*-type HA. The *Y*-type HA structure, exemplified by the LiMgPdSn prototype and crystallizing in the space group $F\bar{4}3m$ (No. 216), with the X, X`, Y and Z atoms are positioned at (¼, ¼, ¼), (½, ½, ½), (¾, ¾, ¾), and (0, 0, 0) [FELS2016] Wyckoff sites, respectively, as illustrated in Figure 1.02 (d).

$C1_b$-type structure

If either the (¼, ¼, ¼) or (¾, ¾, ¾) Wyckoff sites in $L2_1$-type full HA are vacant, the resulting structure is known as $C1_b$-type (half-Heusler) structure with chemical formula XYZ, as portrayed in Figure 1.02 (e). The $C1_b$-type Heusler structure, exemplified by the MgAgAs prototype and crystallizing in the space group $F\bar{4}3m$ (No. 216) [FELS2016].

1.1.2. Heusler alloy structures with atomic disorder

HAs often exhibit structural disorders during synthesis due to intermixing of constituent elements in the Wyckoff positions (*c.f.*, Figure 1.03 (a)), preventing the formation of an ordered structure. The possible atomic disorders in the fully ordered structures are:

_B_2-type disorder

If the Y and Z atoms within the $L2_1$-ordered structure are intermixed, the resulting structure is known as *B*2-type partially disordered structure [FELS2016] as shown in Figure 1.03 (b). This structure can be conceptualized on the basis of the prototype CsCl, leading to a reduced symmetric space group $Pm\bar{3}m$ (No. 221) [FELS2016]. A distinctive feature of this structure is the presence of the (200) superlattice reflections, accompanied by the absence of the (111) superlattice reflections [FELS2016] in the diffraction patterns.

DO_3-type disorder

The DO_3-type disordered structure results from the intermixing of X and Y or X and Z atoms within the $L2_1$-type fully ordered structure, as depicted in Figure 1.03 (c). Its prototype structure

is BiF_3 structure, which crystallizes in the space group $Fm\bar{3}m$ (No. 225) [FELS2016]. It is difficult to identify this atomic disorder from diffraction patterns [FELS2016].

***A*2-type disorder**

Another form of atomic disorder in the fully ordered HA structure is *A*2-type, which arises from the complete intermixing of all three X, Y, and Z atoms, leading to a further reduction in symmetry with a space group $Im\bar{3}m$ (No. 229) as illustrated in Figure 1.03 (d). This structure is based on the prototype tungsten (W), which adopts a body centred cubic lattice [FELS2016]. It is distinguished by the absence of both (111) and (200) superlattice reflections in X-ray or electron diffraction patterns.

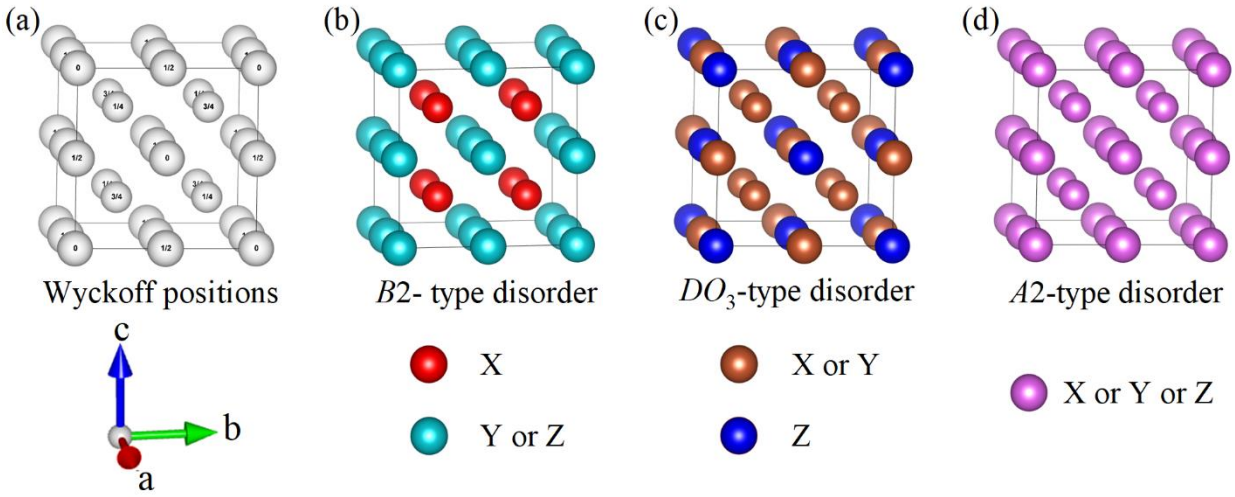

Figure 1.03. (a) Wyckoff positions of HA structure. HA structure with (b) *B*2-type, (c) DO_3-type, and (d) *A*2-type atomic disorder.

1.1.3. Properties of Heusler alloys

HAs are renowned for their diverse and intriguing physical properties, including high *P* [JOUR2014], high M_s [WURM2005], strong magnetic anisotropy [HEYA2020], elevated T_C [JAGG1978], thermoelectric properties [SUZU2004], and superconductivity [WERN1983]. Additionally, they also exhibit topological insulating behaviour [CHAD2010], and heavy fermion characteristics [DENI2001]. Further, phenomena like martensitic transformations and shape memory effects have also been observed in these alloys [TICK1999]. The origin and underlying mechanisms responsible for several of these properties are discussed in detail in the subsequent sections.

1.1.3.1. Magnetic Properties

HAs represent a diverse family of compounds known for their extensive and versatile magnetic properties. The empirical Slater-Pauling (S-P) behaviour [GALA2002] for half-metallic HAs aids in tuning the magnetic moment by establishing a correlation between the total number of valence electrons (Z_t) and the total spin magnetic moment (M_t) [GALA2002]. The relationship between Z_t and M_t based on the S-P rule can be further clarified by connecting Z_t and M_t to the count of valence electrons in the spin-up ($N_\uparrow$) and spin-down ($N_\downarrow$) states [GALA2002]. This relationship is expressed as follows:

$$Z_t = N_\uparrow + N_\downarrow \quad (1.01)$$

While M_t can be written as

$$M_t = N_\uparrow - N_\downarrow \quad (1.02)$$

Combining eq. (1.01) and eq. (1.02),

$$M_t = Z_t - 2\,N_\downarrow \quad (1.03)$$

Here, M_t arises due to the excess number of uncompensated valence electrons. For half-metallic full Heusler compounds, M_t can be determined using the formula [GALA2002],

$$M_t = Z_t - 24 \quad (1.04)$$

Similarly, for half-Heusler compounds, the relationship is expressed as [GALA2002]:

$$M_t = Z_t - 18 \quad (1.05)$$

Inverse HAs follow three different rules, depending on their electronic structure [SKAF2013]:

$$\left.\begin{array}{l} M_t = Z_t - 18, \\ M_t = Z_t - 24, \text{ and} \\ M_t = Z_t - 28 \end{array}\right\} \quad (1.06)$$

These relationships are collectively referred to as the generalized S-P rules for half-metallic HAs. In the case of full HAs, compounds with $Z_t < 24$ are typically ferrimagnetic in nature, whereas those with $Z_t = 24$ are non-magnetic. Compounds with $Z_t > 24$ are generally ferromagnetic. These rules provide a robust framework for predicting and understanding the magnetic behaviour of half-metallic Heusler-based compounds based on their electronic

structure. HAs based on Co and Fe typically exhibit $Z_t > 24$, which results in ferromagnetic behaviour [GALA2002, SKAF2013].

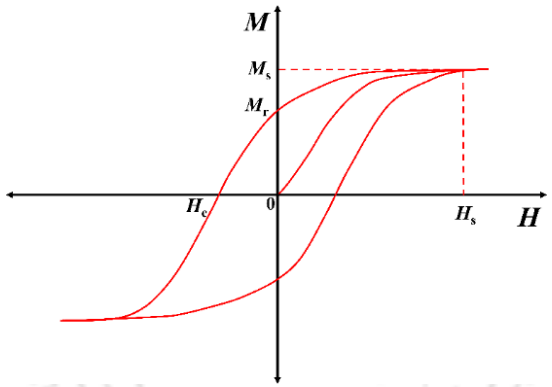

Figure 1.04. *M-H* loop demonstrating M_s, M_r, H_c, and H_s of a ferromagnetic material.

As ferromagnetic materials, HAs display magnetic hysteresis (*M-H*) loop, as depicted in Figure 1.04. Analysis of the *M-H* loop provides valuable insights into the magnetic characteristics, such as M_s, remanence (M_r), and coercive field (H_c). These parameters are essential for evaluating the suitability of magnetic materials for various technological applications. The first quadrant of the *M-H* loop, also known as the initial or virgin magnetization curve, can be analysed to determine the effective anisotropy constant (K_{eff}) of a material. The law of approach to magnetic saturation describes how magnetization (M) increases with an applied magnetic field (H) as it approaches saturation. This relationship incorporates contributions from anisotropy and structural imperfections within the material, providing valuable insights into its magnetic behaviour [ANDR1997, JINZ1998]. The law of approach to magnetic saturation can be described by the relation,

$$M(H) = M_s\left(1 - \frac{g_1}{H} - \frac{g_2}{H^2} - \cdots\right) + \chi_{hf}H \qquad 1.07$$

where M_s is spontaneous magnetization, χ_{hf} is the high field susceptibility, $\frac{g_1}{H}$ corresponds to structural defects and non-magnetic inclusions, while $\frac{g_2}{H^2}$ attributed to uniform magnetocrystalline anisotropy. When the applied external magnetic field is high enough, the magnetization proceeds by domain rotation. Assuming atoms orientation to be arbitrary and strain distribution is homogenous [ANDR1997, JINZ1998], eq. (1.07) can be simplified into

$$M(H) = M_s\left(1 - \frac{g_2}{H^2}\right) \qquad 1.08$$

Using the estimated M_s and g_2, K_{eff} for a cubic system can be estimated as [ANDR1997, DEKA2016],

$$K_{\text{eff}} = \mu_0 M_s \left(\frac{105\, g_2}{8} \right)^{1/2} \qquad 1.09$$

where μ_0 indicates the permeability of free space.

T_C is one of the most important parameters for any kind of application of ferromagnetic materials. T_C is defined as the temperature above which a ferromagnetic material behaves like a paramagnet due to random thermal fluctuations of the magnetic spins. For device applications, a high T_C is highly desirable. Notably, most of the Co and Fe based HAs display T_C higher than room temperature, making them promising candidates for spintronic and magnetic applications [HUKU2023]. Co-based HAs show T_C comparable to that of the 3*d* transition metals like Co and Fe. The reason for the high T_C is the strong interaction between Co-Y and Co-Co atoms present at different sublattices. It is interesting to note that the T_C of Co-based alloys follow a linear dependence with the number of valence electrons and magnetic moments per atom [KARI2022a]. Figure 1.05 portrays the variation of T_C with the number of valence electrons in Co-based HAs. The open squares and red-filled circles represent the estimated T_C obtained from *ab initio* calculations and the experimental measurements, respectively, for various Co based HAs.

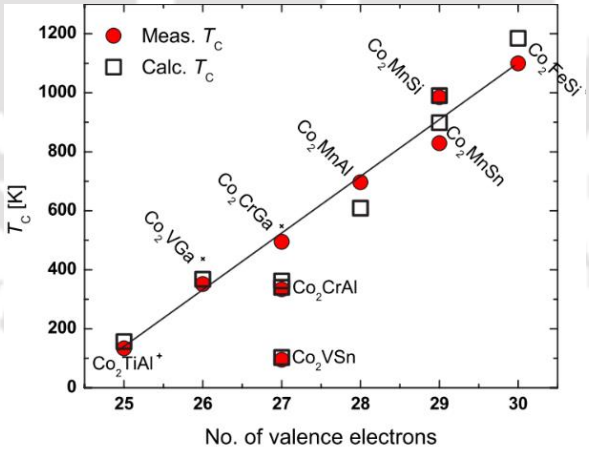

Figure 1.05. Variation of T_C with the number of valence electrons in Co-based HAs obtained from theoretical and experimental studies [KARI2022a].

1.1.3.2. Half-metallicity and spin polarization

Half-metallic materials have become a focal point for spintronic research due to their distinctive electronic band structure, which exhibits metallic behaviour for one spin channel while displaying semiconducting or insulating characteristics for the other spin channel

[FONG2013]. This results in 100% spin polarization at the Fermi level (E_F). Spin Polarization (P) is a crucial physical parameter for quantifying the half-metallicity of alloys at E_F. It is defined by the formula

$$P = \frac{N_\uparrow - N_\downarrow}{N_\uparrow + N_\downarrow} \qquad 1.10$$

where $N_\uparrow$ and $N_\downarrow$ are the density of states (DOS) for spin-up and spin-down channels at E_F, respectively [FONG2013]. The half-metallic materials with 100% spin polarization offer several key advantages over conventional electronic devices, including significantly reduced Joule heating, which leads to improved energy efficiency. This enhanced energy efficiency translates into lower power consumption. Furthermore, spintronic devices feature faster data processing speeds, compact size, and non-volatile memory retention, making them highly promising for next-generation technology [FONG2013].

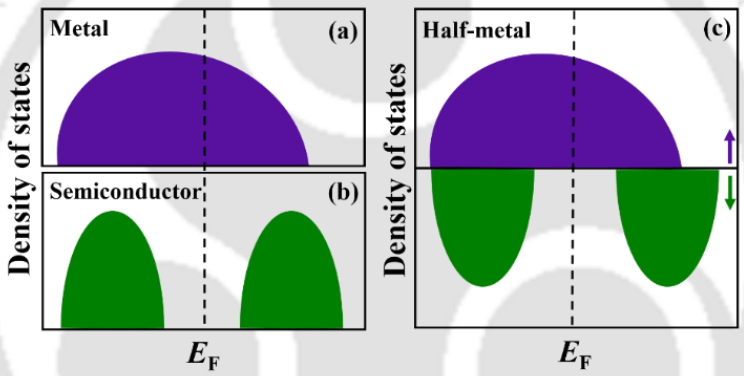

Figure 1.06. Schematic representation of the DOS near E_F for (a) metallic, (b) semiconducting, and (c) half-metallic materials.

Figure 1.06 portrays a schematic representation of the DOS near E_F for metallic, semiconducting, and half-metallic materials. In 1983, de Groot *et al.* [GROOT1983] first identified half-metallicity in the half-Heusler compound NiMnSb through *ab initio* calculations. This marked a major breakthrough, establishing HAs as prominent candidates for spintronic applications that exploit their half-metallic properties. Since then, HAs have attracted substantial attention for their remarkable spin-dependent electronic characteristics [FELS2016, FONG2013]. A defining feature of half-metallic compounds is the presence of at least one transition metal element, whose *d*-orbitals play a crucial role in the manifestation of half-metallicity. Additionally, the interaction of these *d*-orbitals with the electronic states of other elements, such as the *d*-orbitals of other transition metals or the *sp*-orbitals of Group III–V elements, significantly influences the material's properties, including its half-metallic nature.

To understand the origin of the half-metallic gap in the minority spin channel of $L2_1$-type full HA, consider the example of the half-metallic Co_2MnGe HA system which is schematically presented in Figure 1.07. When two neighboring Co atoms of Co_2MnGe interact, their $d_{x^2-y^2}$ and d_{z^2} orbitals hybridize to form doubly degenerate bonding e_g and antibonding e_u states. Similarly, d_{xy}, d_{yz}, and d_{zx} orbitals hybridize to produce triply degenerate bonding t_{2g} and antibonding t_{1u} states. The e_g states resulting from Co-Co hybridization further interact with the $d_{x^2-y^2}$ and d_{z^2} of Mn atoms, forming doubly degenerate bonding e_g states at lower energy, along with unoccupied anti-bonding e_u states located above the E_F. d_{xy}, d_{yz}, and d_{zx} orbitals of Mn atom couple with triply degenerate Co-t_{2g} states and form 3 occupied bonding t_{2g} states and 3 unoccupied anti-bonding states above and below E_F, respectively. Since e_u and t_{1u} states are not available for Mn atoms, the $2 \times e_u$ and $3 \times t_{1u}$ states of hybridized Co-Co atoms cannot couple with Mn *d*-orbitals. The t_{1u} states are occupied and lie below E_F, whereas e_u are above E_F. Thus 8 minority *d*-bands *i.e.*, $2 \times e_g$, $3 \times t_{2g}$ and $3 \times t_{1u}$ are occupied and 7 *d*-bands *i.e.*, $2 \times e_u$, $2 \times e_g$ and $3 \times t_{2g}$ are unoccupied in the case of Co_2MnGe compound [GALA2002]. Apart from this hybridization, there are contributions from 1*s* and 3*p*-orbitals. Thus, in case of full HAs, there are total 12 minority occupied states per unit cell. As a result, the total moment obeys the rule $M_t = Z_t - 24$ [GALA2002].

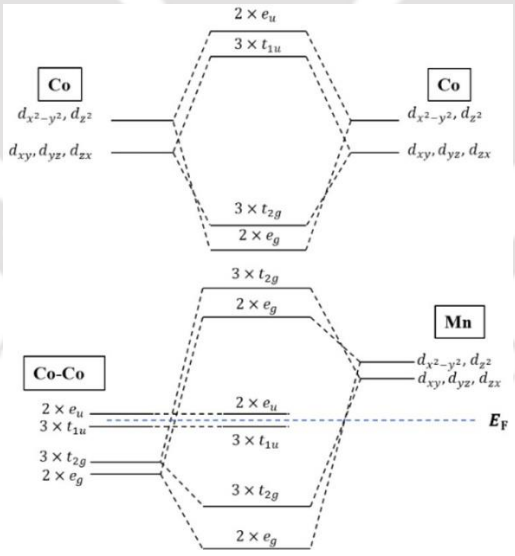

Figure 1.07. Possible hybridization between the *d*-orbitals present at different atomic sites in Co_2MnGe full HA.

Figure 1.08 portrays the variation of M_t with Z_t for full HAs. In the case of half-Heusler alloy like NiMnSb, the situation is more straight forward. The *d*-orbital of the two (X and Y) transition-metal atoms strongly hybridize, forming five occupied bonding *d*-states and five

unoccupied antibonding *d*-states in the spin-down channel [GALA2002]. Apart from these hybridizations, additional contributions arise from 1*s* and 3*p*-orbitals. As a result, there are exactly 9 occupied spin-down states. The corresponding S-P relation is given by $M_t = Z_t - 18$.

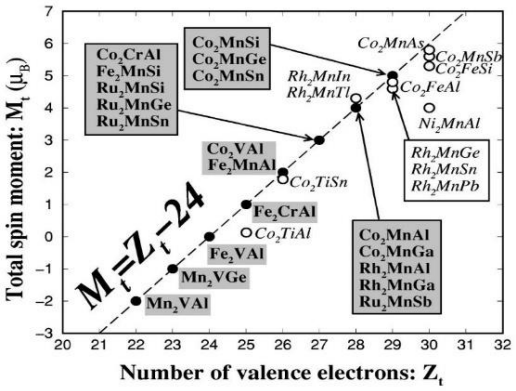

Figure 1.08. M_t *versus* Z_t for different full HAs according to the S-P rule [GALA2002].

In inverse HAs (*X*-type), atomic arrangement differs from that of conventional $L2_1$-type Heusler structure. In the *X*-type structure, the X atoms at Wyckoff sites (¾, ¾, ¾) (denoted as X^A), exchange positions with the Y atoms at Wyckoff sites (½, ½, ½). Consequently, X_A atoms first hybridize with the Y atoms, and these hybridized states further hybridize with the X atoms situated at the Wyckoff site of (¼, ¼, ¼) (denoted as X^B) as depicted in Figure 1.09. The difference in the splitting of these states after hybridization leads to variations in the number of occupied spin-down states, giving rise to three distinct magnetic moment rules: $M_t = Z_t - 18$, $M_t = Z_t - 24$, and $M_t = Z_t - 28$ [SKAF2013]. Figure 1.10 illustrates the dependencies of M_t on Z_t for various inverse HAs.

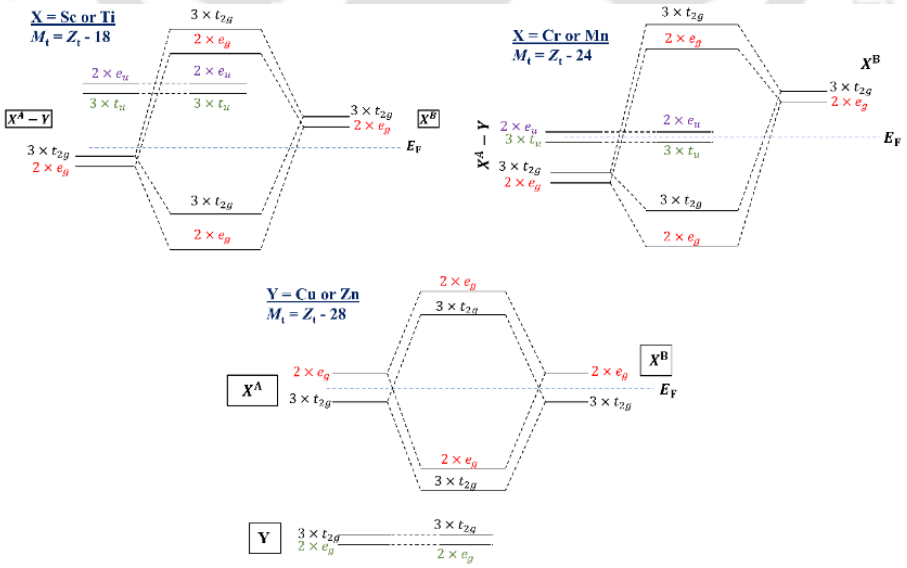

Figure 1.09. Possible hybridizations between different *d*-orbitals present at different atomic sites of inverse HAs X_2YZ.

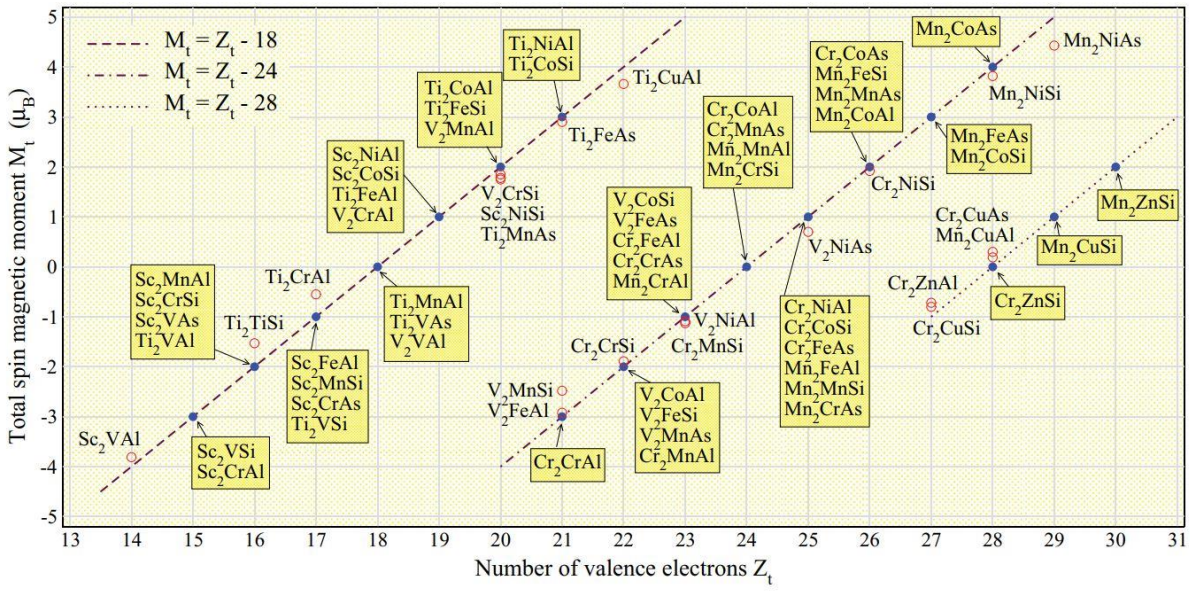

Figure 1.10. Variation of M_t with Z_t according to the S-P rule for inverse HAs [SKAF2013].

1.1.3.3. Shape memory effect

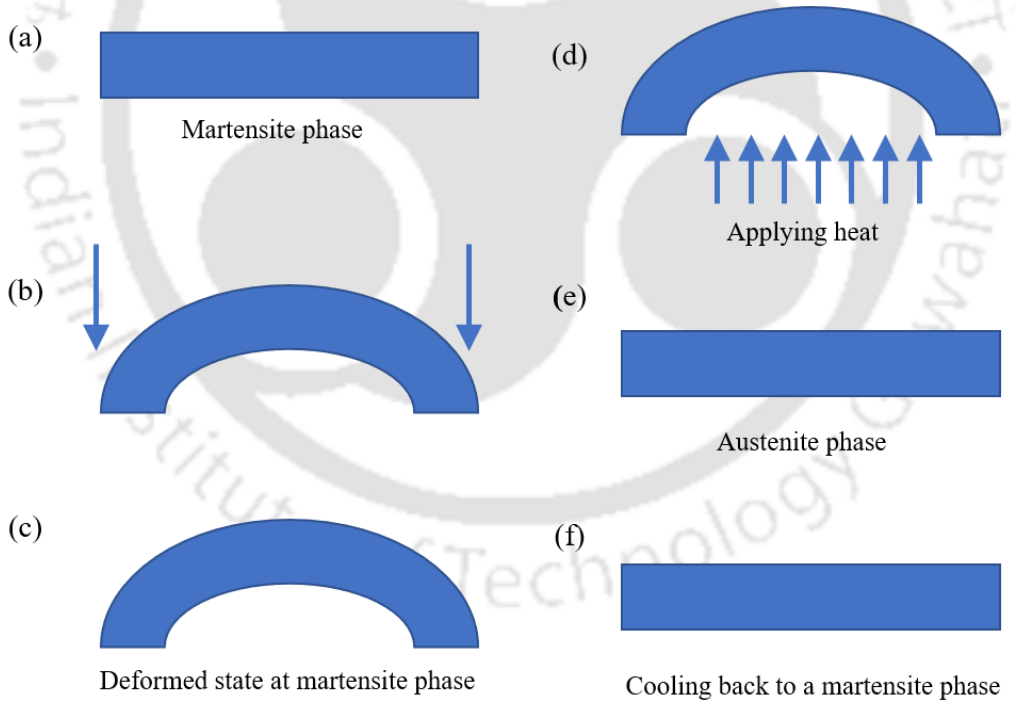

Figure 1.11. Illustration of martensitic phase transformation responsible for the shape memory effect.

In the family of HAs, numerous compounds exhibit a temperature-dependent structural phase transition from a highly symmetric (cubic) austenite phase to a low-symmetry (tetragonal or

hexagonal) martensite phase upon cooling. This first-order, diffusionless, and reversible phase transition is known as martensitic transition, which enables the shape memory effect (SME). SME refers to the ability of a material in the martensite phase to undergo a transformation in shape upon the application of an external stimulus and subsequently recover its original shape when heated to a temperature enough to induce the austenite phase. Materials that exhibit SME are known as shape memory alloys (SMAs). The transformation process becomes faster when a magnetic field acts as a stimulus in certain ferromagnetic materials, which are referred to as ferromagnetic shape memory alloys (FSMAs). Typically, HAs containing Ni and/or Mn fall into this category, including compositions such as Ni-Mn-Z (Z = Ga, Al, Sn, In) and Co-Ni-Z (Z= Ga, Al) [MODA2018a]. Illustration of martensitic phase transformation responsible for the shape memory effect is depicted in Figure 1.11.

1.2. Advancements in Heusler alloys

After the initial studies by F. Heusler [HEUS1903], Otto Heusler [HEUS1934], and Bradley *et al.* [BRAD1934] on Cu_2MnAl and Cu_2MnSn, Webster and Ziebeck [WEBS1973] synthesized Co based full HAs. Later, in 1978, Jaggi *et al.* [JAGG1978] investigated the site preference in induction-melted Co_2FeGa and Fe_2CoGa compounds. In 1980, Grover *et al.* [GROV1980] conducted similar studies on Co_2FeAl and Fe_2CoAl compounds. Subsequently, Buschow *et al.*[BOSC1981] prepared a series of Co_2YAl with Y = (Fe, Mn, Cr, Ta), and Fe_2YAl with Y = (Cr, Mn, Ni) alloys, exhibiting magnetic moment ranging from 1.50 to 4.96 μ_B/f.u. and 1.67 to 4.25 μ_B/f.u., respectively [BOSC1983]. In 1982, Ishida *et al.* [ISHI1982] explored half-metallic ferromagnetism in Co based HAs like Co_2MnSn, Co_2TiSn, and Co_2TiAl using first-principles calculations. However, they did not observe half-metallic ferromagnetism in these compounds. Later in 1983, de Groot *et al.* [GROO1983] observed half-metallic behaviour in half-Heusler NiMnSb. Following this, Galankis *et al.* [GALA2006] carried out theoretical investigations and found that NiMnSb, CoMnSb and FeMnSb have half-metallic nature. In contrast, Ksenofontov *et al.* [KSEN2006] demonstrated that bulk CoMnSb exhibits a non-half-metallic character based on the experimentally determined structure. Ishida *et al.* [WOLL2017] reported half-metallic behavior in Co_2MnGe and Co_2MnSi *via ab initio* calculations, while Fuji *et al.* [FUJI1995] observed half-metallic nature in Fe_2MnSi during their study on Fe_2MnZ alloy system with Z = Al, Si, and P. Galankis *et al.*, [GALA2002] in their computational study on full HAs, demonstrated half-metallicity in Co_2MnGe and non-half-metallic nature in Co_2MnZ (Z = Al, Sn), and described the variation of M_t with Z_t in these compounds. Özdogan *et al.* [OZDO2007], during their first principle study on $Co_2(Cr_{1-x}Fe_x)Al$, discussed the effect of Fe

concentration on *P* of this alloy system. Marchenkov *et al.* [MARC2017] synthesized bulk Co_2YZ (Y = Ti, V, Cr, Mn, Fe, Ni; Z = Al, Si, Ga, Ge, In, Sn, Sb) alloys and observed half-metallicity in Co_2FeSi HA, and also reported T_C of 1100 K and M_s of 6 μ_B/f.u., which was consistent with the subsequent studies on Co_2FeSi compound [WURM2006].

In addition to the above advancements, HAs containing Co and Fe attract significant interest due to their excellent combination of structural, magnetic, electrical, and electronic properties [FELS2016, GILL2008, YINM2013, FUJI2022, WOLL2017]. Their unique spin band structure makes them promising candidates for developing spintronic devices [FELS2016, FUJI2022, PATH2024]. Furthermore, they exhibit different phenomena, such as ferromagnetism, ferrimagnetism, or antiferromagnetism, depending upon the total number of valence electrons in the alloy [LINZ2020, PATH2024]. T_C of Co based HAs scales with magnetic moment [WOLL2017]. Recent research on Co_2YZ Heusler compounds shows that their topological properties can be altered by tuning the position of E_F [KARI2022a]. Additionally, Fe based HAs display thermoelectric, mechanical, elastic, and spectroscopic properties [FELS2016, TICK1999, SUZU2004]. Among Co and Fe based HAs, Co-Fe-Sn and Fe-Co-Sn have received special attention in the scientific community due to their low-cost, soft ferromagnetic nature with high *P*, elevated M_s, and high T_C [DUAN, GALD2020, GAOS2015, GILL2008, HUAN2015, KHAN2018, LITA2013, LIPE2015, MARC2017, YINM2013, WATA2015].

1.2.1. Literature on Co-Fe-Sn and Fe-Co-Sn Heusler alloys

Huang *et al.*, [HUAN2015] in their computational study on Co_2FeSn HA, reported a *P* of 55%. They emphasized that theoretically predicted *P* does not necessarily reflect the *P* obtained from experimental current transport measurements. Further, *P* measured experimentally can be explained in terms of longitudinal current *P*, for which a value of 93% was reported. Subsequently, Noky *et al.*, [NOKY2018] in their theoretical study on Co_2FeSn, reported a very small anomalous Hall conductivity but a strong anomalous Nernst conductivity. This behaviour was attributed to a nodal-line structure with strong Berry curvature located about 100 meV above the E_F. Due to this energy offset, the topological features are not captured in the anomalous Hall conductivity, which remains nearly zero. However, it gives rise to a pronounced anomalous Nernst conductivity at E_F. Özdoğan *et al.* [OZDO2007] through theoretical study reported a magnetic moment of 5.52 μ_B, whereas Gillebean *et al.* [GILL2008] found a similar value of 5.53 μ_B . Matsushita *et al.*, [MATS2017], through *ab initio* calculation, proposed the possibility of an $L2_1$-type structure for the Co_2FeSn alloy with magnetic moment

of 5.66 μ_B. Similarly, Faleev *et al.* [FALE2017], performing the same study, reported a magnetic moment of 5.70 μ_B. Tanaka *et al.* [TANA2012] prepared the Co_2FeSn HA film by atomically controlled alternate deposition at various substrate temperatures. They reported that the film grown at 250 °C used in magnetic tunnel junction (MTJ) showed tunnel magneto-resistance (TMR) ratio of 72.2% at 2 K and 43.5% at 300K. Li *et al.* [LITA2013] synthesized single-phase Co_2FeSn HA nanoparticles *via* solution reduction method and reported *B*2-type partial disordered structure with particle size of 20-40 nm, M_s of 82 emu/g and H_c of 40 Oe. Subsequent to this, Li *et al.* [LIPE2015] prepared Co_2FeSn nanoparticles *via* a diffusion-assisted method and reported magnetic moment of 5.2 μ_B/f.u. at 5 K. Karim *et al.* [KARI2022b] prepared silica-assisted Co_2FeSn nanoparticles using a chemical method and demonstrated the possibility of strain and crystallite size-controlled ordering in the prepared nanoparticles. Faleev *et al.* [FALE2017] and Matsushita *et al.* [MATS2017] performed the theoretical study on Fe_2CoSn HA and highlighted the possibility of an inverse HA structure with high magnetic moment > 5.4 μ_B. In addition to the above, Malaman *et al.* [MALA2016] attempted to synthesize a series of off-stoichiometric $Fe_{53.3-0.6x}Co_{46.7-0.4x}Sn_x$ ($2 \leqslant x \leqslant 26$) nanoparticles using mechanical alloying, which resulted in impurity phase segregation in some of the compositions. Zhang *et al.*, [ZHAN2005] showed that Co_2FeSn can't be synthesized as a single phase form using conventional arc-melting method due to phase separation of constituents into Co_3Sn_2 and CoFe phases as the formation energy of those binary phases are less than that of Co_2FeSn. As Fe_2CoSn, has the same constituent elements as Co_2FeSn, it also faced the same impediment [PATH2023].

1.2.2. Electrodeposition: a viable technique for Sn based Heusler alloys

Co_2FeSn and Fe_2CoSn display a lot of intriguing properties, and their potential application across multiple fields highlights the importance of synthesizing these materials in low-dimensional forms, such as thin films [DUAN2013, GALD2020, GAOS2015, FALE2017, PATH2022, PATH2023, PATH2024, NOKY2018, TANA2012]. Being a non-equilibrium technique, electrodeposition enables the preparation of thermodynamically unstable phases like Co_2FeSn and Fe_2CoSn [DUAN2013, GAOS2015, PATH2022, PATH2023, WATA2015]. The rapid kinetics of the process allow for the deposition even at room temperature, offering a distinct advantage over many conventional physical vapour deposition (PVD) techniques. Additionally, Electrodeposition offers several advantages over vacuum-based techniques, including a simpler and more cost-effective experimental setup, as well as scalability for large-scale fabrication [DUAN2013, WATA2015, CHIS2007].

1.2.3. Electrodeposition of Co-Fe-Sn and Fe-Co-Sn Heusler alloys

Chrisholm *et al.* [CHIS2007] synthesized Sn-Co-Fe alloy using the galvanostatic electrodeposition technique with a gluconate bath. Structural analysis revealed that the alloy exhibited an amorphous nature. Their study further investigated the effects of current density, deposition time, pH, and deposition temperature on the structural properties and magnetic anisotropy of the alloy. Duan *et al.* [DUAN2013] reported the synthesis of Co_2FeSn alloy with *A*2-type crystal structure using constant current mode. The resulting alloy film exhibited granular morphology having soft ferromagnetic nature, with M_s of 4.5 μ_B/f.u. at 5 K and H_c of 32 Oe. They also discussed the relationship between the microstructure and magnetic properties of the deposited films. Later, Watanabe *et al.* [WATA2015] prepared the Co_2FeSn alloy film *via* potentiostatic mode and investigated the influence of deposition potential on the composition of constituent elements, surface morphology, and magnetic properties of the alloy. Karim *et al.* [KARI2020] prepared Co_2FeSn HA films in submicron thickness with *B*2-type partial disordered structure. They reported that the magnetic anisotropy values obtained from magneto-optical Kerr rotation measurements were comparable to those of highly ordered Co based HA films synthesized using conventional vacuum-based techniques. Subsequently, the same research group electrodeposited Co_2FeSn film on the single crystal substrate and investigated the intrinsic magnetization dynamics using time-resolved magneto-optical Kerr effect measurements under femtosecond laser excitation. Their study revealed key parameters such as ultrafast demagnetization time, rapid remagnetization time, and magnetic damping behaviour, as well as their correlation [KARI2021]. Gao *et al.* [GAOS2015] prepared thick Fe_2CoSn film with *A*2-type fully disordered crystal structure by electrodeposition technique and reported the effect of deposition time and electrolyte pH on the morphology of the film. Further, they reported that the films exhibit room temperature M_s and H_c of 3.5 μ_B/f.u. and 48 Oe, respectively.

Apart from this, Co_2FeSn nanowires from the electrodeposition technique have been reported by different research groups. Lu *et al.* [LUHO2018] prepared Co_2FeSn nanowires (30 - 60 nm diameter) *via* the direct current electrodeposition method, reporting soft ferromagnetic behavior with the easy magnetization axis perpendicular to the length of the wire. Galdun *et al.* [GALD2020] synthesized Co_2FeSn nanowires *via* template-assisted electrochemical deposition and reported the polycrystalline nanowires with partially disordered *B*2-type structure having lattice parameter of 5.80 Å. In these samples, the easy magnetization axis was aligned with the nanowire axis, and the experimentally obtained $P \geq 85\%$, confirming the

preservation of high spin polarization in the nanoscale regime. Khan *et al.* [KHAN2018] synthesized Fe_2CoSn nanowires using the alternating current electrodeposition method. The prepared nanowires exhibited diameter of 40 - 60 nm and length of ~15 μm. The average grain size of nanowires was ~35 nm, while the M_s of 488 μemu and a H_c of 460 Oe.

1.3. Motivation and Objectives

The available literature reveals several gaps that must be addressed to fully harness the potential of Co-Fe-Sn and Fe-Co-Sn electrodeposited HA films for practical applications. Some of the short-comings of the published work are listed below:

- Many authors were unable to achieve the fully ordered $L2_1$ structure in their synthesized Co_2FeSn films leading to low M_s and T_C. They could obtain either $B2$ or $A2$-type disordered structures with correspondingly inferior properties [DUAN2013, WATA2015, KARI2020].
- Structural, morphological, and magnetic properties of Co_2FeSn film have not been studied as a function of film thickness [DUAN2013, WATA2015].
- On the theoretical front, electron correlations have not been considered in the computational studies of Co-Fe-Sn and Fe-Co-Sn alloys [MATS2017, OZDO2007].
- The effect of introducing a fourth element on the half-metallicity of ternary Co-Fe-Sn HA has not been explored.
- There are no assessments of highly ordered Fe_2CoSn films for high-temperature magnetic and spintronic applications [GAOS2015].

This thesis work aims to bridge the existing gap in the literature on Co-Fe-Sn and Fe-Co-Sn electrodeposited HA films by focusing on the following key aspects:

- Synthesis of highly ordered stoichiometric Co_2FeSn and Fe_2CoSn films by electrodeposition and assessment of their structural, morphological, electronic and magnetic properties.
- Exploring strategies to improve the half-metallic properties of Co-Fe-Sn HA films by composition variation and atomic substitution.
- Understanding the role of fourth element substitution on the structural, morphological, magnetic, and half-metallic properties of electrodeposited Co_2FeSn films.

Recognizing this gap in the literature, we adopted a low-cost, non-equilibrium electrodeposition technique to successfully fabricate stoichiometric Co_2FeSn alloy films with improved structural, morphological, and magnetic properties. In addition, compositional

variations and the introduction of a fourth element were explored to induce half-metallicity in the non-half-metallic Co_2FeSn HA film. Furthermore, highly ordered Fe_2CoSn HA films were synthesised, and their structural, morphological, magnetic, and electronic properties were systematically investigated to evaluate their potential for various applications.

1.4 Outline of the thesis

The details of the contents of the next seven chapters of thesis are as follows

- Chapter 2 of the thesis presents the experimental methodologies employed for sample fabrication and characterization of the samples along with the theoretical calculations performed to estimate their magnetic and electronic properties.
- Chapter 3 of the thesis focuses on $L2_1$-ordered stoichiometric Co_2FeSn HA film and provides a detailed analysis of its structural, morphological, magnetic, and electronic properties.
- Chapter 4 of the thesis emphasizes on thickness-dependent structural, morphological, and magnetic properties of ordered stoichiometric Co_2FeSn films.
- Chapter 5 of the thesis is devoted to inducing half-metallicity in non-half-metallic Co_2FeSn HA film by tuning its composition. A comprehensive study of the structural, morphological, magnetic, electrical, and electronic properties of the films are described in this chapter.
- Chapter 6 of the thesis explores the introduction of half-metallicity in non-half-metallic $Co_{48.4}Fe_{21.9}Sn_{29.7}$ alloy film by small amounts of Cr substitution for Fe.
- Chapter 7 of the thesis focuses on $L2_1$-ordered stoichiometric Fe_2CoSn HA film and provides a detailed analysis of its structural, morphological, magnetic, and electronic properties.
- Chapter 8 provides a summary of the key findings and proposes potential directions for future research in these areas.
- All references cited in the thesis and the list of publications are presented at the end.

Chapter 2

Experimental and Theoretical Methodologies

The fabrication process plays a vital role in deciding the quality, quantity and viability of a material and its commercial application potential since each synthesis approach offering distinct advantages and limitations. At the preliminary laboratory scale of sample production, it is crucial to select a synthesis technique that maximizes material quality while minimizing property compromises. This chapter presents a concise overview of the challenges involved in various techniques for synthesizing HA films. This is followed by an outline of the procedure employed in this thesis to synthesize the desired HA films. This chapter also provides detailed description of the characterization techniques employed to analyze the properties of the HA films and assess their application potential. The theoretical calculations conducted to forecast, support, and validate the experimental data are also presented towards the end of the chapter.

2.1. Synthesis of Heusler alloy films

Methods available for the synthesis of HA films can be broadly classified into physical and chemical techniques [DUBO2007, DUAN2013, KARI2020, KURF2003]. Physical deposition techniques include magnetron sputtering, molecular beam epitaxy, pulsed laser deposition, and electron beam evaporation, where the deposition takes place after the material to be deposited has been transferred to a gaseous state either by an evaporation or ion impact process [MODA2017, PATR2019, QIAO2013, SUHA2010]. On the other hand, chemical methods consist of techniques such as electrodeposition, controlled precipitation, and chemical bath deposition, which basically involve chemical reactions and processes [DUAN2013, KARI2020, MARI2012]. Among these techniques, electrodeposition (or electrochemical deposition) stands out due to its numerous advantages. It is a cost-effective method that operates under ambient, non-vacuum conditions, requiring relatively simple instrumentation, lower operational costs, and offers scalability for large-area or industrial-scale fabrication [CHIS2007, DUAN2013]. The rapid kinetics of the chemical process facilitates deposition at room temperature, apart from providing significant advantages over many conventional physical vapour deposition (PVD) methods [DUAN2013, WATA2015]. Moreover, the non-equilibrium nature of the electrodeposition process enables the formation of

thermodynamically unstable phases, such as Co_2FeSn and Fe_2CoSn HAs, which are challenging to synthesize using conventional techniques like arc melting [DUAN2013, PATH2022, PATH2023, WATA2015]. A detailed discussion of the electrodeposition technique and the preparation of HA films using this method is presented below.

2.1.1. Electrodeposition

Electrodeposition is an electrochemical technique used to deposit solid materials onto the surface of conductive substrates. By applying an electric current, positively charged ions in an electrolyte solution are reduced and deposited as a uniform thin film on a conducting substrate maintained at a negative potential [BREN1963, ZANG2015]. This method is extensively used in industrial coating processes for both decorative and protective purposes [DUAN2013, GRIS2022, ZANG2015]. Over time, electrodeposition has developed into a highly advanced technique, capable of producing metallic alloy films with structural and magnetic properties comparable to those of thermally synthesized counterparts [PATH2022, ZANG2015].

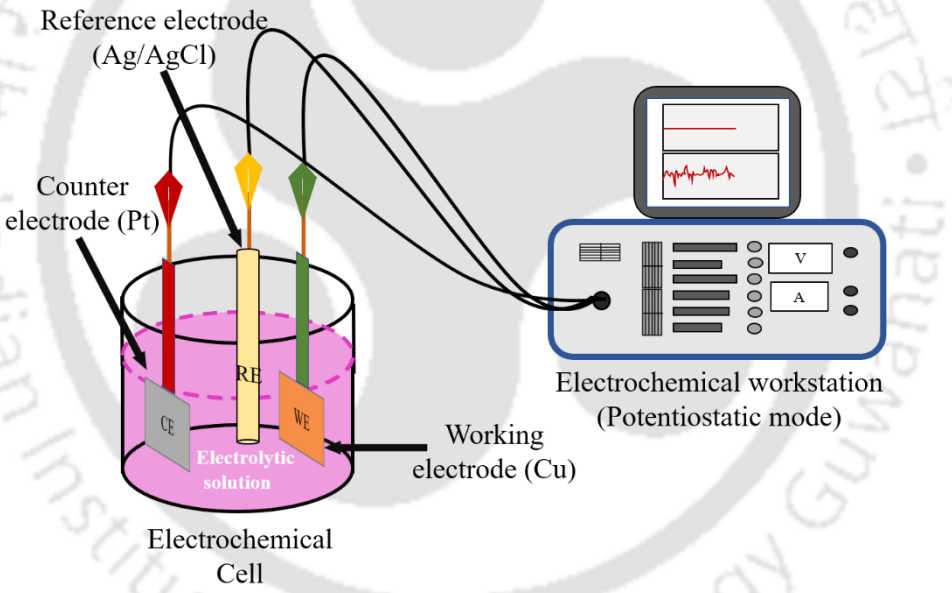

Figure 2.01. Schematic representation of electrodeposition in potentiostatic mode.

Electrodeposition of metals or alloys can be carried out using two methods, namely, the two-electrode system, commonly known as the galvanostatic deposition method, and the three-electrode system, which is usually referred to as the potentiostatic deposition method [DUAN2013, PATH2023, WATN2015]. In galvanostatic deposition, a constant current is applied between the working electrode (cathode) and the counter electrode (anode), with both immersed in an electrolytic solution containing metal salts. The applied current drives the reduction of metal ions in the salt solution at the working electrode, resulting in the formation

of a metal or alloy film on its surface [DUAN2013, NASI2017]. In potentiostatic mode, the experimental setup includes three electrodes, namely, a working electrode (WE), a counter electrode (CE), and a reference electrode (RE). In potentiostatic electrodeposition, an alloy film is deposited onto a substrate by maintaining a constant potential with respect to the RE. This fixed potential drives the electrochemical reduction of metal ions in the electrolyte, enabling the formation of a metal or alloy layer on the conducting substrate serving as the WE [BREN1963]. A schematic representation of a typical potentiostatic electrodeposition set-up for depositing metallic alloy films is shown in Figure 2.01.

2.1.1.1 Electrodeposition of Heusler alloy films

Let us consider the synthesis of Co_2FeSn HA film as an example in describing the methodology employed in this thesis work. Co_2FeSn films were electrodeposited on 0.2 mm thick polycrystalline 99.99% pure copper substrate (WE) using CorrTest Electrochemical workstation (model # CS300) operated in potentiostatic mode with 3.5 M Ag/AgCl as RE and a high purity Pt plate as CE. The separation between the CE and WE was 20 mm. Figure 2.02 depicts the experimental set-up used in this research work.

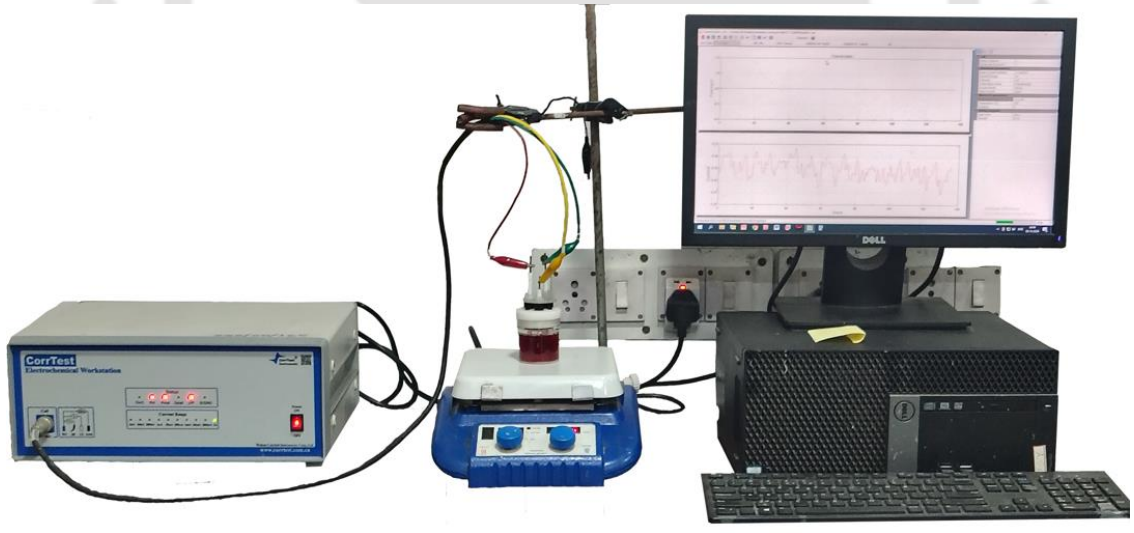

Figure 2.02. Experimental set-up for potentiostatic electrodeposition of HA films.

The electrolytic solution (or electrolyte) was first prepared by sequentially adding the following precursors and additives in 125 ml of ascorbic acid stabilized deionized water under constant (140 r.p.m.) stirring at room temperature. 3.8518 g of $CoSO_4.7H_2O$ (purity $\geqslant$ 99%, Loba Chemie Pvt. Ltd.), 1.7040 g of $FeSO_4.7H_2O$ (purity $\geqslant$ 98.5%, Merck Specialities Pvt. Ltd.) and 0.1785 g of $SnSO_4$ (purity $\geqslant$ 95.5%, Alfa Aesar) were used as precursors. 2.3190 g boric acid (purity $\geqslant$ 99.8%, Merck Specialities Pvt. Ltd.) as buffer, 2.0580 g of NaCl (purity

⩾ 99.9%, Qualigens Fine Chemicals), 15 g of sodium gluconate (purity ⩾ 98%, Loba Chemie Pvt. Ltd.) and 0.0025 g of peptone (analytical grade, Loba Chemie Pvt. Ltd.) were used as additives. The pH of the electrolyte was adjusted to 7.0 by adding an appropriate amount of 1 molar NaOH solution. Following the preparation of the electrolyte, a 10x10 mm^2 copper (Cu) substrate was mechanically polished and cleaned sequentially in dilute HCl, deionized water and acetone. The dried substrate was then immersed in freshly prepared electrolyte solution. Film deposition was performed at deposition potentials (V_{dep}) at WE ranging from -2.4 V to -5.1 V with respect to the RE for a fixed deposition time (say, t_{dep} = 300 s). The elemental composition of the films was determined using energy dispersive X-ray spectroscopy (EDS) analysis. Figure 2.03 portrays the variation of atomic percentages of transition metals (Co and Fe) and *s-p* element Sn in Co-Fe-Sn films prepared under different V_{dep} for t_{dep} of 300 s. As we move towards lower negative V_{dep}, the atomic percentage of Co and Fe decreases, while that of Sn increases. To understand the nature of the individual elemental deposition and to arrive at an appropriate V_{dep} for depositing the desired amount of each element in the alloy, the whole range of V_{dep} can be divided into two regions, namely, X and Y, based on the Sn content as shown in Figure 2.03. In the lower negative V_{dep} region (or X region), Sn content dominates over that of the transition metals (Co and Fe) content because the nobler element (*i.e.*, the element with the least negative electrode potential) electrodeposits more easily than the less noble elements (*i.e.* elements with higher negative electrode potential) [PATH2022, WATA2015]. In the case of Co-Fe-Sn alloy electrodeposition, the value of the standard electrode potential (V_{sep}, which is the equilibrium potential of an electrode in contact with an electrolyte with respect to standard hydrogen electrode, when all components of the specified electrochemical reaction are in their standard states *i.e.*, a pressure of 1 atm., temperature of 298 K, and 1 M solute concentration) of Sn is lower (-0.14 V) than that of both the transition metals Co (-0.27 V) and Fe (-0.44 V) with respect to standard hydrogen electrode (a RE used to establish a zero potential reference point against which the electrode potential of other electrodes can be measured) [BRAT1998, BREN1963]. This is the reason for the dominance of Sn content in the X region. In contrast, at higher negative V_{dep} region (or Y region), the Sn content starts to decrease as compared to the transition metals Co and Fe. In this region, Co electrodeposition is preferred over Fe because of two reasons: (i) Co is nobler than Fe, and (ii) the concentration of Co metal ions is higher than that of Fe metal ions due to higher precursor amount of Co as compared to Fe in the deposition bath [PATH2022, WATA2015]. It can be seen in Figure 2.03 that the film deposited at -4.0 V gives the average composition of Co:Fe:Sn of 49.8:23.3:26.9, which is very close to the stoichiometric target composition of

50.0:25.0:25.0. This potential is found to be appropriate for the synthesis of stoichiometric Co_2FeSn films under the said experimental conditions and electrolyte concentration [PATH2022, PATH2024].

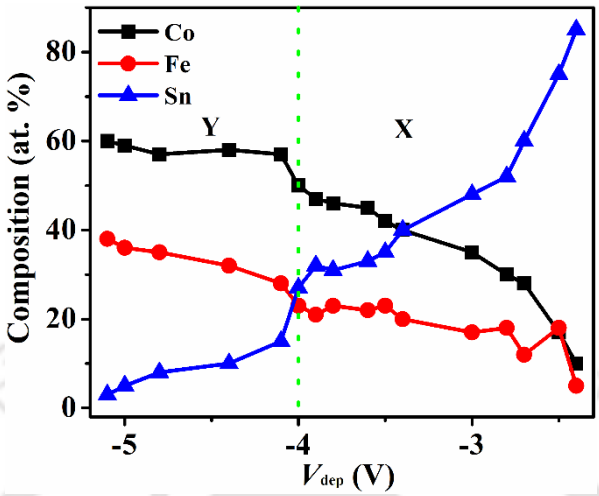

Figure 2.03. Composition variation of Co, Fe, and Sn content (at.%) in the deposited Co-Fe-Sn films as a function of V_{dep}.

The reaction mechanism involved in the formation of Co-Fe-Sn film is described below [DUAN2013, PATH2022]:

$$2H_2O + 2e^- \leftrightarrow H_2 + 2OH^- \quad (2.01)$$

$$M^{2+} + OH^- \leftrightarrow MOH^+ \quad (2.02)$$

$$MOH^+ \rightarrow (MOH^+{}_{ads}) \quad (2.03)$$

$$MOH^+{}_{ads} + 2e^- \rightarrow M + OH^- \quad (2.04)$$

where *M* represents the metal ions of Co, Fe and Sn. Accordingly, Co, Fe, and Sn ions are reduced, and the active ions react with each other to form Co-Fe-Sn alloy film.

2.1.1.2. Film thickness measurement

The deposition rate associated with the potentiostatic electrodeposition technique is required to obtain films of varying thicknesses. The deposition rate was calibrated using a surface profilometer (Veeco, Dektak-150). Stylus profilometers are versatile instruments that measure film thickness by quantifying step heights or trench depths on the substrate surface. Stylus profilometers employ a fine stylus that traverses the sample surface either by movement of the stylus itself or the stage to perform linear surface scans. As the stylus moves across the surface, it deflects vertically in response to surface features, enabling the measurement of parameters such as surface roughness and film thickness [MODA2018a]. To monitor the thickness of the deposited films, a fine insulating strip was adhered to the top of the cleaned Cu substrate prior

to deposition. This effectively masks the part of the substrate from deposition. After the completion of the film deposition, the insulating strip was carefully removed using acetone. This process exposed a well-defined step edge between the deposited film and the uncoated substrate. The resulting step height was then measured using a stylus surface profilometer, and a typical scan profile is shown in Figure 2.04.

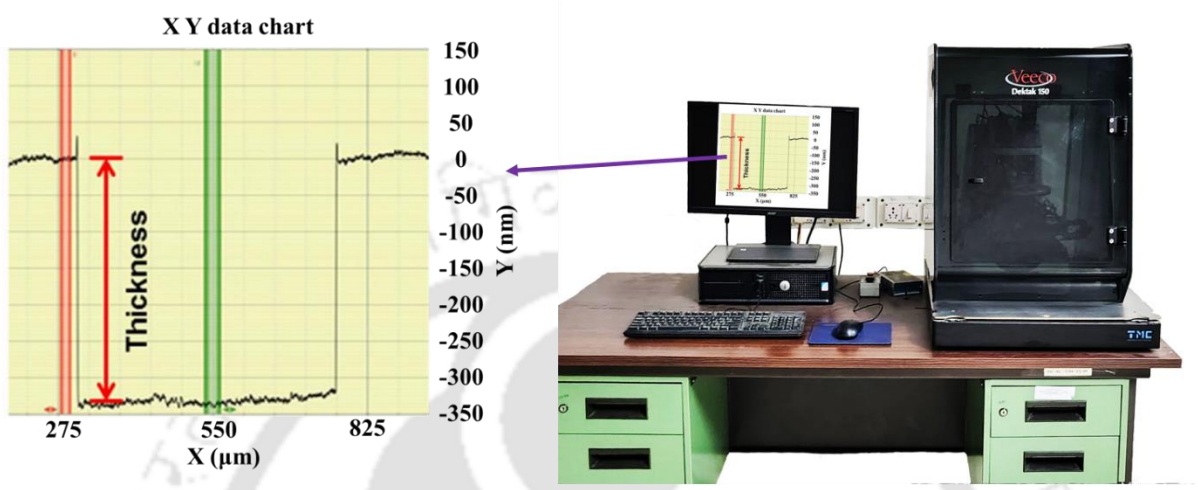

Figure 2.04. Photograph of the Veeco Dektak 150 surface profilometer. The image on the left provides an enlarged view of the scanned profile, where the red arrow indicates the film thickness as determined by the measured step height.

An alternative approach to determine the thickness of the deposited film involves cross-sectional imaging using field emission scanning electron microscopy (FESEM). For accurate measurement, the sample must be vertically mounted, with a clearly distinguishable interface between the film and the substrate, along with a clean, smooth cross-sectional surface. To achieve this, the cross-section was carefully polished using fine-grit emery paper until a sharp interface was revealed. It was subsequently cleaned with acetone to remove any residual debris. Following this, the sample was vertically mounted on the FESEM stub using carbon tape as schematically illustrated in Figure 2.05 (a). High-resolution cross-sectional images showing the film thickness were then acquired using FESEM. The underlying imaging mechanism employed during FESEM operation is discussed in detail in a later section of this chapter. Film thickness was subsequently calculated from the captured images using ImageJ software. Figure 2.05 (b) displays the cross-sectional image of the Co_2FeSn HA film having a thickness of 320 nm.

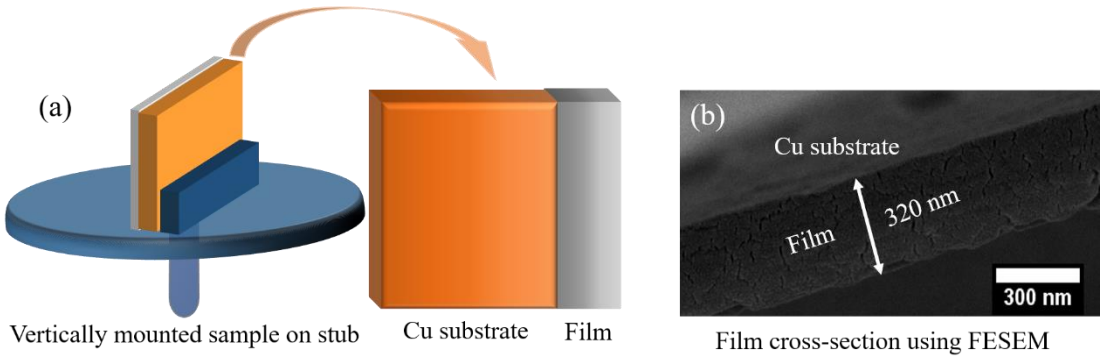

Figure 2.05. (a) Schematic view of a sample (film on Cu) mounted on FESEM stub for film thickness measurement. (b) Cross-sectional FESEM image of a Co_2FeSn film on Cu substrate.

2.1.1.3. Post-deposition processing

Since electrodeposition is generally rapid, it does not allow proper crystallisation of the deposited films. In order to improve the crystallinity of the as electrodeposited films, heat treatment under optimized conditions has to be provided. Since metallic alloys cannot be heat treated in open air due to the risk of oxidation, the films were first cleaned with acetone, and then placed inside fused silica ampoules. These ampoules were evacuated down to a pressure of ~10^{-3} Pa using a high vacuum pumping station consisting of a combination of oil-based diffusion and rotary pumps (Make:Vacuum Technique Pvt. Ltd., India) shown in Figure 2.06 (a).

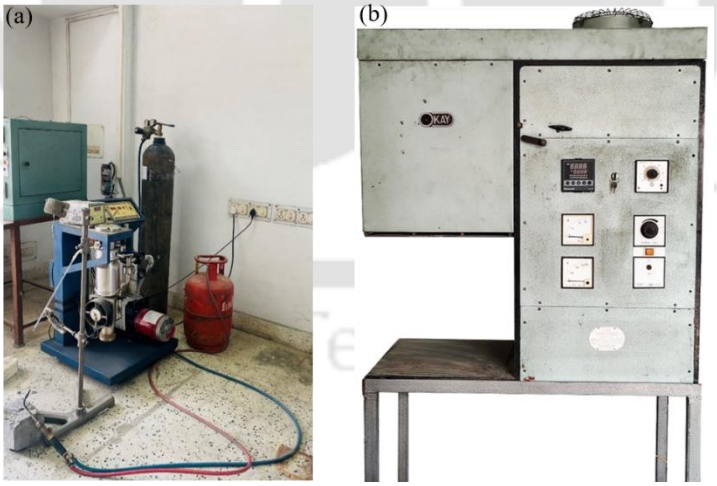

Figure 2.06. Photographs of (a) ampoule vacuum sealing setup, and (b) raising hearth furnace.

The evacuated ampoules were then sealed at the neck using a neutral flame produced by a mixture of oxygen and liquid petroleum gas. Subsequently, the vacuum-sealed ampoules containing the samples were placed in a raising-hearth electric furnace (Make: OKAY, Model

70R4, India), illustrated in Figure 2.06 (b), and heat treated at an optimized temperature of 823 K for 60 minutes. The furnace, equipped with $MoSi_2$ heating elements, features a PID temperature controller and programmer for precise regulation of temperatures up to 1973 K.

2.2. Characterization techniques

Material characterization involves a variety of probes such as X-rays, photons, electrons, atoms and ions, whose interactions with the material provide critical insights into its intrinsic properties under various conditions. Depending on the instrument used and a specific property of interest, a broad spectrum of techniques can be employed to probe, analyse and understand the material property. The characterization techniques and instruments utilized in the present study are described below:

2.2.1. X-ray diffractometer

Knowledge of the atomic structure of a material is a fundamental and crucial step in the characterization of any material. X-ray diffraction (XRD) is a versatile analytical technique that facilitates the identification of various crystalline phases in materials and offers valuable insights into their atomic arrangements. In addition, XRD enables the evaluation of key structural parameters, including lattice constants (unit cell dimensions a, b, c, and angles α, β, γ), average crystallite size (D_v), and internal (micro)strain (ε). This technique is based on the Bragg's law of diffraction, which describes the diffraction of X-rays by the periodic arrangement of atoms in a crystal, producing distinct and informative diffraction patterns [CULL2014, MARI2020]. It is well known that a crystalline material exhibits a periodic arrangement of atoms. When incident X-rays interact with a set of parallel atomic planes within the crystal at specific angles, diffraction occurs. The constructive interference of the scattered X-rays leads to the emergence of distinct diffraction peaks corresponding to the atomic planes present in the crystal, as illustrated in Figure 2.07. The condition for constructive interference is given by [CULL2014], path difference = $n\lambda$ 2.05

where n is an integer representing the order of diffraction, and λ is the wavelength of the incident X-rays. As illustrated in Figure 2.07, the path difference between the X-ray beams 1 and 2 is given by,

$CB + BD = n\lambda$ 2.06

where d represents the interplanar spacing, and θ is the diffraction angle (also known as Bragg's angle) at which diffraction occurs

$d \sin\theta + d \sin\theta = n\lambda$ 2.07

or

$$2\,d\sin\theta = n\,\lambda \qquad 2.08$$

Eq. (2.08) is commonly referred to as Bragg's law [CULL2014].

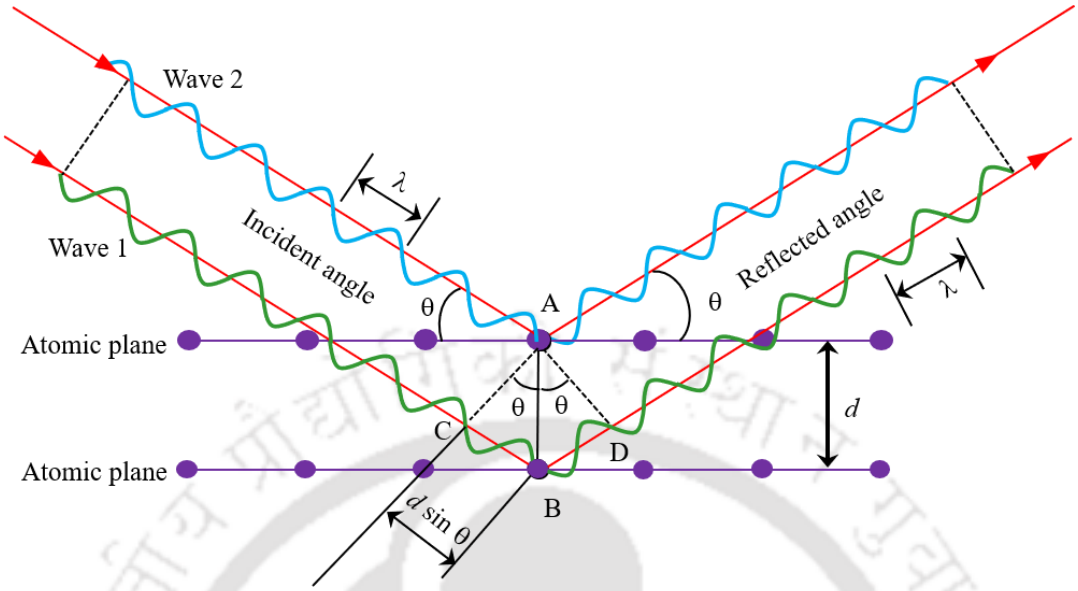

Figure 2.07. Schematic representation of Bragg's law.

Metallic alloys prepared by casting and deposition methods crystallize as polycrystalline materials. Such samples are finely powdered and investigated using a powder X-ray diffractometer. In conventional powder X-ray diffraction systems, measurements are typically performed using θ-2θ geometry, also known as Bragg-Brentano geometry. In this configuration, the sample holder remains stationary while the X-ray source and detector rotate such that the angle between the incident beam and sample surface is θ, and the angle between the incident beam and detector is 2θ. This configuration ensures that high-intensity diffraction from the specific crystallographic planes is efficiently directed towards the detector at specific angles satisfying Bragg's law. Despite its widespread use, the conventional symmetrical θ-2θ geometry presents significant limitations for thin film characterization. For example, X-rays incident at large glancing (grazing) angles can penetrate several micrometres into the material. In the case of thin films, the penetration depth may significantly exceed the film thickness, resulting in weak signals from the film and strong signals from the underlying substrate. To address this issue, thin film samples are typically analysed using a modified technique known as grazing incidence XRD (GI-XRD). In this technique, the incident angle (ω) is maintained at a low fixed value (typically between 0.5° and 3°), while only the detector moves to vary the angle between the incident and diffracted beams (2θ) [MCCA2005]. The low incident angle limits the X-ray penetration into the sample, ensuring that the resulting diffraction pattern predominantly arises from the thin film rather than the underlying substrate. This method is

especially very useful to study multi-layered films since the penetration depth can be adjusted to examine layers at different depths by choosing an appropriate ω. A schematic representation of (a) θ-2θ (Bragg-Brentano geometry) and (b) 2θ (grazing incidence geometry) is portrayed in Figure 2.08.

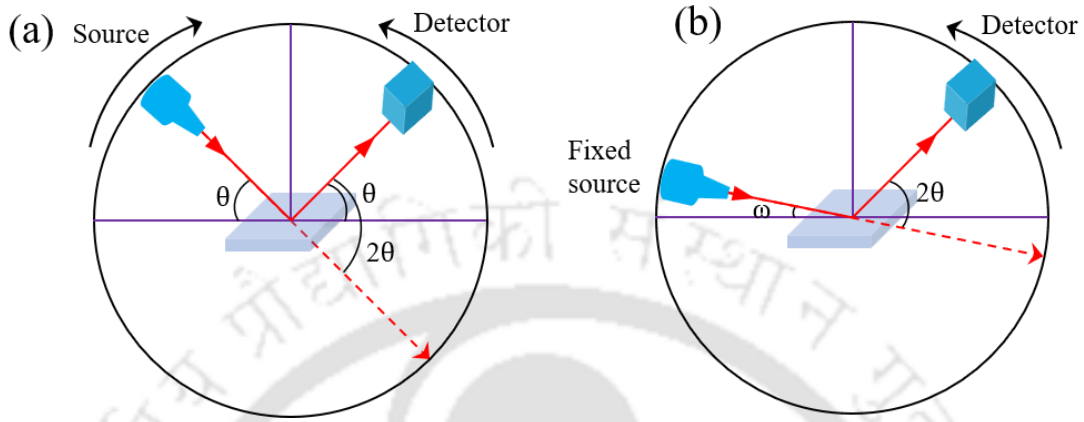

Figure 2.08. Schematic diagram displaying (a) θ-2θ geometry and (b) 2θ grazing incidence geometry with fixed ω.

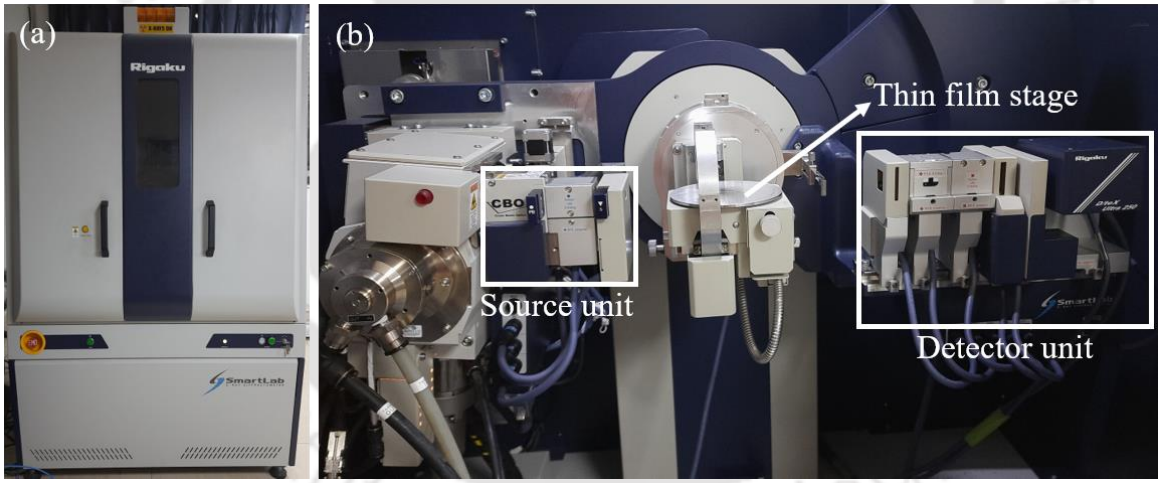

Figure 2.09. Image of (a) Rigaku Smartlab X-ray diffractometer and (b) source unit, thin film stage, and detector unit in 2θ grazing incidence geometry with fixed ω.

The picture in Figure 2.09 (a) shows a Rigaku SmartLab X-ray diffractometer and Figure 2.09 (b) provides a magnified view of the X-ray source, thin film stage, and detector unit (D/teX Ultra 250 detector). In this work, XRD measurements were performed on thin film samples in grazing incidence mode (2θ scan with fixed ω), using Cu-Kα radiation (wavelength λ = 1.5406 Å) operating at 9 kW (45 kV/200 mA).

The lattice constants, *a*, *b*, *c*, of a crystalline unit cell are related to the interplanar spacing d_{hkl} characterized by the Miller's indices (*h k l*) through the following relation [CULL2014],

$$\frac{1}{d_{hkl}^2} = \frac{h^2}{a^2} + \frac{k^2}{b^2} + \frac{l^2}{c^2} \qquad 2.09$$

For crystalline materials with cubic unit cell for which *a* = *b* = *c*, eq. (2.09) can be simplified to [CULL2014],

$$\frac{1}{d_{hkl}^2} = \frac{h^2+k^2+l^2}{a^2} \qquad 2.10$$

The intensity of the X-rays reflected from each crystal plane is determined by the structure factor [CULL2014],

$$F = \sum_{i=1}^{N_{eff}} f_n \, e^{2\pi i\,(hx_i + ky_i + lz_i)} \qquad 2.11$$

Here f_n represents the atomic scattering factor of the n^{th} atom and N_{eff} denotes the effective number of atoms in the unit cell with fractional coordinates (x_i, y_i, z_i), where [CULL2014],

$$N_{\text{eff}} = \frac{1}{8}N_c + \frac{1}{2}N_f + 1\,N_i \qquad 2.12$$

Here, N_c, N_f, and N_i represent the number of atoms located at the corners, faces, and interstitial positions of the unit cell, respectively. For a face centred cubic (fcc) unit cell, N_c = 8, N_f = 6, N_i = 0, yielding an effective number of atoms N_{eff} = 4. These four equivalent atoms are positioned at fractional coordinates (0,0,0), (½ ½ 0), and (0 ½ ½). Consequently, eq. (2.11) can be rewritten as [CULL2014],

$$F = f\,[1 + e^{\pi i(h+k)} + e^{\pi i(k+l)} + e^{\pi i(l+h)}] \qquad 2.13$$

The above equation yields a non-zero value only when the Miller indices (*h k l*) are unmixed, *i.e.*, when all the indices are either even or all odd. This condition leads to the appearance of reflections from planes such as (111), (200), (220), (311), (222), (400), (331), (420), (333), (511), and so on in the XRD pattern of a HA. These planes can be identified by combining eqs. (2.08) and (2.10) for *n* = 1 as,

$$\frac{sin^2\theta}{h^2+k^2+l^2} = \frac{\lambda^2}{4\,a^2} \qquad 2.14$$

The right-hand side (RHS) of eq. (2.14) remains constant for a given crystal structure and a specific X-ray source. This implies that only certain planes, characterized by specific Miller indices (*h k l*), will satisfy the condition with particular angle θ, where the left-hand side (LHS) equals the RHS. In this way, all the peaks (or reflections) observed in the XRD pattern of a fcc HA system can be systematically indexed, facilitating the determination of the lattice constant.

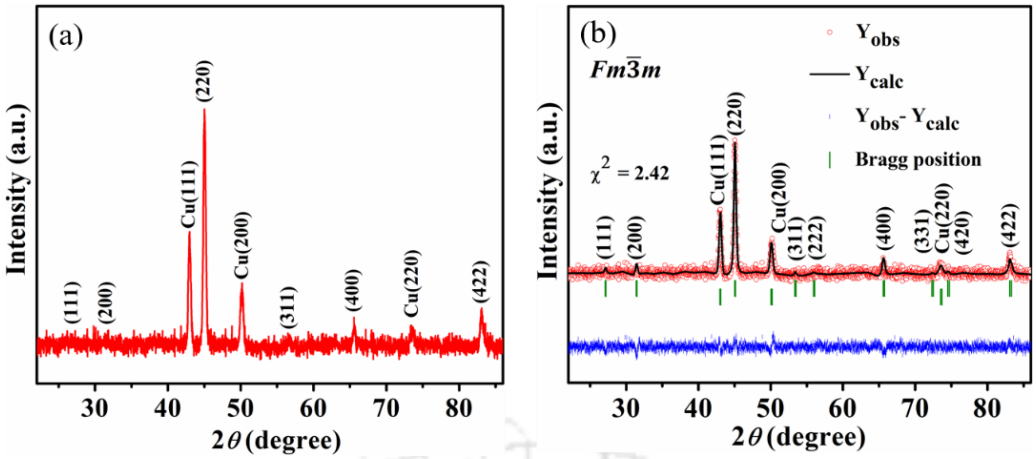

Figure 2.10. Typical XRD pattern of electrodeposited (a) $Co_{53.8}Fe_{20.6}Sn_{25.6}$ HA film, and (b) Rietveld refined XRD pattern of the $Co_{53.8}Fe_{20.6}Sn_{25.6}$ film.

Figure 2.10 (a) shows the XRD pattern of the electrodeposited $Co_{53.8}Fe_{20.6}Sn_{25.6}$ HA film, while Figure 2.10 (b) presents the Rietveld-refined XRD pattern of the same. The FullProf Suite software was used to extract various structural parameters from the experimental XRD pattern through Rietveld refinement. The refinement process helps to estimate the actual phase purity of the material and allows for better estimate of multiple crystallographic parameters, including lattice constants, bond angles, bond lengths, and detailed phase information. In this procedure, the experimental data are compared with the simulated XRD pattern generated using the proposed unit cell using the least squares method [CARV2000]. The unit cell dimensions and other fitting parameters are iteratively changed to obtain a good fit between the experimental pattern and the simulated one. The fitting quality is assessed by minimizing the parameter χ^2 representing the goodness of the fitting during the refinement cycles. Considering the ideal value of unity, χ^2 values <5 are generally claimed as indicators of good fitting. More details about the FullProf software, refinement process, and underlying theories can be found in the report by Carvajal *et al.* [CARV2000]. In Figure 2.10 (b), red circles represent the experimentally observed XRD pattern (Y_{obs}), while the black solid line corresponds to the calculated pattern (Y_{cal}) obtained through the Rietveld refinement. The nearly straight blue line is the difference (Y_{obs}-Y_{cal}) curve. The low χ^2 value (~2.42) obtained in this example is indicative of a good fitting of the experimental XRD pattern to the simulated pattern obtained for the optimized $L2_1$ unit cell.

Assuming that the atomic arrangement in a material is perfectly periodic and extends infinitely, the XRD peaks would ideally appear as Dirac delta functions at the Bragg angles. However, in practice, XRD peaks of nanocrystalline materials exhibit noticeable broadening

due to several factors, including finite crystallite size, internal strain, and instrumental limitations. Among these, nanocrystallite size plays a dominant role, with its influence commonly assessed through the full width at half maximum (FWHM) of the diffraction peaks. As the crystallite size increases, the FWHM decreases, indicating sharper peaks. The average crystallite size (D_v) of the synthesized material can be calculated using the Schërrer equation [CULL2014],

$$D_v = \frac{k\lambda}{\beta cos\theta} \qquad 2.15$$

Here, k is a shape factor, typically taken as 0.9 for spherical grains with cubic symmetry; λ (= 1.5406 Å) is the X-ray wavelength; θ is the Bragg angle; and β is the FWHM of the Bragg peak, expressed in radians. The θ value corresponding to the most intense peak of the XRD pattern is chosen for the estimate of D_v.

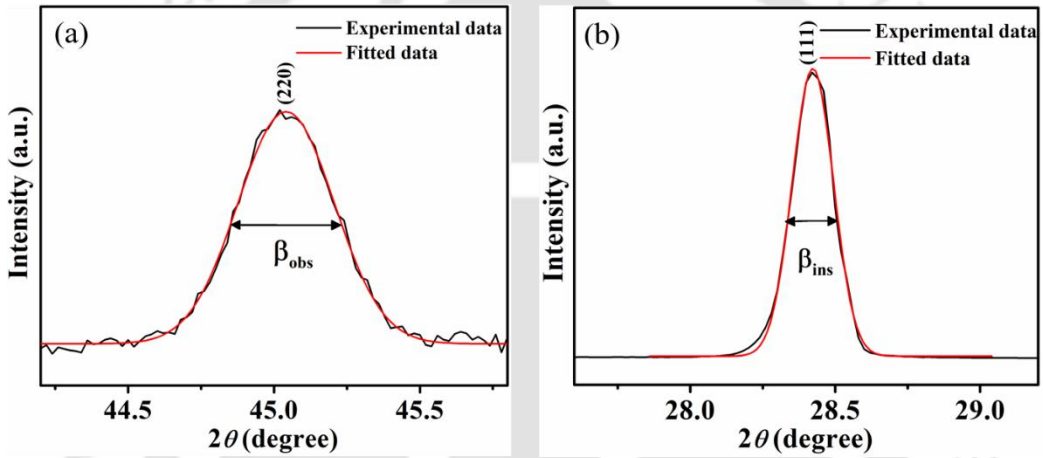

Figure 2.11. Gaussian fitting of the most intense (a) (220) peak in the XRD pattern of $Co_{53.8}Fe_{20.6}Sn_{25.6}$ alloy film and (b) (111) peak of a standard silicon sample.

The Gaussian peak profile fitting procedure used to determine β from the most intense (220) peak in the XRD pattern of $Co_{53.8}Fe_{20.6}Sn_{25.6}$ HA is illustrated in Figure 2.11 (a). The FWHM (= 0.3886°) value obtained from the fit is converted into radians (= 0.0068 rad.). This observed value of β (β_{obs}) also includes a contribution from the instrumental broadening (β_{ins}) arising from non-monochromaticity of X-ray beams, finite X-ray beam size, limitations in collimator to yield a perfectly parallel beam, and resolution (pixel size) of the detector. In order to obtain the actual FWHM (β_{act}) corresponding to the nanocrystallite size, β_{ins} should be subtracted from the β_{obs}. To obtain a decent estimate of β_{ins}, the XRD pattern of the fully crystallized standard silicon (Si) sample supplied as a reference by Rigaku is recorded under the same experimental conditions as the sample. It is presumed that the peak broadening in the

standard Si XRD pattern has a negligible contribution to crystalline size since the Schërrer equation is only applicable to assess peak broadening of nanocrystallites of size <1 μm [CULL2014] and embodies all the instrumental contributions. Hence, the FWHM (= 0.08259° = 0.001887 rad.) of the strongest Si peak (111) appearing at $2\theta \approx 28.4°$ is taken as β_{ins}. Hence β_{act} of the $Co_{53.8}Fe_{20.6}Sn_{25.6}$ film can be estimated using the relation,

$$\beta_{act} = \sqrt{(\beta_{obs}^2 - \beta_{ins}^2)} \qquad 2.16$$

Using β_{act} = (0.0065) in eq. (2.15), D_v of the $Co_{53.8}Fe_{20.6}Sn_{25.6}$ alloy film was estimated to be 23±1 nm.

2.2.2. Electron microscopes

In order to investigate the morphological and microstructural properties and validate the structural properties of the film, electron microscopes have been employed. Electron microscopes exploit the wave nature of electrons to capture images of sub-micron structures. The de Broglie wave equation relates the wavelength (λ) and velocity (v) of an electron [ZHAN2008] as,

$$\lambda = \frac{h}{mv} \qquad 2.17$$

where h is Planck's constant and m is the rest mass of the electron. Under an applied potential V (in volt), an electron acquires a kinetic energy of ½ mv^2 [ZHAN2008]. So,

$$v = \sqrt{\frac{2eV}{m}} \qquad 2.18$$

where e is the charge of the electron. From eqs. (2.17) and (2.18), one can obtain [ZHAN2008],

$$\lambda = \frac{h}{\sqrt{2meV}} \qquad 2.19$$

Substituting $h = 6.625\times10^{-34}$ J/s, $m = 9.11\times10^{-31}$ kg and $e = 1.6\times10^{-19}$ C in eq. (2.19), one can obtain the following relation for λ of electrons (in nm) in terms of V (in volt) [ZHAN2008],

$$\lambda = \frac{1.23}{\sqrt{V}} \qquad 2.20$$

The working potential (usually ~3 - 20 kV for scanning mode and ~200 kV for transmission mode) results in λ values of ~0.022 - 0.009 nm for scanning mode and ~0.003 nm for transmission mode. Since the electrons have considerably lower wavelengths than visible light (λ = 400 – 700 nm), electron waves provide better resolution of the image of sub-micron structures as compared to optical microscopes [ZHAN2008]. Electron beams are used in both reflection and transmission geometries and in elastic and inelastic scattering geometries to explore various features of nanostructures.

2.2.2.1. Field emission scanning electron microscope

Field emission scanning electron microscope operates on the same principles as scanning electron microscope (SEM), with the primary difference being the electron generation system. FESEMs use a field emission gun (FEG) as the electron source, which generates the electron beam by applying a potential gradient, whereas SEM relies on thermionic emission for electron production [ZHAN2008]. When the electron beam emitted by the FEG interacts with a sample, the electrons may undergo various processes, such as scattering, absorption, or transmission through the material, as depicted in Figure 2.12. FESEM is specifically designed to analyze the scattered electrons produced during these interactions with the sample.

When a loosely bound outer electron of the sample interacts with the incoming incident electron, secondary electrons are produced as portrayed in Figure 2.13 (a). These secondary electrons are primarily emitted from regions close to the surface of the sample and utilized to construct the topographic image of the sample. However, as shown in Figure 2.13 (b), the backscattered (or reflected) electrons are the result of the elastic scattering of the incoming electrons with the sample. These are high energy electrons that can travel through more depths as compared to the secondary electron and can provide contrast depending upon the atomic number of the scattering atom. In addition to outcoming electrons, the interaction of energetic incoming electrons with the specimen also results in photon emission, which can be utilized for composition analysis, which will be described later.

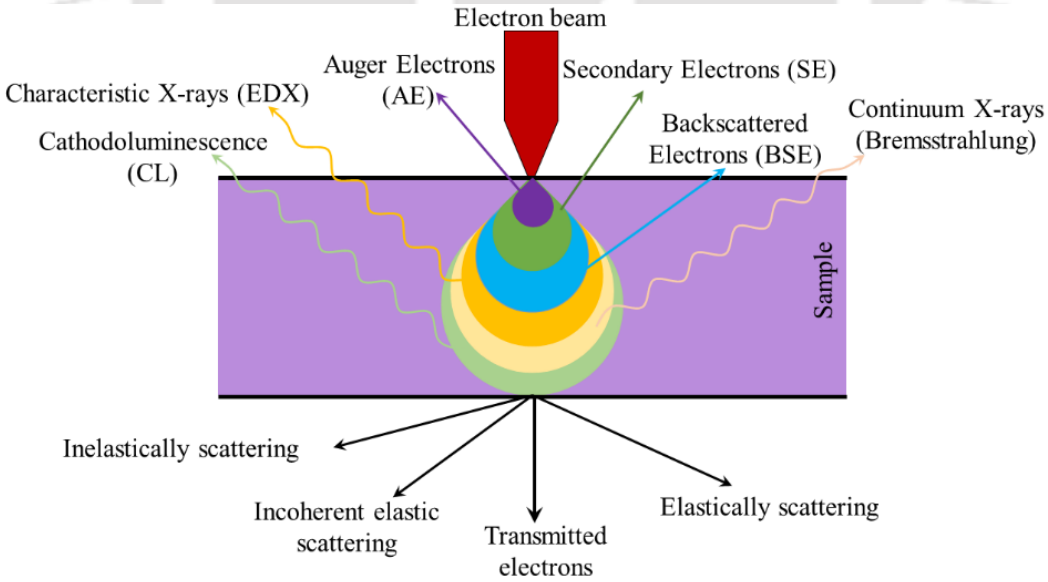

Figure 2.12. A schematic view, illustrating the interaction of electrons with the sample, and highlighting the various possible scattering processes.

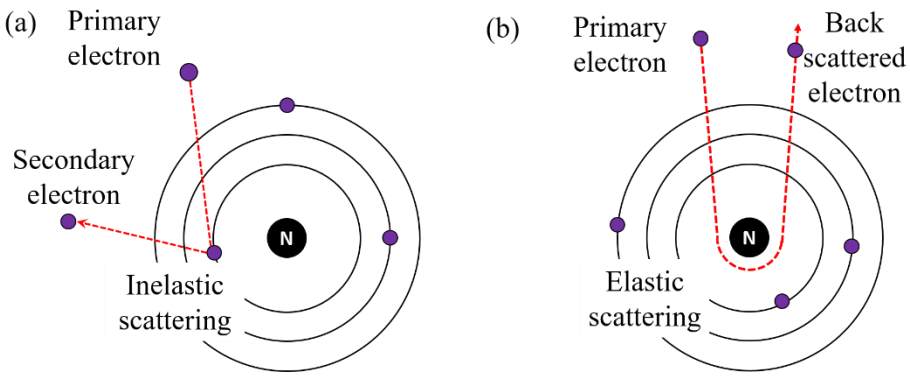

Figure 2.13. (a) Secondary and (b) backscattered electrons after interaction with a specimen.

FESEM consists of an electron source (FE electron gun), condenser lenses, objective lenses, scan coils, and detectors. The schematic diagram of a typical FESEM is shown in Figure 2.14. Field emitter is an advanced source of electron beam, which provides better resolution to the micrographs due to its reduced beam diameter as compared to the thermionic emitter. In the present study, a field emitter was used as a source of the electron beam. Thus, the instrument is named FESEM. Electron microscopes have electromagnetic lenses whose focal length can be varied by altering the current in the coil of a solenoid [ZHAN2008]. The electron microscopes are equipped with two types of lenses. The condenser lens with a large focal length is used to focus the beam on the sample [ZHAN2008]. The objective lens with a small focal length is utilized for magnification and projection of the image on the image plane [ZHAN2008]. The scan coils have the function of moving the electron beam across the specimen as required. In order to detect the scattered electrons and photons, various detectors such as Inlens and SE2 are used. A FESEM (Zeiss Gemini 300) was used in this work. The image of the instrument is shown in Figure 2.15.

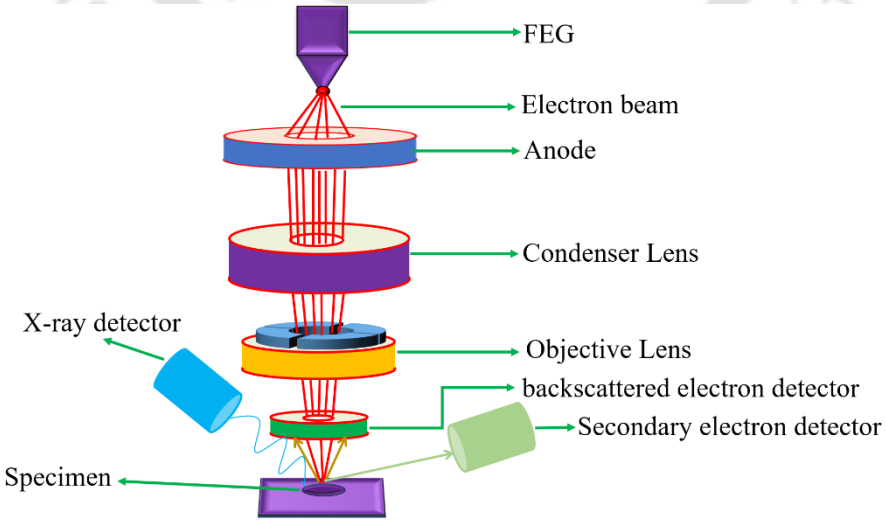

Figure 2.14. Schematic representation of a typical FESEM setup.

Figure 2.15. Field emission scanning electron microscope (Zeiss Gemini 300).

The FESEM image displaying the granular morphology of electrodeposited $Co_{53.8}Fe_{20.6}Sn_{25.6}$ HA film is shown in Figure 2.16 (a). Figure 2.16 (b) the grain size distribution of the $Co_{53.8}Fe_{20.6}Sn_{25.6}$ film with a mean grain size of 30±1 nm and FWHM of 20 nm.

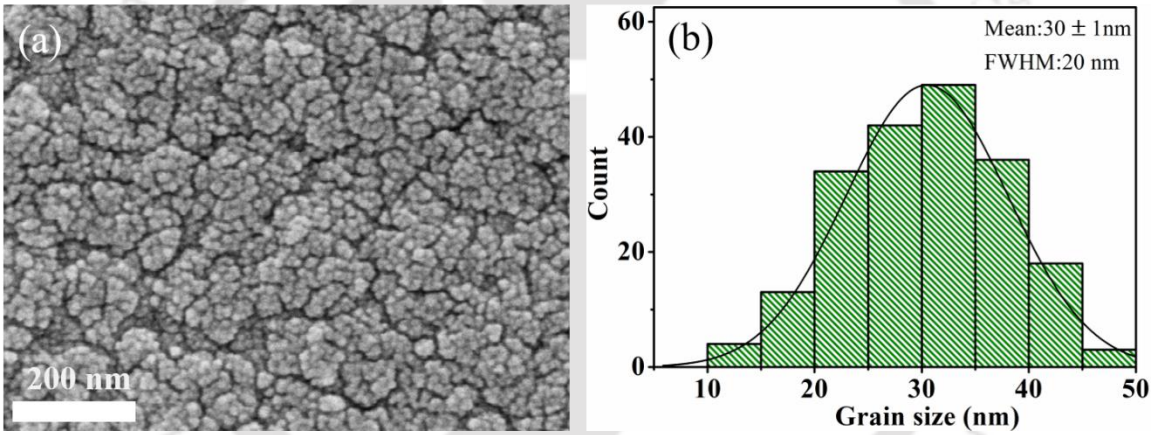

Figure 2.16. (a) FESEM image showing grain morphology and (b) grain size distribution of $Co_{53.8}Fe_{20.6}Sn_{25.6}$ alloy film.

2.2.2.2. Energy dispersive X-ray spectroscopy attachment

The next step in material characterization is to determine the elemental composition of the alloy films. The interaction of the incoming electrons with the atoms in the FESEM specimen can give rise to processes depicted in Figure 2.12. These interactions include core electron excitations, which ultimately result in the emission of X-rays, as depicted in Figure 2.17 (a). Since these are characteristic X-rays, their energies are unique to each element and can therefore be used to identify the elements present in the specimen, as well as estimate their relative concentrations. In the FESEM with an energy dispersive X-ray attachment, an X-ray detector collects these X-rays as a function of their energies. The EDS spectrum, which is a

plot of X-ray intensity *versus* energy, is shown in Figure 2.17 (b). Each peak in this spectrum is a unique characteristic of an element.

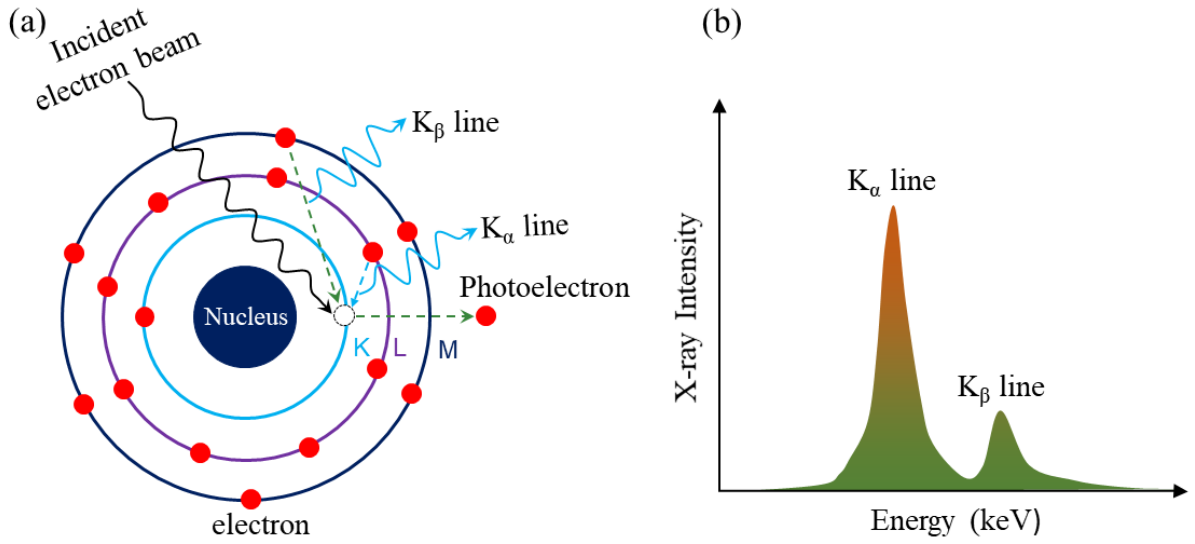

Figure 2.17. (a) X-ray generation process by the incident electrons in an FESEM and (b) the typical EDS spectrum of an element.

Figure 2.18. Image of an EDS unit attached to Zeiss Σigma FESEM.

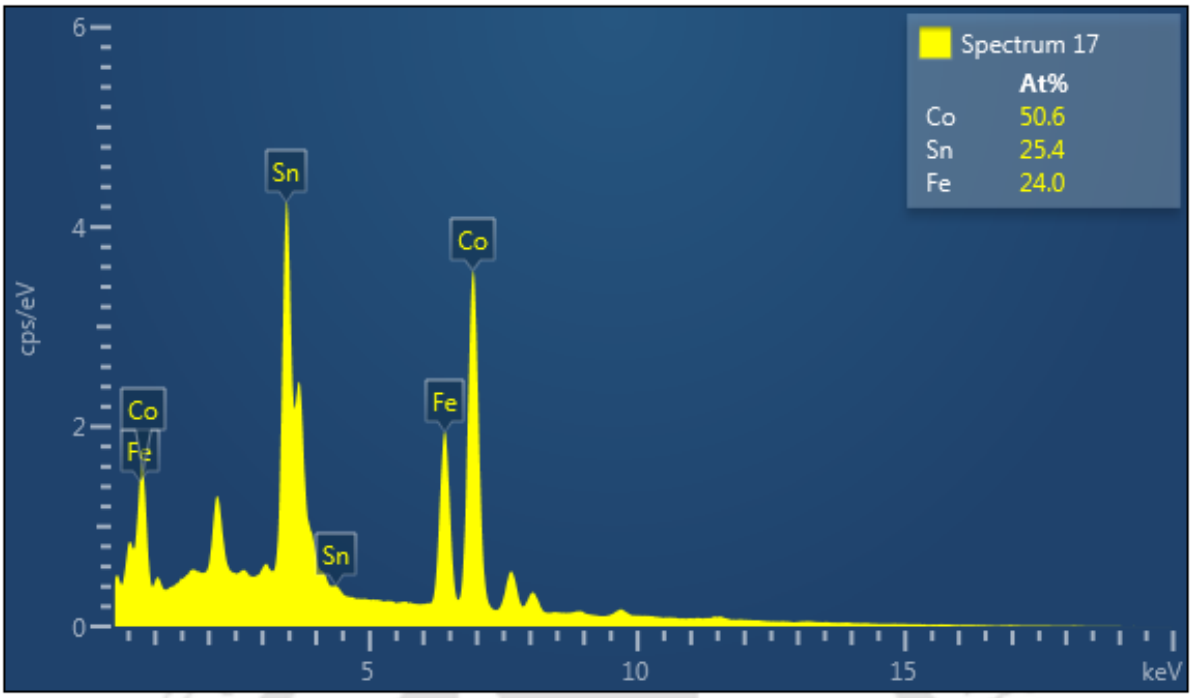

Figure 2.19. EDS data of Co_2FeSn alloy film after subtraction of data from C and Au coatings.

Figure 2.18 presents the photograph of the FESEM with EDS detector (Zeiss Σigma unit) operated under an acceleration voltage of 20 kV used for compositional analysis of the samples. Although the EDS spectrum provides elemental analysis in both weight percent (wt.%) and atomic percent (at.%), the at.% data have been used for all calculations throughout this thesis. Figure 2.19 displays a typical raw EDS spectrum of the Co_2FeSn alloy film. The detected carbon (C) peak in the spectrum originates from the carbon tape used to mount the sample on the electrode, while the gold (Au) signal arises from the conductive gold coating applied to the film surface to prevent charging effects. After excluding the C and Au contributions from the raw data, the actual elemental composition of the specimen, along with their relative percentages can be determined as illustrated in Figure 2.19. From Figure 2.19, it is clear that Co, Fe, and Sn are the only constituents and their concentrations in at.% are Co:Fe:Sn = 50.6:25.4:24.0. The overall composition of the films has been evaluated in this work by taking the average of 10 to 15 spectral scans for each sample.

2.2.2.3. Field emission transmission electron microscope

As mentioned in section 2.2.2.1, the incoming electrons in an SEM can interact with the specimen in various ways, as depicted in Figure 2.12. A portion of the incoming energetic electron beam may transmit through a thin specimen after interacting with it. In a field emission transmission electron microscope (FETEM), these transmitted electrons are imaged to

understand the atomic structure. In FETEM, electrons emitted from the field emission electron gun are accelerated and projected toward the thin specimen using electromagnetic condenser lenses. While transmitting through the specimen, the electrons (a) passes unhindered, (b) are elastically scattered with no energy loss due to the interaction of the electrons with the potential field of the atom/ion cores, leading to the construction of electron diffraction patterns, and (c) are inelastically scattered by the electron cloud, defects, dislocations, grain boundaries, etc resulting in variation in their intensities [ZHAN2008]. A series of intermediate and projector lenses are used to further magnify the transmitted electron beams, which are then projected onto a fluorescent screen. These transmitted electrons are detected to obtain various types of information about the specimen. FETEM can operate in either imaging mode or diffraction mode. Figure 2.20 schematically portrays the imaging and diffraction modes of an FETEM.

A JEOL-2100F FETEM shown in Figure 2.21 has been used in these investigations. Bright field images are generated by removing all the diffracted beams and permitting only the central beam to traverse the material. This is achieved with apertures of suitable dimensions in the rear focal plane of the objective lens. On the other side, dark field images can be generated using an aperture that blocks the central beam and all diffracted beams except a selected diffracted beam. The third imaging method involves the recombination of the primary transmitted beam with one or more diffracted beams, with careful preservation of both their phases and amplitudes. This technique is employed in high-resolution transmission electron microscopy (HRTEM) to visualize lattice planes and atomic arrangements. Consequently, HRTEM images can be used to analyze the crystallographic structure and determine the lattice parameters of the specimen. In contrast, selected area electron diffraction (SAED) is achieved by blocking the central transmitted beam using a beam stopper, allowing only the diffracted beams to contribute to the resulting diffraction pattern. For single-crystal specimens, SAED patterns display sharp, well-defined spots, whereas polycrystalline samples produce patterns composed of concentric rings made up of discrete spots [ZHAN2008].

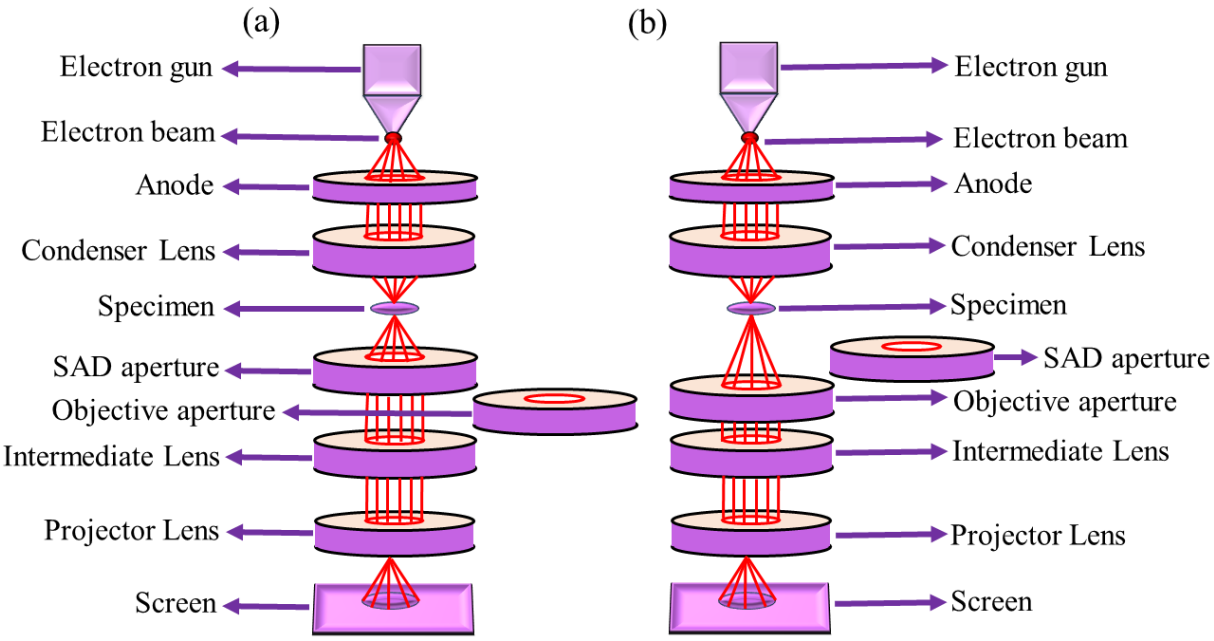

Figure 2.20. Schematic diagram of FETEM in (a) diffraction and (b) imaging mode.

Figure 2.21. Photograph of JEOL-2100F FETEM utilized in this work.

For very small θ, $\sin\theta \approx \theta$. Using this and $n = 1$ in Bragg's law (eq. (2.08)),

$$2\theta d_{hkl} = \lambda \qquad 2.21$$

Figure 2.22 shows the geometry of an SAED pattern. Here, L is the distance between the sample and the screen (camera length), and r is the radius of the circle connecting the diffraction spots from a plane (distance between transmitted and diffracted beam from a plane).

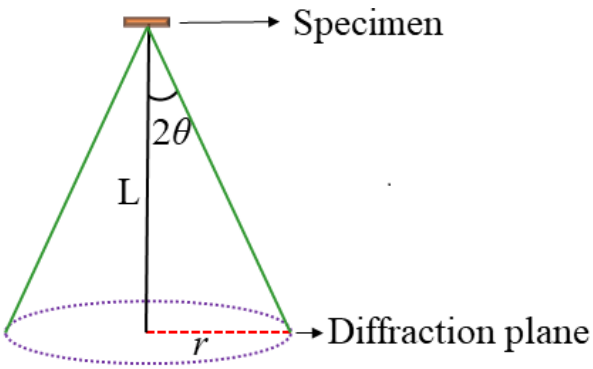

Figure 2.22. Geometry of SAED pattern in an FETEM.

From the geometry of the SAED pattern shown in Figure 2.22, for small θ, $\tan(2\theta) \approx 2\theta$, So,

$$2\theta = r/L \qquad 2.22$$

Combining eqs. (2.21) and (2.22), one can write,

$$rd_{hkl} = L\lambda \qquad 2.23$$

or $$d_{hkl} = \frac{L\lambda}{r} \qquad 2.24$$

If the FETEM is operated at say, 200 kV, then $\lambda \approx 0.003$ nm as per eq. (2.20), which is a constant. Now, L and r depend upon each other, which shows that the camera length L can modify the radius of the ring pattern for a particular plane. Adjusting the camera length allows us to control the magnification of the diffraction pattern to optimize the visibility and distinguishability of a specific diffraction spot or ring. Rewriting eq. (2.24), we get,

$$d_{hkl} = \frac{1}{\left(\frac{r}{L\lambda}\right)} \qquad 2.25$$

The length scale given in the SAED image is a measure of $\frac{r}{L\lambda}$ in nm^{-1}. Therefore, we need not calculate the individual values of r, L, and λ. By merely measuring the radius of a ring in nm^{-1} scale, one can determine the corresponding d_{hkl}. Figure 2.23 (a) displays the indexed SAED pattern and Figures 2.23 (b and c) provide the HRTEM images of (111), and (200) superlattice planes of $Co_{53.8}Fe_{20.6}Sn_{25.6}$ alloy film. Image J software was used in the analysis of FETEM images of all the samples.

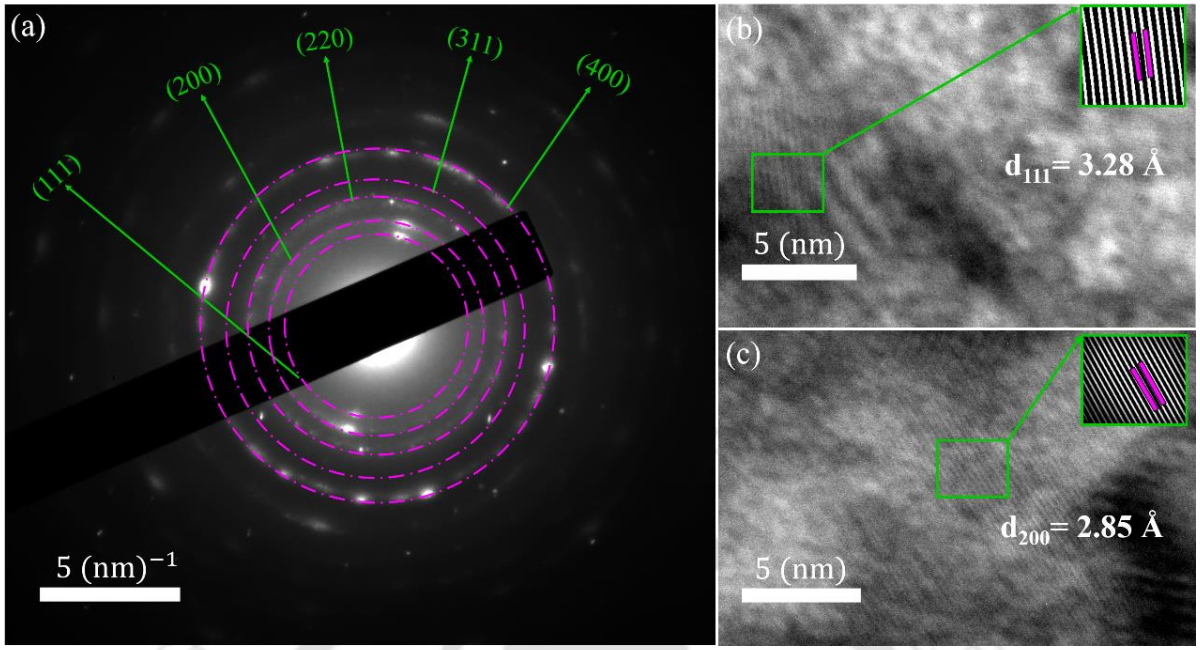

Figure 2.23. (a) SAED pattern and HRTEM images of (b) (111) and (c) (200) planes of the $Co_{53.8}Fe_{20.6}Sn_{25.6}$ alloy film. The corresponding inverse fast Fourier transformed (ifFT) images are shown as insets.

2.2.3. Vibrating Sample Magnetometer

The magnetic properties of the samples were measured using a vibrating sample magnetometer (VSM), which is based on Faraday's law for electromagnetic induction (*c.f.*, Figure 2.24). It states that the induced electromagnetic induction (ε) is proportional to the rate of change of magnetic flux through the coil [GRIF1999],

$$\varepsilon \propto -\frac{d\varphi}{dt} \qquad 2.26$$

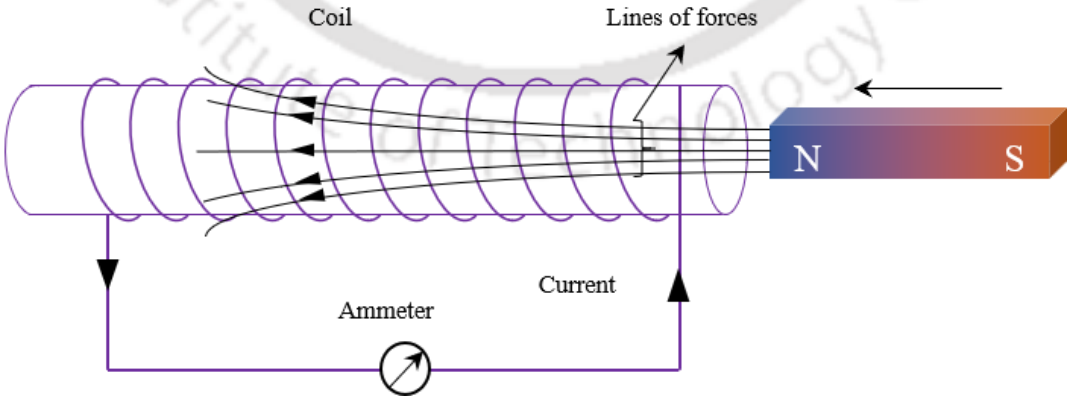

Figure 2.24. Schematic diagram demonstrating Faraday's law of electromagnetic induction.

A block diagram of a typical VSM is illustrated in Figure 2.25. The VSM comprises of the following components: (i) sample vibrator unit, (ii) sample holding rod, (iii) electromagnet and power supply, (iv) Hall probe, (v) pick up coil pairs, (vi) lock-in amplifier, (vii) control panel and (viii) computer interface. The specimen undergoing analysis is positioned in a homogeneous magnetic field and vibrated at a fixed frequency using the sample vibration exciter unit. The variation of the flux within the pickup coils due to the vibration of a magnetic specimen generates an induced electromotive force (emf) owing to electromagnetic induction. A lock-in amplifier measures the induced voltage using a reference voltage generated at the piezoelectric vibration frequency. The amplitude of the induced voltage is directly proportional to the magnetic moment of the specimen, as well as the amplitude and frequency of the vibration. Using lock-in amplifier and feedback methods, only the component of the signal originating from the magnetic moment is extracted, transformed into the unit of magnetization (*i.e.*, emu), and displayed on a digital panel [CULL2009].

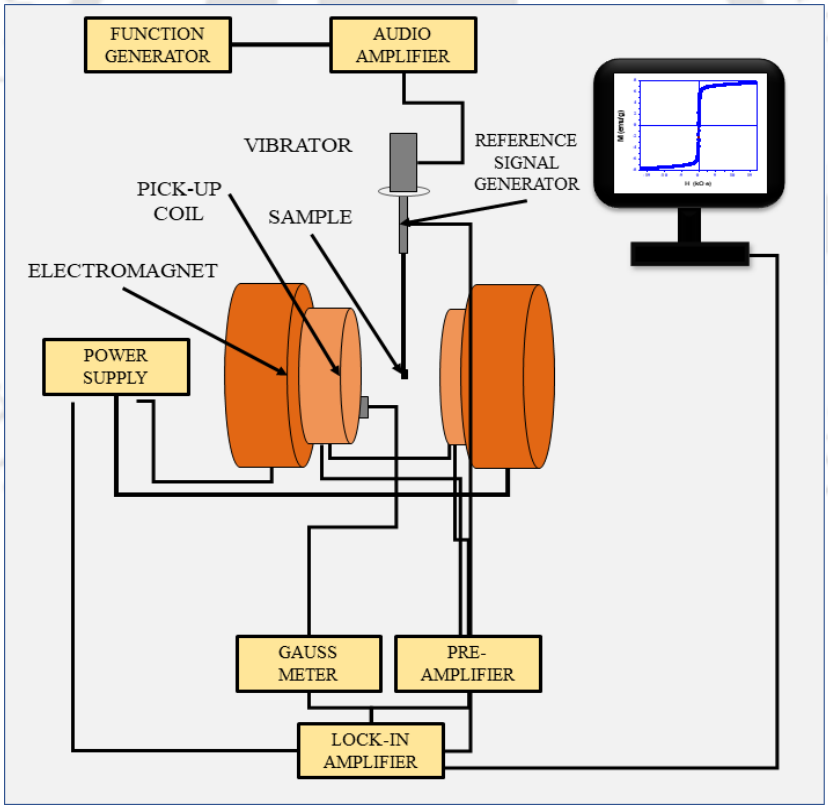

Figure 2.25. Schematic diagram portraying a typical vibrating sample magnetometer.

Figure 2.26 displays the picture of an electromagnet-based VSM (Lakeshore 7410). Figure 2.27 portrays the photograph of 9 Tesla Physical property measurement system (PPMS, Quantum Design Dynacool) based on a superconducting magnet with a VSM module attached to it.

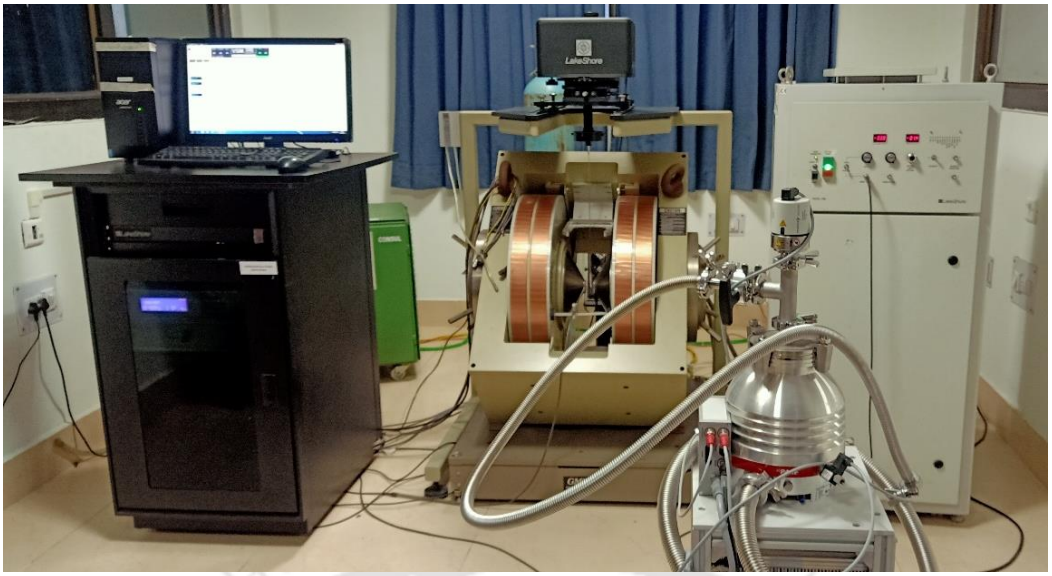

Figure 2.26. Photograph of the electromagnet-based VSM (Lakeshore 7410).

Figure 2.27. Photograph of the 9T PPMS (Quantum Design, Dynacool) with a VSM module.

The calibration of the VSM is usually done using a standard nickel sphere specimen with a known magnetic moment (M = 6.92 emu at H = 5000 Oe) prior to measurements on the samples. A program sequence is defined by the user as per the requirements in the software packaged with the instrument. The sequence is customized with optimum steps of magnetic fields (H) or temperatures (T) to gather the optimum number of data points to minimize the errors in the derived magnetic parameters (M_s, M_r, H_c, T_C, *etc.*). Many improvements have been made in the VSM instrumentation to enhance its sensitivity, utilizing the same basic concept. In the current investigations, an electromagnet based VSM was utilized for high temperature (300 – 1273 K) measurements and a 9 Tesla PPMS based VSM was utilized for the low temperature (5 – 300 K) magnetic measurements. A high temperature oven assembly and a

closed cycle refrigerator based low temperature assembly were utilized to vary the sample temperatures in VSM and PPMS, respectively. Sample holders made of polychloro-trifluoro-ethylene (Kel-F) and quartz (quartz paddle) were utilized in VSM and PPMS, respectively. For high temperature measurements, a sustainable quartz rod was utilized to hold the sample. Argon gas was continuously purged in the oven to prevent the sample from oxidising at high temperatures. To minimize temperature gradients within the sample chamber, the high-temperature assembly was evacuated to a pressure of 10^{-3} Pa. The virgin or initial magnetization curve (1st quadrant) and *M-H* loops recorded for the Co_2FeSn film at 5 K are depicted in Figures 2.28 (a) and (b), respectively. As part of the data analysis, the virgin curve was fitted to the law of approach to magnetic saturation defined by eq. (1.10). M_s (= 1051.9 emu/cc) was obtained from the fitting. Eq. (1.11) is then utilized to obtain the value of K_{eff} (= 6.70×10^6 erg/cc). H_c (= 270 Oe) and M_r (= 1.26 μ_B/f.u.) of the specimen were also obtained from Fig. 2.28 (b) The value of M_s was then converted to the generalized unit of μ_B/f.u. following the procedure outlined below for the composition X_2YZ,

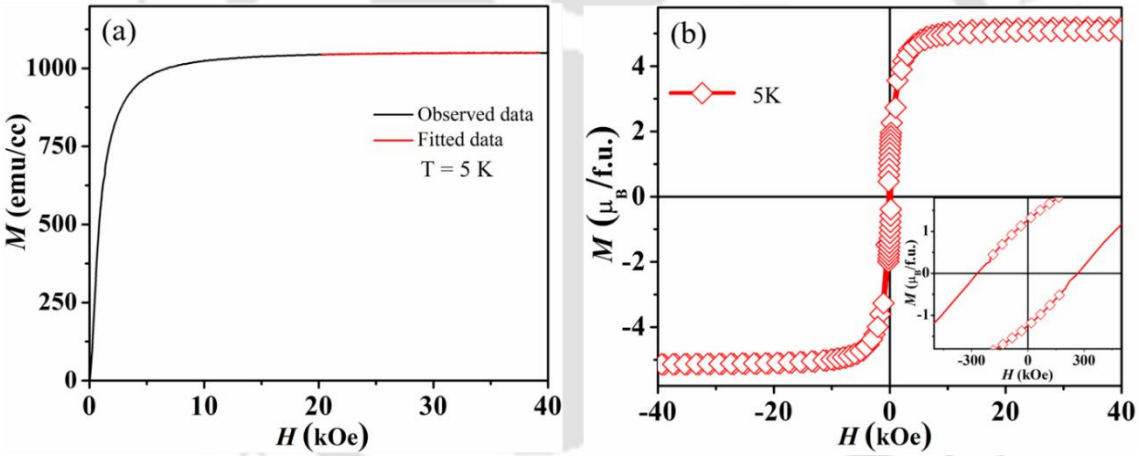

Figure 2.28. (a) Virgin curve fitted to LAS and (b) *M-H* loop of Co_2FeSn film recorded at 5 K.

1 emu = 10^{-3} J/T 2.27

1 μ_B = 9.27402×10^{-24} J/T 2.28

Combining the above two eqs.,

$$1 \text{ emu} = \frac{10^{-3}}{9.27402 \times 10^{-24}}\ \mu_B \quad (2.29)$$

$$\text{emu/g} = \frac{(\text{emu/cc})}{\rho} \quad (2.30)$$

where,

$$\rho = \frac{(Z \times M)}{N_A \times a^3} \quad (2.31)$$

Therefore, M_s in μ_B/f.u. for X_2YZ can be expressed as,

$$M_s\ (\mu_B/\text{f.u.}) = M_s\ (\text{emu/g}) \times \frac{(2\times u_x + 1\times u_y + 1\times u_z)}{N_A} \times \frac{10^{-3}}{9.27402\times 10^{-24}} \qquad 2.32$$

where u_x, u_y, and u_z are atomic masses of X, Y, and Z atoms, respectively, and N_A is Avagadro's number ($N_A = 6.022\times10^{23}$/mole). Using eq. (2.32), the calculated value of M_s for the Co_2FeSn film is 5.18 μ_B/f.u.

Thermomagnetization (*M-T*) measurement is an important characterization technique for magnetic materials, as it provides insights into the second-order ferromagnetic to paramagnetic phase transition temperature, known as Curie temperature. For the $Co_{53.8}Fe_{20.6}Sn_{25.6}$ film, T_C of this sample was determined from the derivative of the magnetization *versus* temperature plot shown in Figure 2.29 (a). To understand the nature of spin systems in these ferromagnetic HA films, the Rhodes-Wohlfarth ratio $\left(\frac{p_c}{p_s}\right)$ of the alloy was estimated from the thermo-magnetization data. As per the proosal, $\left(\frac{p_c}{p_s}\right)$ is supposed to be 1 (unity) for localized-moment ferromagnets, and higher than unity for itinerant ferromagnets [DEKA2015, OTTO1998]. In this ratio, p_c represents the effective paramagnetic moment per atom inferred from the Curie constant, while p_s denotes the magnetic moment at 0 K, obtained by extrapolating the experimentally determined M_s to 0 K [DEKA2015, OTTO1998]. A half-metallic material is expected to exhibit a $\frac{p_c}{p_s}$ value which is significantly less than unity as per the molecular field model proposed by Otto e*t al*. which incorporates both local magnetic moments and spin-polarized itinerant electrons [DEKA2015, OTTO1998]. p_c value can be empirically obtained from the expression,

$$p_c\,(p_c + 2) = \left(\frac{3k_B}{\mu_B^2}\right) C \qquad (2.33)$$

Here, k_B and μ_B denote the Boltzmann constant and the Bohr magneton, respectively, while C denotes the Curie constant. The value of C (for $T > T_C$) can be obtained from the linear fit shown in Figure 2.29 (b), by applying the Curie-Weiss equation [DEKA2015],

$$\chi^{-1} = \left(\frac{T-\theta_p}{C}\right) \qquad (2.34)$$

where θ_p and χ represents the paramagnetic Curie temperature and magnetic susceptibility, respectively. Using eqs. (2.33) and (2.34), Rhodes-Wohlfarth ratio was calculated for $Co_{53.8}Fe_{20.6}Sn_{25.6}$ film to be 0.73 which is less than unity. Hence, the $Co_{53.8}Fe_{20.6}Sn_{25.6}$ alloy film displays the characteristic of a half-metallic ferromagnet. Thus, $\frac{p_c}{p_s}$ ratio serves as a simple and effective means of identifying ferromagnetic half-metals, as it is derived from easily accessible experimental data.

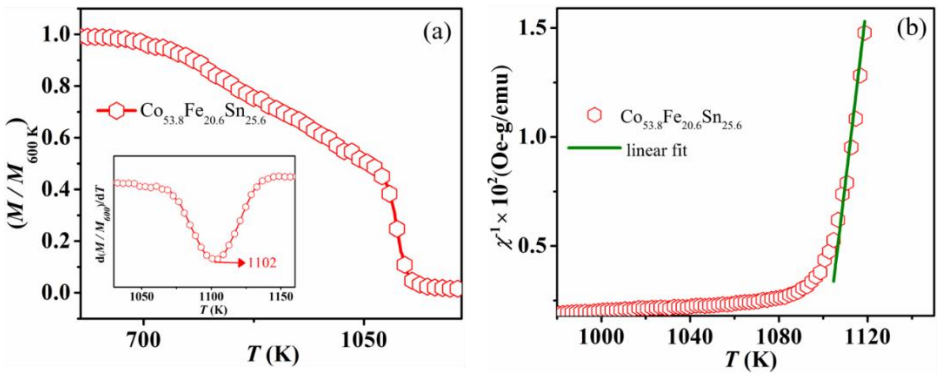

Figure 2.29. (a) *M-T* curve of $Co_{53.8}Fe_{20.6}Sn_{25.6}$film measured under an applied field of 500 Oe. The inset depicts differential magnetization *versus* temperature curve used to locate the T_C. (b) χ^{-1}*versus T* curve corresponding to $Co_{53.8}Fe_{20.6}Sn_{25.6}$ alloy film, fitted to eq. (2.34).

2.2.4. Electrical resistivity measurement

Meaningful insights on the half-metallic nature of prospective spintronic materials can be obtained from temperature-dependent electrical resistivity. In metallic ferromagnetic alloys, the electrical resistivity has a contribution from an intrinsic component (ρ_0) arising from the scattering of conduction electrons by lattice defects and impurities, which remain unaffected by temperature [CHAT2023]. Additional contribution to electrical resistivity from electron-phonon scattering (ρ_{ph}) varies linearly with temperature, especially in the higher temperature range [CHAT2023]. Besides these two contributions, electrical resistivity also exhibits a T^2 dependence due to electron-magnon scattering (ρ_{mag}) [BOMB2013, CHAT2023]. Thus, combining all these contributions, the total electrical resistivity of a ferromagnetic material (ρ_{xx}) can be expressed ,in the form of Matthiessen's rule [CHAT2023] as,

$$\rho_{\mathrm{xx}} = \rho_0 + \rho_{\mathrm{ph}} + \rho_{\mathrm{mag}} \qquad 2.35$$

Incorporating the expressions for the temperature dependence of ρ_{ph} and ρ_{mag}, eq. (2.35) can be rewritten as

$$\rho_{\mathrm{xx}} = \rho_0 + AT + BT^2 \qquad 2.36$$

where *A* and *B* are the coefficients of resistivity from scattering due to phonons and magnons, respectively. Since the contribution to the resistivity from ρ_{ph} is negligible in the low-temperature range, eq. (2.36) can be simplified to the form,

$$\rho_{\mathrm{xx}} = \rho_0 + BT^2 \qquad 2.37$$

Here, magnonic contribution arises from spin-flip scattering in metallic ferromagnetic materials. In the case of half-metallic ferromagnets, the absence of minority (spin-down) states

at E_F results in the suppression of spin-flip scattering. Therefore, the expression of ρ_{xx} turns out to be [BOMB2013, CHAT2023],

$$\rho_{xx} = \rho_0 + BT^2 e^{-\Delta/T} \quad 2.38$$

where Δ is temperature (in K) corresponding to the minimum excitation energy (E_g) required for the majority charge carriers to occupy the empty minority states involving spin-flip. Here, $\Delta = E_g/k_B$, where, k_B represents the Boltzmann constant. In eq. (2.38), the pronounced exponential suppression of electron-magnon scattering due to high Δ is a signature of half-metallicity. However, at high temperatures, the ρ_{ph} term dominates, leading to linear resistivity behaviour described by [BOMB2013, CHAT2023],

$$\rho_{xx} \propto T \quad 2.39$$

The half-metallic nature of the material can be evaluated by fitting eq. (2.38) to the low-temperature region of the temperature-dependent electrical resistivity (ρ_{xx}) data. In the present study, resistivity measurements were carried out using the standard four-probe technique using a PPMS equipped with electrical resistivity measurement option. A film sample with dimensions of 5 mm×4 mm was mounted on a standard four-probe puck. Thin Cu wires were used to establish electrical contact between the film and the gold pads of the puck, with indium serving as the conductive adhesive. The geometry of the linear four-probe resistivity measurement is illustrated in Figure 2.30 (a). A constant current of 5 mA was applied along the length of the film, and measurements were conducted from 5 K to 300 K.

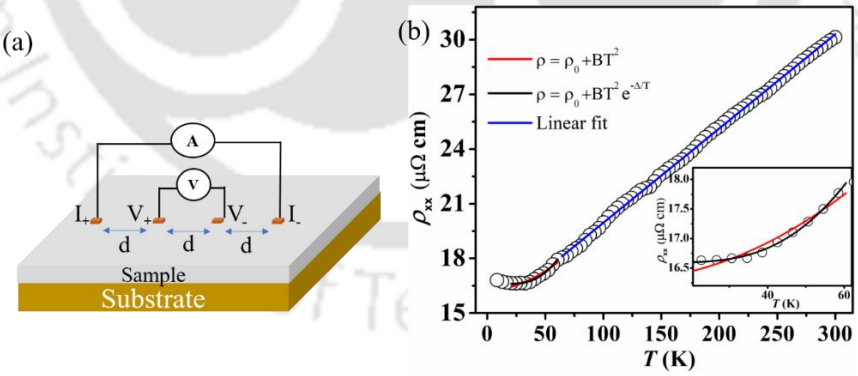

Figure 2.30. (a) Experimental geometry for electrical resistivity measurement. (b) Electrical resistivity *vs* temperature plot of $Co_{53.8}Fe_{20.6}Sn_{25.6}$ alloy, fitted to eqs. (2.37) and (2.38). Inset gives an enlarged view of the low temperature data.

In Figure 2.30 (b), the resistivity *versus* temperature data of $Co_{53.8}Fe_{20.6}Sn_{25.6}$ alloy film is fitted to eqs. (2.37) and (2.38) to evaluate the different contributions to the total electrical resistivity. The red line represents the fit to eq. (2.37) in the low-temperature regime (< 70 K), while the black line shows the fit to the same temperature range using eq. (2.38). It can be seen

that the data in the low-temperature region are better fitted by eq. (2.38), which yields a high value of Δ (> 104 K), a characteristic feature that indicates the half-metallic nature of the film [BOMB2013, CHAT2023].

2.3. Details of *ab initio* calculations

To explore the electronic properties of the HA and provide support to interpret the experimental findings, *ab initio* calculations were conducted using density functional theory (DFT). DFT is a widely used quantum mechanical tool that enables the prediction of various material properties, including the ground-state lattice structure, magnetic moment, DOS, band structure, dielectric constant, entropy, and enthalpy. The theoretical foundation of DFT lies in the Hohenberg-Kohn theorem, which asserts that all ground-state properties of a many-electron system are uniquely determined by its electron density. Accurate results are achieved in DFT by employing Born-Oppenheimer approximation [JOUB1999] and Kohn-Sham formalism [DUDA1998, PERD1996] employing appropriate approximation for the exchange correlation potential. This potential accounts for the Coulomb interaction, which is dominant in elements containing *d* electrons. The simplest approach, the local density approximation (LDA), approximates the exchange-correlation energy density of an inhomogeneous system using the homogeneous electron gas model. Gradient corrections improve the performance of LDA, leading to the generalized gradient approximation (GGA) [DUDA1998].

In this thesis, spin-polarised DFT calculations were carried out using the plane wave-based projector augmented wave (PAW) method, as implemented in the Vienna *Ab initio* Simulation Package (VASP) [DEKA2015, DEKA2016, DUYX2013, MONK1976]. The exchange correlation potential describing electron interactions was treated using the approach proposed by Dudarev *et al.* [DUDA1998]. In this method, electron-electron correlations are accounted by using the effective Hubbard parameter $U_{\text{eff}} = U - J$, where U represents the on-site Coulomb interaction and J is the Hund's rule coupling parameter. To understand the first principle electronic calculation, consider the example of Co_2FeSn HA. To represent the stoichiometric alloy composition, the electronic calculations were carried out using a 16-atom supercell comprising of 8 Co atoms, 4 Fe atoms, and 4 Sn atoms. The lattice constant value of the Co_2FeSn alloy film obtained from the refinement of the concerned experimental XRD pattern was used for the calculation. The self-consistent Kohn-Sham equations were solved with a plane wave cut-off energy of 520 eV and 6×6×6 Monkhorst-Pack *k*-point mesh [MONK1976]. For evaluating the DOS, the tetrahedron method with Blöchl's correction was applied, using a high-density *k*-point mesh of 10×10×10. The typical input files prepared for the VASP calculation are named as INCAR, POSCAR, POTCAR and KPOINT. The INCAR

file specifies the input parameters and conditions for the calculations, such as the plane wave cut-off energy, information about the *U*-parameter, type of smearing, magnetic moment, spin polarization, initial charge density, and other computational settings. A typical INCAR file prepared for Co_2FeSn HA is presented in Figure 2.31. A brief description of the INCAR file parameters are given below:

ISTART

This parameter defines whether to read the WAVECAR file (of the previous step) or not. The WAVECAR file contains information about the initial cut-off energy, initial basis vectors defining the supercell, *etc*. In the present example, " ISTART = 0" is used to start the calculation from the initial step [VASP2025].

ISMEAR

This parameter determines how the partial occupancies f_{nk} are set for each orbital, and this process is referred to as smearing. "ISMEAR = -5" is generally used for DOS calculation, which describes the tetrahedron method with Blöchl corrections [VASP2025].

ICHARG

This parameter provides information about the initial charge density. Among the available values, "ICHARG = 11" is used at the time of DOS calculations to utilize the CHGCAR file obtained from the SCF calculations [VASP25].

SIGMA

This parameter specifies the width of the smearing in eV [VASP25]. A width of "SIGMA = 0.02" has been used in the calculations.

EDIFF

This parameter is employed to define the termination criterion for electronic iterations in eV. Iterative computations were carried out until the energy convergence criterion of $\leq 10^{-5}$ eV (EDIFF = 1E-5) was achieved, to ensure the required precision in energy calculations [VASP25].

ENCUT

This parameter specifies the energy cut-off for the plane-wave basis set in eV [VASP25]. A minimum value of "ENCUT = 520" has been used for the calculations.

ISPIN

This parameter specifies whether the calculation is spin polarized or not. Two possible values, *viz.*, "ISPIN = 1" and "ISPIN = 2" are available. The former shows that non-spin polarized

calculations, whereas the latter shows that spin polarized calculations [VASP25]. Therefore, "ISPIN = 2" has been used throughout the calculations.

PREC

This parameter defines the precision level in the calculation, such as Low | Medium | High | Normal | Single | Accurate. "PREC = Accurate" has been utilized throughout the calculations to yield the best precision [VASP25].

LORBIT

This parameter defines the post-processing step of Kohn-Sham (KS) orbitals to decompose the KS orbitals into local quantum numbers (*l, m*) and obtain local properties, *i.e.*, the onsite charge density or onsite magnetic moments due to spin degrees of freedom. Among various possible values, *viz.*, 0 | 1 | 2 | 5 | 10 | 11 | 12 | 13 | 14, "LORBIT = 11" provides orbital resolved DOS for each element present in the system [VASP2025]. .

MAGMOM

It describes the initial magnetic moment for each element in the form of the number of atoms times the approximate magnetic moment of that element. In case of Co_2FeSn, "MAGMOM = 8*4.0 4*2.0 4*1.0" for 8 Co, 4 Fe, and 4 Sn atoms was used [VASP2025].

IBRION

This parameter defines how the crystal structure changes (updates) during the calculation. During static calculations (DOS, band structure), "IBRION = -1" is used, which means the ionic structure remains fixed during the calculation [VASP2025].

LREAL

It indicates whether the projection operators are evaluated in real space or reciprocal space. In all calculations, the setting "LREAL = Auto" is used, which specifies that the projection is performed in real space with fully automatic optimization of the projection operators [VASP2025].

LWAVE

This parameter specifies whether the wavefunction should be written to the output WAVECAR file. "LWAVE = .FALSE." is used during the relaxation and DOS calculation, while "LWAVE = .TRUE." is set during the SCF step [VASP25].

LCHARG

This parameter determines whether the output CHGCAR file is written or not. "LCHARG = .FALSE." is used during the relaxation step, while "LCHARG = .TRUE." is employed during the SCF calculations to generate the CHGCAR file, which is subsequently used for DOS calculations [VASP2025].

LDAU

This enables the use of the Hubbard parameter (*U*), which accounts for onsite Coulomb repulsion among 3*d* electrons [VASP2025]. The *U* parameter was applied during both SCF and DOS calculations.

LDAUJ

This sets the effective on-site exchange interaction (J) in eV for each element [VASP2025]. J was set to 0.0 eV while performing calculations.

LDAUTYPE

This parameter describes the DFT + *U* approach used in the study. In the present study, "LDAUTYPE = 2", developed by Dudarev *et al.*, is employed [VASP2025].

LDAUL

specifies the *l*-quantum number for which the onsite interaction is added [VASP2025]. In case of Co_2FeSn , "LDAUL = 2 2 0" was utilized for Co, Fe, and Sn elements.

LDAUPRINT

This parameter decides whether to write the onsite occupancy matrix to the OUTCAR file or not. Among possible values, *viz.*, 0 | 1, "LDAUPRINT = 1" was utilized to write the information to OUTCAR file while performing calculations [VASP2025].

LDAUU

This specifies the strength of the onsite Coulomb interactions in eV. In this thesis work *U* parameter was varied between 0.0 eV to 3.0 eV to incorporate onsite Coulomb interactions among 3 *d* electrons.

The above-mentioned parameters can be varied from system to system at different stages according to requirement.

```
SYSTEM = Co2FeSn
ISTART = 0
ISMEAR = -5
ICHARG = 11
SIGMA = 0.02
EDIFF = 0.00001
ENCUT = 520
ISPIN = 2
PREC = .ACCURATE.
LORBIT = 11
MAGMOM = 8*2.0 4*4.0 4*1.0
IBRION = -1
LREAL = Auto
LWAVE = .FALSE.
LCHARG = .FALSE.
LDAU = .TRUE.
LDAUTYPE = 2
LDAUJ = 0 0 0
LDAUL = 2 2 0
LDAUPRINT = 1
LDAUU = 3.0 3.0 0.0
```

Figure 2.31. A typical INCAR file utilized for the DOS calculations of Co_2FeSn HA.

The POSCAR file contains details about the composition and structure of the unit cell, including lattice parameters and atomic positions. The typical example of POSCAR file of Co_2FeSn HA containing 16 atoms (8 Co, 4 Fe, 4 Sn) is shown in Figure 2.32.

The POTCAR file is a combined file that provides the pseudopotential information for each atom in the system. The KPOINTS file defines the *k*-point mesh used for sampling the Brillouin zone. A Γ-centered Monkhorst pack of 10×10×10 *k*-point mesh was used in the Brillouin zone integration required for the electronic part. A typical KPOINT file is given in Figure 2.33.

```
Co2FeSn
1.00000000000000
  5.6722998619000000   0.0000000000000000   0.0000000000000000
  0.0000000000000000   5.6722998619000000   0.0000000000000000
  0.0000000000000000   0.0000000000000000   5.6722998619000000
 Co   Fe   Sn
   8    4    4
Direct
 0.2500000000000000  0.2500000000000000  0.2500000000000000
 0.7500000000000000  0.7500000000000000  0.2500000000000000
 0.7500000000000000  0.2500000000000000  0.7500000000000000
 0.2500000000000000  0.7500000000000000  0.7500000000000000
 0.7500000000000000  0.7500000000000000  0.7500000000000000
 0.2500000000000000  0.2500000000000000  0.7500000000000000
 0.2500000000000000  0.7500000000000000  0.2500000000000000
 0.7500000000000000  0.2500000000000000  0.2500000000000000
 0.5000000000000000  0.5000000000000000  0.5000000000000000
 0.5000000000000000  0.0000000000000000  0.0000000000000000
 0.0000000000000000  0.5000000000000000  0.0000000000000000
 0.0000000000000000  0.0000000000000000  0.5000000000000000
 0.0000000000000000  0.0000000000000000  0.0000000000000000
 0.0000000000000000  0.5000000000000000  0.5000000000000000
 0.5000000000000000  0.0000000000000000  0.5000000000000000
 0.5000000000000000  0.5000000000000000  0.0000000000000000
```

Figure 2.32. A typical POSCAR file utilized during DOS calculation of Co_2FeSn HA.

```
Automatic mesh
0
Gamma
10 10 10
 0  0  0
```

Figure 2.33. A typical KPOINTS file utilized in the DOS calculation of Co_2FeSn HA.

To determine the DOS of the system, a three-step calculation was performed in VASP. In the first step, the ground-state electronic and structural positions are relaxed according to the input structure. In the next step, self-consistent field (SCF) calculations were carried out using the relaxed structure to determine the proper charge distribution of the lattice. Finally, to compute the DOS, a calculation is performed using the charge distribution obtained from the SCF calculation as input, along with the other input files. The total and element-specific

magnetic moment value can be obtained from OSZICAR and OUTCAR files, which are available as OUTPUT files after the completion of the calculation. Typical total DOS and element resolved DOS plots calculated for the Co_2FeSn HA are presented in Figure 2.34 (a) and (b), respectively.

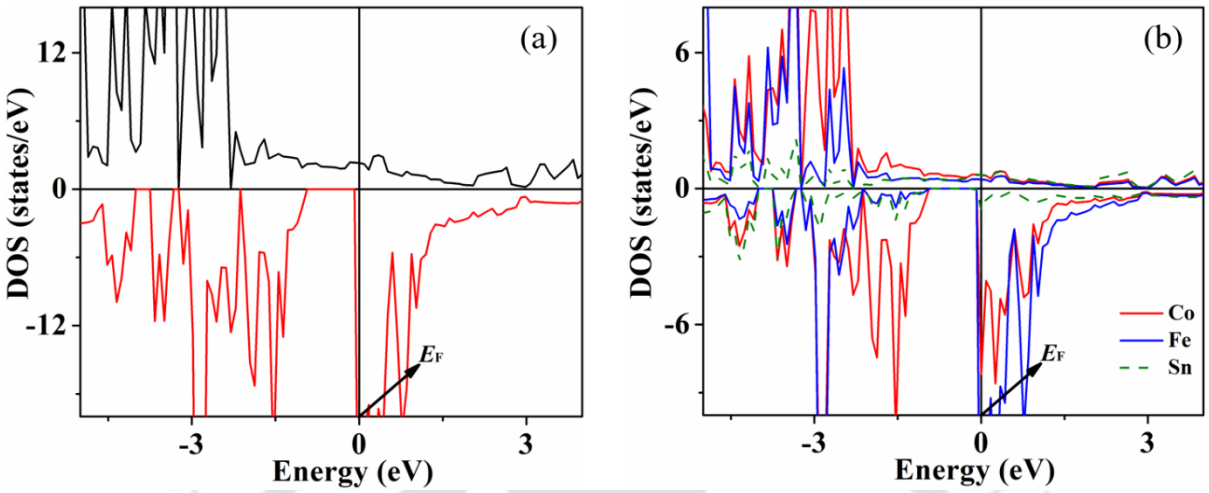

Figure 2.34. (a) Total density of states, and (b) element resolved density of states of Co_2FeSn HA.

More detailed information about the formats of the input and output files, as well as the input parameters, can be found in the VASP manual available on the VASP wiki webpage [VASP2025]. The methodologies outlined above were consistently followed in the investigations carried out in this thesis work.

Chapter 3

Investigations on electrodeposited Co_2FeSn alloy

As highlighted in Chapter 1, Co_2FeSn HA demonstrates outstanding properties, including a high M_s, elevated T_C [GALD2020, PATH2022], and substantial P [GALD2020, HUAN2015]. However, a careful review of the literature reveals that it is extremely challenging to obtain single-phase stoichiometric Co_2FeSn alloy through conventional synthesis methods such as the arc melting process, due to phase segregation of the constituent elements into Co_3Sn_2 and CoFe phases during the cooling process of the molten alloy [ZHAN2005]. Yin *et al.* [YINM2013] have documented the presence of these secondary phases through back-scattered electron microscopy studies. Interestingly, Tanaka *et al.* [TANA2012] achieved a single-phase Co_2FeSn alloy film with $L2_1$-type ordered structure by an atomically controlled alternate deposition method. Their study demonstrated that this technique facilitates the synthesis of such non-equilibrium alloys. However, this technique involves a complex and costly experimental setup with an energy-intensive process [OKE2022]. On the other hand, electrodeposition offers a viable alternative, as it also involves a non-equilibrium process capable of synthesizing non-equilibrium alloys without requiring a complex experimental setup [WATA2015]. Several researchers have attempted to fabricate Co_2FeSn alloy films by electrodeposition, which invariably yielded in Co-Fe-Sn films with either $B2$ or $A2$-type disordered structures [DUAN2013, WATA2015, KARIM2020] as discussed in section 1.2.3 of Chapter 1. Therefore, achieving a single-phase stoichiometric Co_2FeSn films with $L2_1$-type structure with theoretically expected magnetic properties and evaluating their electronic properties are crucial steps towards exploiting the promising characteristics of this alloy. In this chapter, the successful synthesis of $L2_1$-type ordered Co_2FeSn films on polycrystalline copper (Cu) substrate by electrodeposition at room temperature, followed by vacuum heat treatment, is described. This is followed by a discussion on the elemental composition, morphology, crystal structure and magnetic properties of these films. These experimental studies are augmented with theoretical studies performed to estimate the magnetic and electronic properties of this alloy.

3.1. Electrodeposition of Co_2FeSn alloy film

Co_2FeSn HA film was deposited on high-purity (99.99%) polycrystalline Cu substrate by potentiostatic electrodeposition process already explained in Chapter 2. Optimized amounts of metal sulphates, *viz.*, $CoSO_4.7H_2O$ (3.8518 g), 1.7040 g of $FeSO_4.7H_2O$, and 0.1785 g of $SnSO_4$ were used as precursors in 125 ml of ascorbic acid stabilized DI water. 2.3190 g boric acid, 2.0580 g of NaCl, 15 g of sodium gluconate, and 0.0025 g of peptone were used as additives. The film deposition was carried out using potentiostatic mode with an optimized V_{dep} of -4.0 V [PATH2022] for t_{dep} of 300 s. The details of the deposition process including optimization of V_{dep} and reaction mechanism involved in the formation of stoichiometric Co_2FeSn alloy film, are mentioned in section 2.1.1.1 of this thesis. The as-deposited film of 1420±10 nm thickness was cleaned with acetone, air dried, and vacuum flame sealed in a fused silica ampoule at a pressure of ~10^{-3} Pa. The sealed ampoule containing film was heat treated at an optimized temperature of 550 °C for 1 hour to induce proper crystallization of the alloy film.

3.2. Compositional analysis of Co_2FeSn alloy film

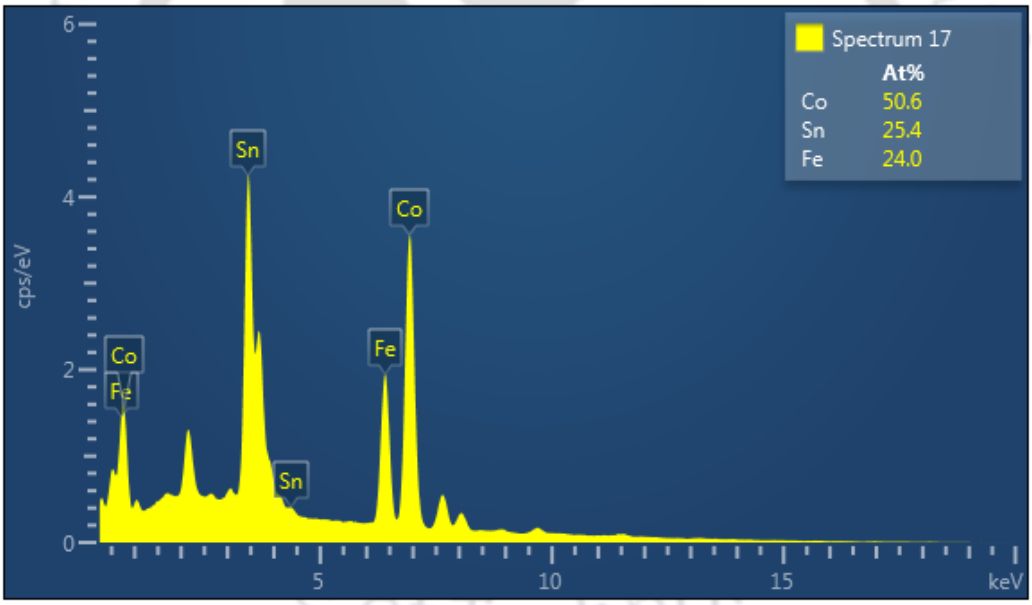

Figure 3.01. Reduced EDS data of Co_2FeSn alloy film after subtraction of Cu, C and Au peaks.

Figure 3.01 displays a typical raw EDS spectrum of the heat treated Co_2FeSn alloy film. The detected peaks in the spectrum other than those of the constituent elements (Co, Fe, and Sn) originate from the Cu substrate, carbon (C) tape used to mount the sample on the electrode, and the conductive gold (Au) coating applied on the film surface to prevent charging effects. After excluding the Cu, C, and Au contributions from the raw data, the actual elemental composition of the specimen was determined as illustrated in Figure 3.01. From the figure, it

is clear that Co, Fe, and Sn are the only constituents present, and their concentrations (in at.%) are 50.6, 24.0, and 25.4, respectively. The overall composition of the films was evaluated by taking the average of 10 such individual spectral scans from various parts of each sample. The average elemental composition of the deposited film, determined by EDS analysis, is $Co_{49.8\pm1.2}Fe_{23.3\pm1.6}Sn_{26.9\pm1.5}$, which is very close to the stoichiometric $Co_{50.0}Fe_{25.0}Sn_{25.0}$ composition.

3.3. Structure and morphology of Co_2FeSn alloy film

Room temperature XRD patterns of as-deposited and heat treated Co_2FeSn films are shown in Figure 3.02 (a) along with the simulated pattern. The simulated pattern was generated using the $L2_1$-type unit cell of Co_2FeSn alloy by CaRIne crystallography 3.1 software. Rietveld refined XRD pattern of the heat treated Co_2FeSn film using the $L2_1$-type unit cell is shown in Figure 3.02 (b). The goodness of fit parameter (χ^2) obtained from the least squares fitting is 2.08. The as-deposited film shows a weak reflection from the (220) plane, which appears as a shoulder to the strong (111) primary reflection from the Cu substrate at a 2θ value of 44°. Appearance of the (220) reflection confirms the crystallization of the Heusler phase in the as-deposited state, but its weak intensity compared to Cu peaks implies poor crystallization of the HA phase. However, upon heat treatment, reflections from (220), (400), and (422) HA phase appear in the XRD pattern. The absence of the characteristic superlattice (111) and (200) reflections in the XRD pattern of the heat-treated film can be attributed to the low intensity of (111) and (200) reflections, even with the fully ordered structure, as indicated by their very low intensities in the simulated pattern. However, the SAED pattern of the heat treated alloy film exhibited both (111) and (200) reflections as depicted in Figure 3.03 (a). Figure 3.03 (b and c) displays the HRTEM micrographs showcasing the lattice fringes of (111) and (200) superlattice planes, which establish the formation of $L2_1$-type full HA structure in the heat treated Co_2FeSn film. Insets in the figures show the lattice fringes with better clarity in the ifFT images.

The lattice constant (a) of the heat treated Co_2FeSn film was obtained from Rietveld refinement of the XRD data and was found to be 5.6993 Å. Theoretically estimated a values reported by different authors lies in the range of 4.2400 Å to 6.0130 Å [FALE2017, HUAN2015, MATS2017] and those reported from experimental studies vary from 5.7000 Å to 5.9000 Å [GALD2020, KARI2020, KARI2021, TANA2012] for Co_2FeSn nanoparticle, nanowire, and electrodeposited films. D_v of the heat treated Co_2FeSn film was estimated using the Schërrer's equation (eq. (2.15)), yielding a value of 21±1 nm.

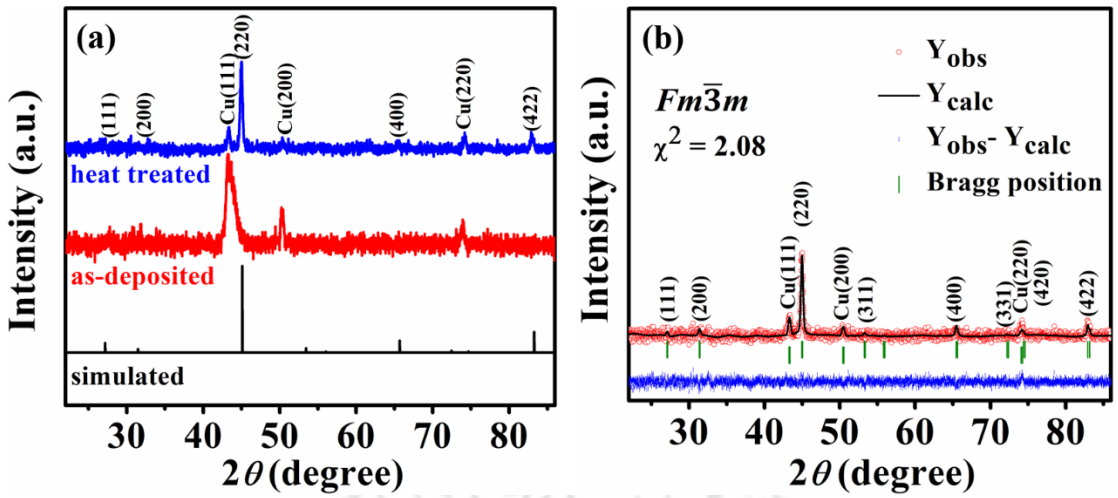

Figure 3.02. (a) XRD patterns of simulated, as-deposited and heat treated Co_2FeSn films. (b) Rietveld refined XRD pattern of heat treated Co_2FeSn film using space group 225 [$Fm\bar{3}m$].

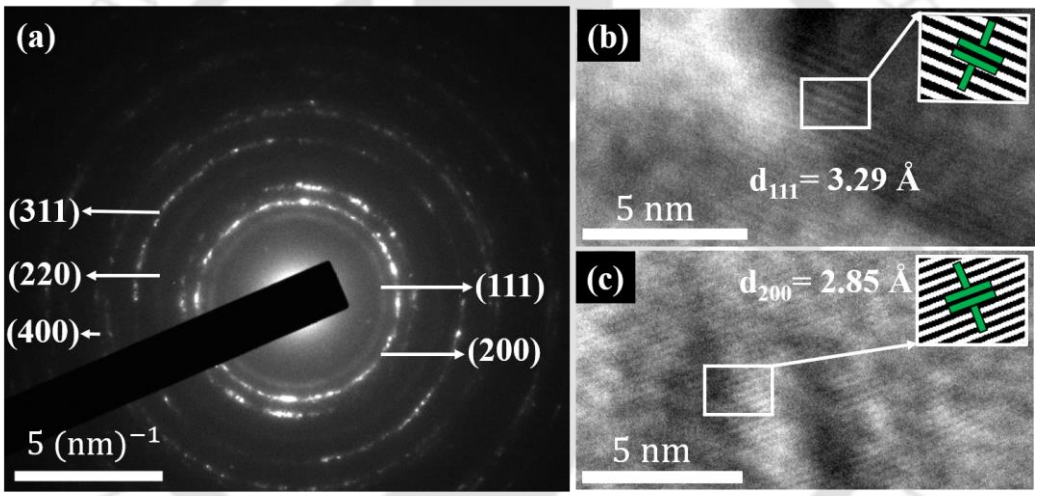

Figure 3.03. (a) SAED pattern of heat treated Co_2FeSn film. HRTEM images of superlattice planes (b) (111), and (c) (200), with corresponding ifFT images displayed as insets**.**

Figure 3.04 (a, b) portrays the FESEM micrographs of as-deposited and heat-treated Co_2FeSn films, respectively. Both the as-deposited and heat treated films show granular film morphology. Duan *et al.* [DUAN2013] reported similar morphology for their electrodeposited Co_2FeSn film with near stoichiometric composition. The grains in the heat treated film are compact and larger than the as-deposited film due to thermally driven grain growth during the heat treatment process, which promotes the formation of larger and more stable grains. Figure 3.04 (c) shows the grain size distribution of heat treated Co_2FeSn film, which ranges from 14 to 30 nm with a mean grain size of 23±1 nm and a dispersion (FWHM) of 8 nm.

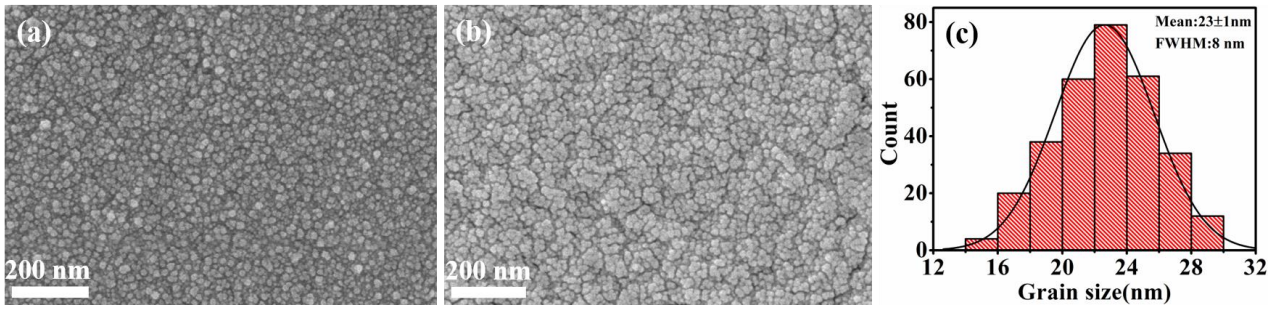

Figure 3.04. FESEM micrographs showing granular morphology of (a) as-deposited and (b) heat treated Co_2FeSn films. (c) Grain size distribution of heat treated Co_2FeSn film.

3.4. Magnetic properties of Co_2FeSn alloy film

Figure 3.05 (a and b) show the variation of in-plane magnetization with applied magnetic field of as-deposited and heat treated films recorded at 5 K and 300 K. Insets in Figure 3.05 (a and b) provide an enlarged view of the data close to the origin. The as-deposited film exhibits *A*2-type fully disordered structure, resulting in lower M_s and H_c due to the absence of long-range crystalline ordering. Heat treatment promotes the growth of larger nanocrystalline grains, facilitating the development of long range ferromagnetic interaction and the formation of $L2_1$-type fully ordered HA structure in the heat treated film, resulting in higher magnetic moment [MODA2017, PATH2022]. The M_s and H_c values of the as-deposited film at 5 K (300 K) are 3.00±0.02 μ_B/f.u. and 78 Oe (2.77±0.02 μ_B/f.u. and 27 Oe), and the corresponding values of the heat treated film are 5.18±0.04 μ_B/f.u. and 270 Oe (4.97±0.04 μ_B/f.u. and 249 Oe), respectively. Li *et al*. [LITA2013] reported M_s of 4.31 μ_B/f.u. at room temperature for *B*2-type Co_2FeSn nanoparticles. Li *et al*. [LIPE2015] in their study on diffusion-assisted Co_2FeSn nanoparticles, reported *A*2-type fully disordered structure with M_s of 5.2 μ_B/f.u. (at 5 K) and 4.9 μ_B/f.u. (at 300 K). Duan *et al*. [DUAN2013] reported M_s of 4.5 μ_B/f.u and H_c of 70 Oe (at 5 K) and 32 Oe at room temperature for Co_2FeSn film electrodeposited on polycrystalline Cu substrate. The electrodeposited Co_2FeSn film studied in this work exhibits higher M_s than that of the Co_2FeSn nanoparticles reported by Li *et al*. [LITA2013] and the electrodeposited films by Duan *et al*. [DUAN2013], and is comparable to that of Co_2FeSn nanoparticles prepared by Li *et al*. [LIPE2015] using diffusion assisted method. It is to be noted that the 5-12 nm Co_2FeSn nanoparticles synthesized by Li *et al*. [LIPE2015] by complex chemical route exhibited a fully disordered Heusler structure. The comparable M_s value reported for their structurally disordered nanoparticles may be attributed to compositional variations in their samples relative to the ordered Co_2FeSn films being examined in the present study. This speculation is tenable since disordered HA invariably exhibit lower M_s than their ordered counterparts with the same

composition. The films studied in this study exhibit soft ferromagnetic nature in agreement with the previous reports [KARI2020, LITA2013, LIPE2015, LUHO2018, WATA2015].

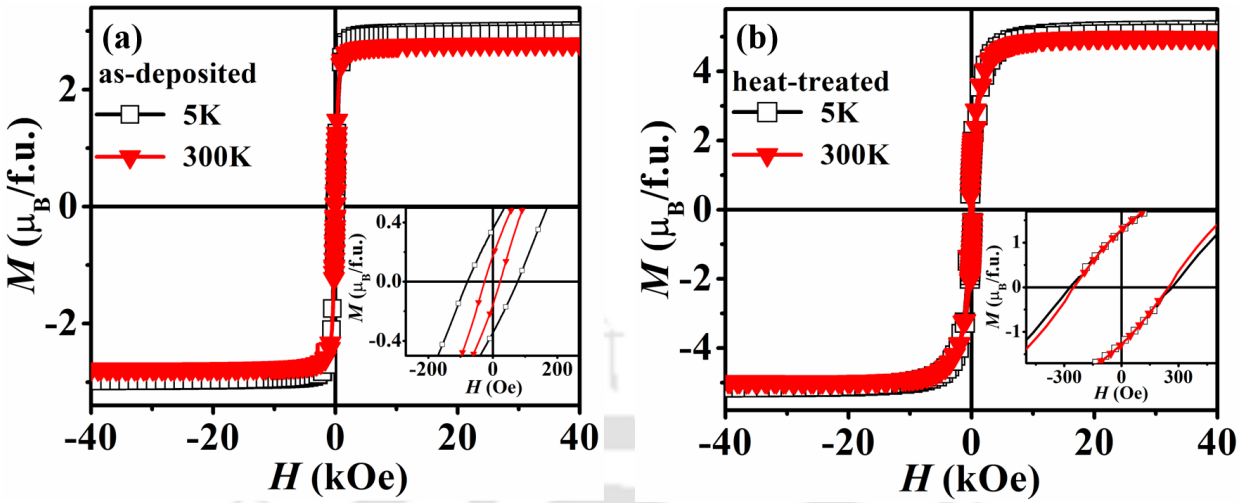

Figure 3.05. *M-H* curves recorded at 5 K and 300 K for (a) as-deposited and (b) heat treated Co_2FeSn films. Insets show an expanded view of the data near the origin.

The K_{eff} of the Co_2FeSn film was estimated from the initial magnetization (*M-H*) curve using the law of approach to magnetic saturation (eq. (1.09)) [ANDR1997, FAHN1978, JINZ1998]. K_{eff} of as-deposited Co_2FeSn film was found to be 3.18×10^6 erg/cc at 5 K and 1.92×10^6 erg/cc at 300 K, and the corresponding values for the heat-treated film were 6.70×10^6 erg/cc and 4.94×10^6 erg/cc, respectively. K_{eff} of electrodeposited Co_2FeSn is higher than that of sputtered Ni-Mn-Sn (7.3×10^5 erg/cc) [MODA2017] and Ni-Mn-Ga (4.2×10^5 erg/cc) films [GOLU2009]. The higher K_{eff} observed in the present study is primarily due to its higher M_s [DEKA2016a] as compared to those of the reported Ni-Mn-Sn and Ni-Mn-Ga films.

Thermomagnetization curve of heat-treated Co_2FeSn film, recorded under an applied field of 500 Oe (shown in Figure 3.06), reveals a high T_C of 1123 K. Although Galdun *et al.* [GALD2020] performed *M-T* measurements at a very high field of 3.7 kOe on Co_2FeSn nanowires, they merely speculated the T_C to be higher than 1000 K. The high T_C of Co_2FeSn films could be attributed to better atomic ordering due to the ordered $L2_1$-type structure as compared to their disordered *B*2-type structure. Marchenkov *et al.* [MARC2018] reported the T_C of bulk Co_2FeSn and Co_2FeSi alloy as 1000 K and 1100 K, respectively. Kobayashi *et al.* [KOBA2004] prepared $Co_2Cr_{1-x}Fe_xAl$ alloy in bulk form and found that T_C of the alloys increased from 850 K to 1170 K as x is increased from 0.5 to 1.0. The experimentally determined T_C for electrodeposited Co_2FeSn film is comparable to the previously reported values of bulk Co_2FeZ (Z = Al, Ga, Si) [MARC2018, KOBA2004, HIRO2006] system and

higher than the value reported for any form of Co_2FeSn. To explore the half-metallic character and to estimate the magnetic moment of Co_2FeSn alloy, *ab initio* calculations were performed, which are discussed in the next section of this chapter.

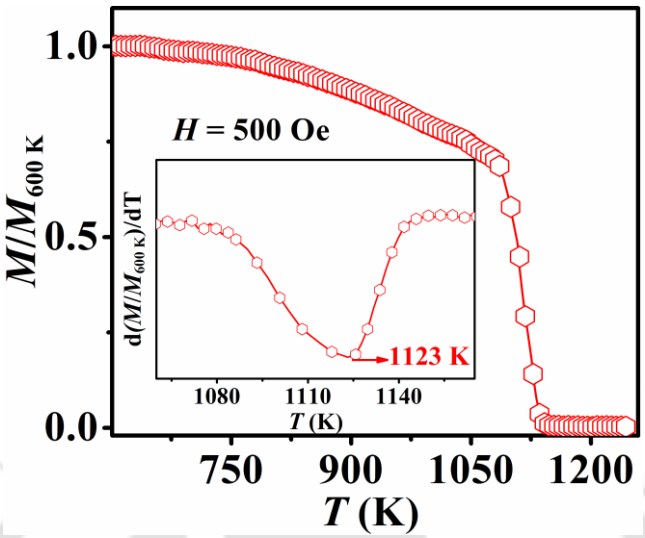

Figure 3.06. *M-T* curve of heat treated Co_2FeSn film recorded under an applied field of 500 Oe. Inset depicts the differential of magnetization curve plotted to locate the T_C of the alloy film.

3.5. Density of electronic states and magnetic moment of Co_2FeSn alloy

After successful synthesis and characterization of the heat treated Co_2FeSn alloy film, the electronic structure of the alloy was theoretically explored. A Co_2FeSn supercell consisting of 16 atoms (8 Co, 4 Fe, and 4 Sn) was used in the calculations. Ideally, the atoms in the unit cell occupy the designated Wyckoff position of the full Heusler structure, *i.e.* Sn (0, 0, 0) 4*a*, Fe (½, ½, ½) 4*b*, Co (¼, ¼, ¼) 4*c* and Co (¾, ¾, ¾) 4*d*, respectively [MATS2017]. The lattice constant obtained from Rietveld refined XRD data was used in the calculations. The detailed methodology followed in the *ab initio* calculations are discussed in section 2.3 of Chapter 2. Özdogan *et al*. [OZDO2007] performed *ab initio* calculations on the Co_2FeSn alloy using the GGA scheme. Their result did not display any gap in the minority spin channel at E_F in the computed DOS, leading to the conclusion that Co_2FeSn is non-half-metallic. However, the experimental study by Galdun *et al.* [GALD2020] on the Co_2FeSn nanowire, using point contact Andreev reflection measurements, reported a *P* value of ~85%. Based on this investigation, they claimed that the high *P* is preserved in low-dimensional forms of Co_2FeSn alloy. It is worth noting that the *ab initio* studies performed by Özdogan *et al*. [OZDO2007] did not consider Coulomb interactions in their calculations, despite the fact that these interactions are significant in highly correlated electron systems involving transition metals

like Fe and Co. To understand the nature of the minority DOS in the presence of electron correlations, *ab initio* calculations were carried out using the GGA+*U* approach, following the procedure outlined in section 2.3 of Chapter 2. The total DOS and element-resolved DOS of the Co_2FeSn alloy are shown in Figure 3.07 and Figure 3.08, respectively. To investigate the influence of *U*, the DOS calculations were performed by varying the *U* value from 0.0 to 2.0 eV in steps of 0.5 eV, as depicted in Figure 3.07 (a-e) and Figure 3.08 (a-e). In the figures, the absolute energy difference between the gap edge and E_F is denoted by δ_{EU}. At U = 0.0 eV, the presence of minority states at E_F indicates a non-half-metallic nature of Co_2FeSn HA. However, an energy gap was observed at 0.36 eV below E_F in the valence band. Interestingly, as the *U* value increased from 0.0 to 1.5 eV, the gap gradually shifted toward E_F. At U = 1.5 eV, the energy gap approached its closest approach to E_F, *i.e.* 0.05 eV below E_F. With further increase to U = 2.0 eV, the gap moved away from E_F, which is portrayed in Figure 3.07 (e). The energy gap in the minority band of Co_2YZ HAs arises from the bonding and antibonding characteristics of the second nearest neighbour Co-Co 3*d* interactions [GALA2002]. Miura *et al.* [MIUR2006] suggested that in Co_2FeZ alloys, there is a high possibility of Co-Fe type disorder. This disorder is attributed to the valence electron charge around the Fe atom in the ordered $L2_1$-type structure. Such antisite disorder introduces additional nonbonding states, which disrupt the half-metallic electronic band structure [MIUR2006].

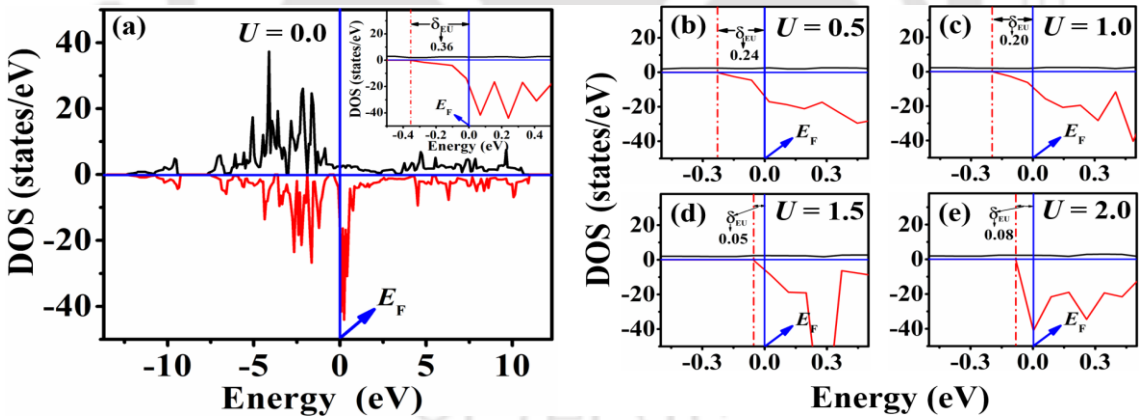

Figure 3.07. TDOS near E_F of Co_2FeSn alloy calculated using $L2_1$-type unit cell with (a) U = 0.0, (b) U = 0.5, (c) U = 1.0, (d) U = 1.5, and (e) U = 2.0 eV. In all the figures, E_F is taken to be at 0.0 eV, and δ_{EU} is the absolute energy difference between the gap edge and E_F.

The presence of minority states at E_F in Co_2FeSn alloy can be understood from the element-resolved DOS (EDOS) distribution as shown in Figure 3.08 (a-e). Özdogan *et al.* [OZDO2007], in their investigation of Co_2CrZ (Z = Al, Sn), reported that the additional electron present in the case of Sn-based compounds (compared to Al based ones) occupies the

majority spin states. This leads to enhanced exchange splitting between occupied majority states and unoccupied minority states, resulting in a wider energy gap for Sn based compounds relative to Al based counterparts. Furthermore, they noted that in Co_2FeZ compounds containing Fe as the Y element, the extra valence electron (relative to Cr) causes an overlap of Co bonding and antibonding minority *d* states, thereby destroying the energy gap associated with the Co atoms. Additionally, the unoccupied Fe states shift toward the minority spin band for all *U* values. These features are evident from the element-resolved DOS plots in Figure 3.08 (a-e). As illustrated in both total DOS and element resolved DOS (Figure 3.07 and Figure 3.08), the presence of Fe contributes to the reduced value of the majority DOS at E_F [OZDO2007]. Hence, by varying the onsite Coulomb interaction from 0.0 to 2.0 eV, the energy gap in the minority spin channel can be brought as close as 0.05 eV below E_F, but not exactly at E_F. This indicates that the simultaneous presence of Fe and Sn is responsible for disrupting the half-metallicity in the Co_2FeSn HA [PATH2022].

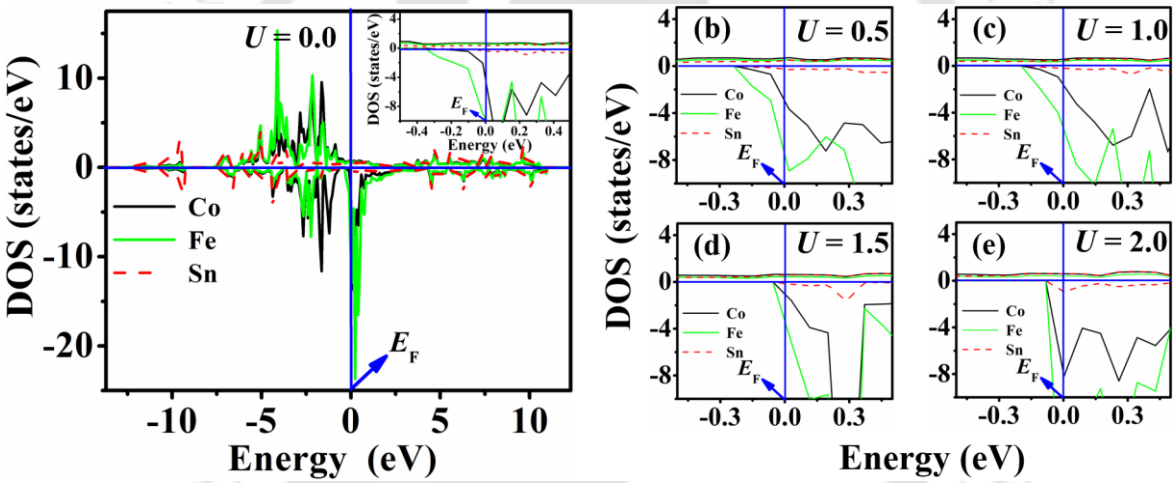

Figure 3.08. Element resolved DOS near E_F for Co_2FeSn alloy calculated using $L2_1$-type unit cell with (a) U = 0.0, (b) U = 0.5, (c) U = 1.0, (d) U = 1.5, and (e) U = 2.0 eV. In all the figures, 0.0 eV refers to the location of E_F.

To understand and investigate possible ways to induce half-metallicity in Co_2FeSn alloy, the partial DOS (PDOS) of the magnetic elements Fe and Co were calculated as a function of *U* near E_F, as shown in Figure 3.09 (a-j). For all *U* values, the valence band in the minority spin channel is predominantly occupied by Co-t_{2g} orbitals, while the conduction band is primarily contributed by Fe-e_g orbitals. Due to the dominance of Co-e_g and Fe-e_g orbitals near E_F, the conduction states start to originate slightly below E_F, leading to the occurrence of minority states at E_F. Similar behaviour has been observed in the minority spin channel of Co_2FeSi HA

by Khosravizadeh *et al.*[KHOS2009]. Thus, the non-half-metallic nature of Co_2FeSn arises from the partial occupation of minority *d*-states at E_F.

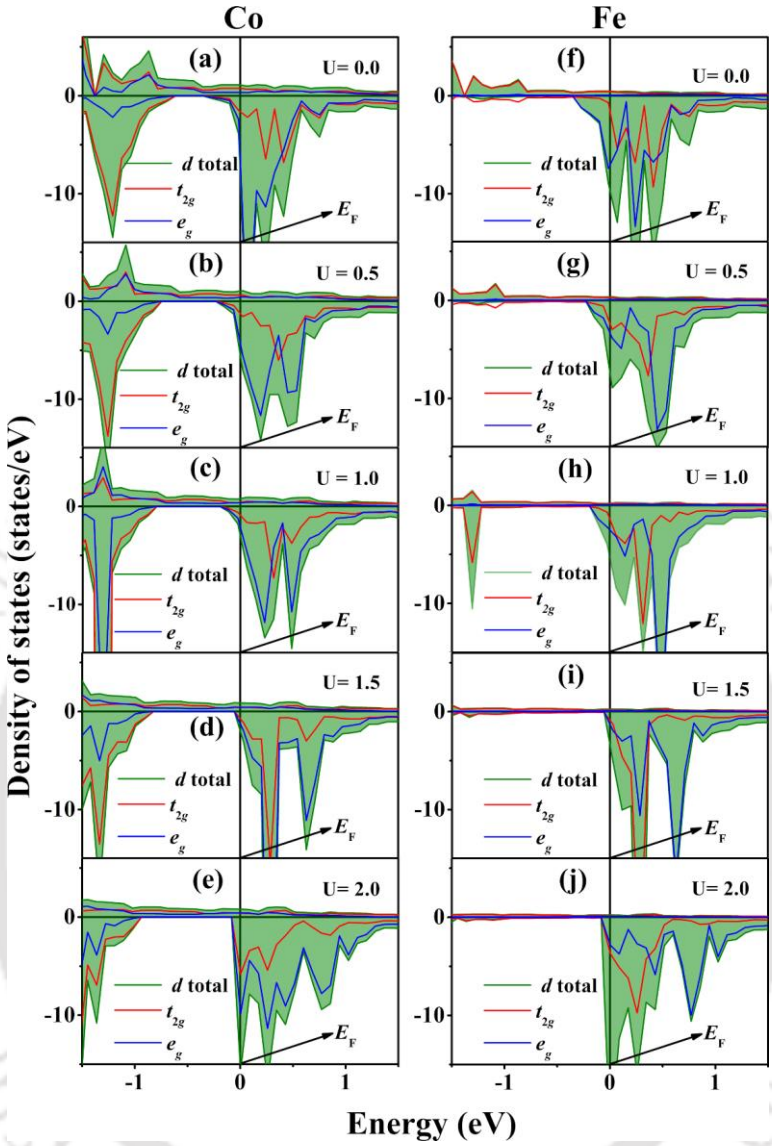

Figure 3.09. Projected partial DOS of *d*-orbital with doubly degenerate e_g and triply degenerate t_{2g} states of Co with (a) U = 0.0, (b) U = 0.5, (c) U = 1.0, (d) U = 1.5, (e) U = 2.0 eV, and Fe with (f) U = 0.0, (g) U = 0.5, (h) U = 1.0, (i) U = 1.5, (j) U = 2.0 eV.

Upon incorporating the electron correlation parameter U in the calculations, the Co-e_g and Fe-e_g states become progressively less occupied, causing the minority bandgap to shift closer to E_F. As shown in Figure 3.09 (d) and Figure 3.09 (i), for U = 1.5 eV, the gap is positioned very close to E_F, and the e_g states of Co and Fe are nearly unoccupied. However, increasing U to 2.0 eV results in the shifting of the minority gap away from E_F, thereby bringing in significant contributions from Co and Fe t_{2g} and e_g states. A detailed discussion on the hybridization scheme responsible for the formation of t_{2g} and e_g orbitals is given in section

1.1.3.2 of Chapter 1. From the above discussion, it becomes evident that reducing the extra valence electrons in Fe by substituting it with a lower valent element can effectively suppress the minority states at E_F in Co_2FeSn alloy. *Ab initio* study by Özdoğan *et al*. [OZDO2007] on the $Co_2Cr_{1-x}Fe_xSn$ offers a valuable insight into this aspect. Their calculations demonstrate that when $x = 0.4$ in $Co_2Cr_{1-x}Fe_xSn$ alloys, the extra minority states originating from Co and Fe (t_{2g} and e_g states) at E_F could be reduced. thereby facilitating the formation of a full minority band gap in the minority spin channel. It is important to note that these theoretical investigations are strictly applicable to bulk systems with fully ordered $L2_1$-type structure and were obtained at $T = 0$ K. If the assertion made by Galdun *et al*. [GALD2020] that half-metallicity is preserved in low-dimensional forms of Co_2FeSn such as nanowires (1-dimensional nanomaterial) is valid, then spin polarization measurements on Co_2FeSn films would clarify whether the same is also preserved in nanogranular films.

Table 3.01. Calculated total and atomic spin magnetic moment of Co_2FeSn HA for different U values.

U (eV)	M_t (μ_B/f.u.)	Atomic spin moment (μ_B/f.u.)			
		Co (I) (¼, ¼, ¼)	Co (II) (¾, ¾, ¾)	Fe (½, ½, ½)	Sn (0, 0, 0)
0.0	5.03	1.23	1.23	2.63	-0.06
0.5	5.30	1.28	1.28	2.81	-0.07
1.0	5.52	1.34	1.34	2.91	-0.07
1.5	5.72	1.39	1.39	3.02	-0.08
2.0	5.88	1.43	1.43	3.10	-0.08

The theoretically calculated magnetic moment values for various U parameters are presented in Table 3.01. Both Co atoms, *i.e.* Co (I) located at Wycoff position 4*c* (¼, ¼, ¼), and Co (II), at 4*d* (¾, ¾, ¾), exhibit identical spin magnetic moment across all U values. This invariance arises from the fact that, although both Co atoms occupy different sublattices, they are situated in equivalent local environments, each surrounded by 4 Fe and 4 Sn atoms. For non-zero U values, the Coulomb interaction parameter plays an important role, particularly because both Fe and Sn atoms are surrounded by eight Co atoms as their nearest neighbours. In the case of Fe, an increase in the U parameter leads to a rise in its individual M_t, as illustrated in Table 3.01. M_t of Sn remains very small and is antiparallel to those of Co and Fe. This weak moment is induced by the surrounding magnetic Fe and Co atoms. Consequently, as the spin

moment of Fe increases with *U*, a corresponding change is also observed in the induced M_t of Sn. Nepal *et al.* [NEPA2020] made similar observations in Co_2ZAl (Z = Sc, Ti, V, Cr, Mn, and Fe) alloys, where a change in M_t of the Z element either through the application of *U* parameter or by substituting different Z atoms, led to changes in the weak magnetic moment of the *sp* element. The theoretically calculated value of M_t for Co_2FeSn by various authors ranges from 5.52 - 5.70 μ_B/f.u. [GILL2009, MATS2017, NOKY2018, OZDO2007], which aligns well with the magnetic moment calculated in this work for the case with U = 1.5 eV, for which the minority gap lies very close to E_F. M_t value reported by Huang *et al.* [HUAN2015] is 5.994 μ_B/f.u., which differs from the current value due to a larger lattice parameter (6.0130 Å) employed in their calculations, which is different from our experimentally calculated lattice parameter of 5.6993 Å.

3.6. Summary

The combined experimental and theoretical investigations on the structural and magnetic properties of electrodeposited Co_2FeSn HA films yield the following key insights:

- A highly ordered $L2_1$-type structured Co_2FeSn HA film with granular morphology has been synthesized on a low-cost polycrystalline Cu substrate by the electrodeposition route.
- The electrodeposited Co_2FeSn films exhibit soft ferromagnetic behaviour with high M_s (5.18 μ_B/f.u. at 5 K), elevated T_C (1123 K), and a high K_{eff} (6.70×10^6 erg/cc at 5 K). M_s observed for the heat treated film is the highest reported to date (in film form) and is closest to the theoretical value for this alloy.
- DOS calculations performed using the GGA+*U* approach offer deeper insights into the minority gap near E_F and a way to effectively tune its position.
- The combination of high M_s, elevated T_C, large K_{eff}, and the presence of a minority gap near E_F makes the electrodeposited Co_2FeSn HA film a promising candidate for various nanomagnetic applications.

Apart from demonstrating a simple, economical, and non-equilibrium electrodeposition route for the synthesis of stoichiometric Co_2FeSn alloy films with high crystalline ordering, this study highlights the superior magnetic properties of the prepared films.

Chapter 4

Film thickness-dependent properties of electrodeposited Co_2FeSn alloy films

The successful synthesis and in-depth analysis of structural, morphological, magnetic, and electronic properties of electrodeposited Co_2FeSn films with a thickness of 1.42 μm have already been presented in Chapter 3. These films exhibited an ordered $L2_1$-type structure with optimal magnetic properties. However, the downscaling of electrodeposited films from micrometer to nanometer scale, required for nanomagnetic applications, remains a challenge [PATH2023]. Unlike the magnetron sputtering techniques, the dependence of the deposition rate of individual elements in nanometric multi-element alloy films deposition is not well understood and adapted to yield consistent chemical stoichiometry in electrodepostion. This is primarily due to limited information available in the literature on the influence of V_{dep} and t_{dep} on the mobility of individual ions in a multi-element alloy film [DUAN2013, PATH2023]. This chapter outlines a procedure for scaling down the thickness of electrodeposited near-stoichiometric Co_2FeSn films to the sub-micrometre regime while preserving high crystalline order. The corresponding variation in morphological and magnetic properties of the films as a function of their film thickness are also reported in this chapter.

4.1. Electrodeposition of Co_2FeSn alloy films with different thicknesses

Co_2FeSn HA films of different thickness with near stoichiometric composition were electrodeposited on high-purity (99.99%) 0.2 mm thick polycrystalline Cu substrate by the potentiostatic electrodeposition process already explained in Chapter 2. Prior to electrodeposition, an appropriate amount of metal sulphates, *i.e.*, $CoSO_4.7H_2O$ (3.8518 g), 1.7040 g of $FeSO_4.7H_2O$, and 0.1785 g of $SnSO_4$, were used as precursors in 125 ml of DI water. 2.3190 g boric acid, 2.0580 g of NaCl, 15 g of sodium gluconate, 0.5 g ascorbic acid and 0.0025 g of peptone were used as additives. The film deposition was carried out using potentiostatic mode with the optimized V_{dep} of -4.0 V [PATH2022, PATH2023]. The details of the deposition process involved in the formation of Co-Fe-Sn alloy films are mentioned in Chapter 2 of the thesis. A stoichiometric film with a thickness of 320 nm, designated as P1, was obtained through electrodeposition following this process for t_{dep} of 75 s. Likewise, a film

with a thickness of 780 nm (designated as P2) was achieved through a t_{dep} of 150 s. Extending the deposition time to 300 s resulted in a film with a thickness of 1400 nm (designated as P3). The concentration of the electrolytic bath and all deposition parameters except t_{dep} remained constant throughout the deposition of all three films. Figure 4.01 illustrates the FESEM image showcasing the thicknesses of (a) P1, (b) P2, and (c) P3 films, where F represents the film thickness and Cu denotes the copper substrate. The as-deposited films of 320, 780, and 1400 nm thickness were cleaned with acetone, air dried, and vacuum flame sealed in fused silica ampoules at a pressure of ~10^{-3} Pa. The sealed ampoules containing films were heat treated at an optimized temperature of 550 ℃ for 1 h to induce proper crystallization of the alloy films.

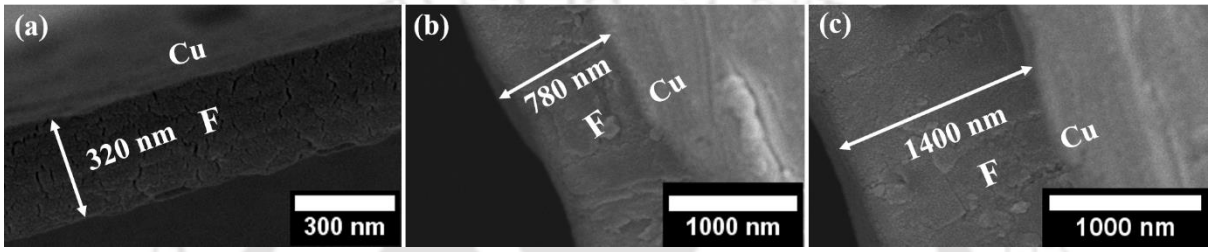

Figure 4.01. Cross-sectional FESEM images showing the thickness of (a) P1, (b) P2, and (c) P3 film, where F represents the film and Cu denotes the copper substrate.

4.2. Compositional analysis of Co_2FeSn alloy films with different thicknesses

The overall composition (Co:Fe:Sn) in at. % was evaluated from an average of at least 10 minimum individual EDS spectral scans from various regions of P1, P2, and P3 films. The average value of composition obtained for P1 film was Co:50.3±1.3, Fe:24.8±1.4, Sn:24.9±1.4. Similarly, film P2 exhibits an overall composition of Co:49.8±1.4, Fe:26.2±1.3, Sn:24.0±1.3. The corresponding values obtained for the P3 film are Co:49.8±1.5, Fe:23.2±1.3, Sn:27.0±1.4, respectively. It can be seen that films P1, P2, and P3 have an overall composition which is in close proximity to the stoichiometric composition of Co:50.0, Fe:25.0, Sn:25.0. The variation of the film thicknesses has been achieved by merely varying t_{dep} in the range of 75 s to 300 s. Attempts to electrodeposit for lower t_{dep} resulted in the film with chemical composition deviating too much from the stoichiometric composition. This shows that there is a window of t_{dep} over which films with stoichiometric composition could be electrodeposited under the said deposition conditions and electrolyte concentration. Figure 4.02 displays a typical raw EDS spectrum of the heat treated P1 film. As explained earlier, the spectrum contains peaks from the Cu substrate C tape and Au top coating apart from those of the constituent elements (Co, Fe, and Sn). After excluding the Cu, C, and Au contributions from the raw data, the actual elemental composition of the alloy film was determined as illustrated in Figure 4.02.

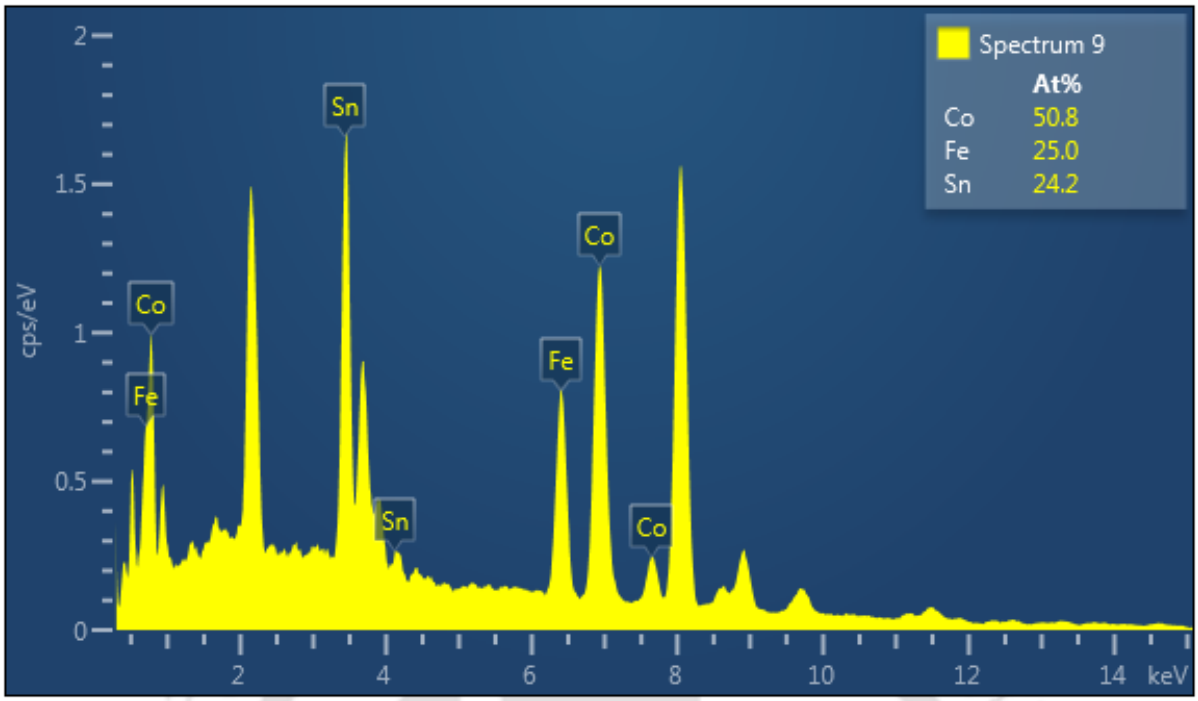

Figure 4.02. Typical reduced EDS data of P1 film after subtraction of Cu, C and Au peaks.

4.3. Structure and morphology of Co_2FeSn alloy films with different thicknesses

XRD patterns of heat treated P1, P2, and P3 films are shown in Figure 4.03 (a) along with the simulated XRD pattern generated by CaRIne crystallography 3.1 software using $L2_1$-type unit cell. The presence of intense (220), (400), and (422) reflections validates the formation of the HA structure. As seen from the simulated XRD pattern, the intensity of (111) and (200) superlattice reflections are intrinsically very weak and hence are not observed in the experimental XRD patterns [PATH2022, PATH2023]. However, SAED patterns of the heat treated P1 film reveal the presence of (111) and (200) superlattice reflections, which are characteristic of the highly ordered $L2_1$-type structure as depicted in Figure 4.04 (a). High-resolution transmission electron microscope images of lattice fringes of the two superlattice planes, along with their ifFT, are presented in Figure. 4.04 (b) and (c). Rietveld refinement of the XRD patterns for heat treated P1, P2, and P3 films was performed using the $L2_1$-type unit cell and the results are depicted in Figure 4.03 (b, c, and d). The goodness of fit parameter (χ^2) was found to be as low as 2.30, 2.79, and 2.31 for P1, P2, and P3 films, respectively, with lattice constants of 5.6902 Å, 5.6891 Å, and 5.6892 Å. The experimentally observed values of the lattice constant of P1, P2, and P3 films are very close to previously reported values on Co_2FeSn nanoparticles [LIPE2015], nanowires [GALD2020], and electrodeposited films [DUAN2013, PATH2022], which are in the range of 5.6993 Å to 5.9000 Å.

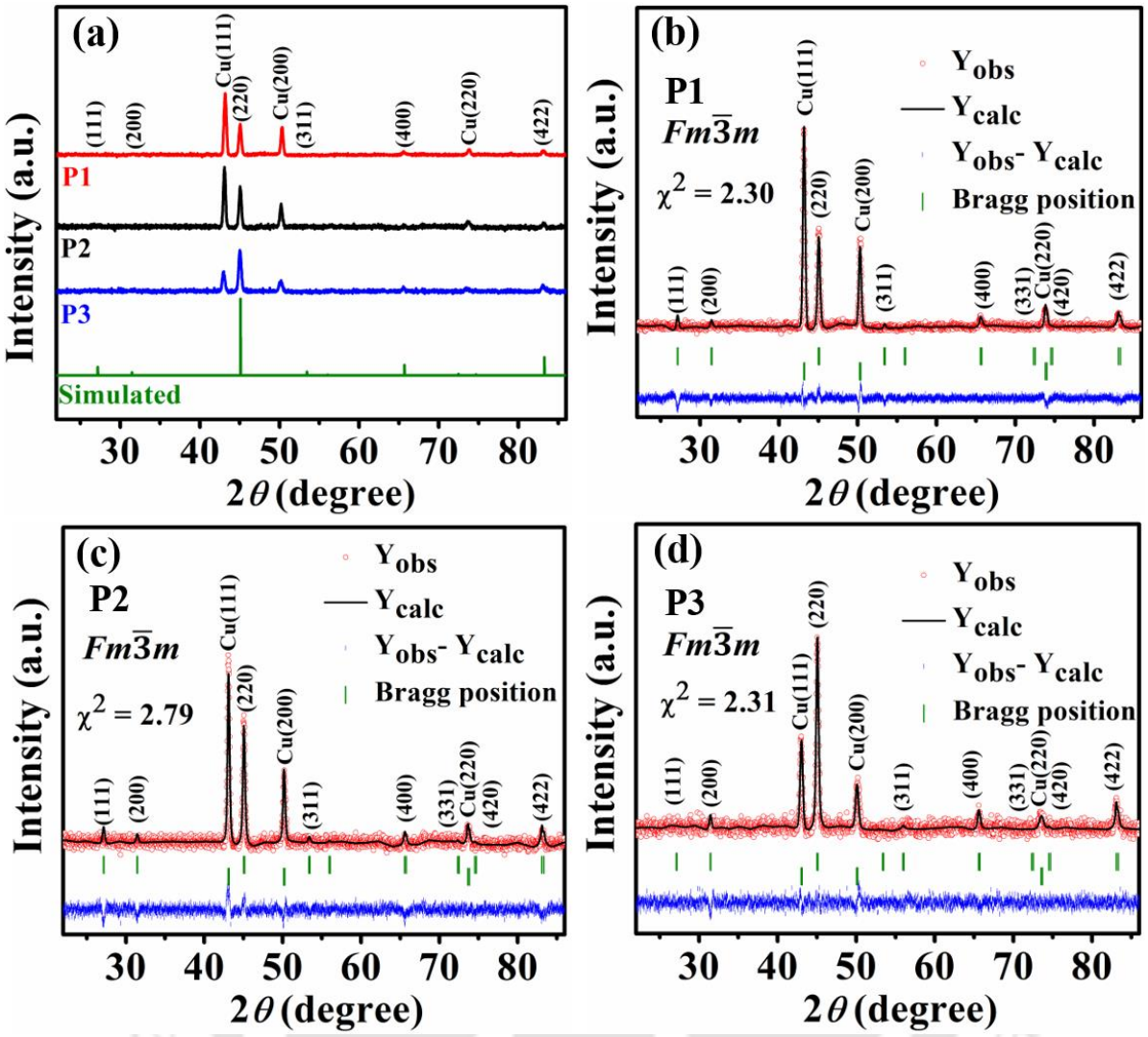

Figure 4.03. (a) Simulated and experimental XRD patterns of heat treated P1, P2, and P3 films. (b-d) Rietveld refined XRD patterns of P1, P2, and P3 films using space group 225 [$Fm\bar{3}m$].

D_v of the heat treated P1, P2, and P3 films were estimated using Schërrer's equation (eq. (2.15)) [CULL2014], yielding values of 20±1 nm, 21±1 nm, and 21±1 nm, respectively. The consistent D_V values indicate that the deposition and heat-treatment conditions are similar for the three films.

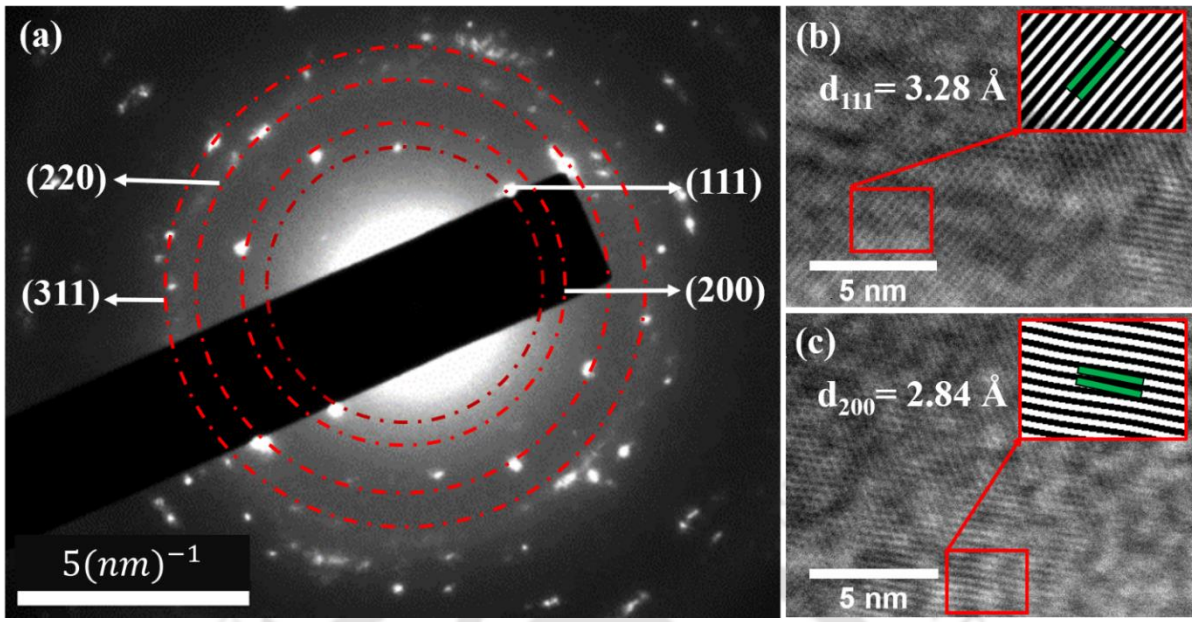

Figure 4.04. (a) Typical SAED pattern of heat treated P1 film and HRTEM images of superlattice planes (b) (111), and (c) (200) with the corresponding ifFT image as an inset.

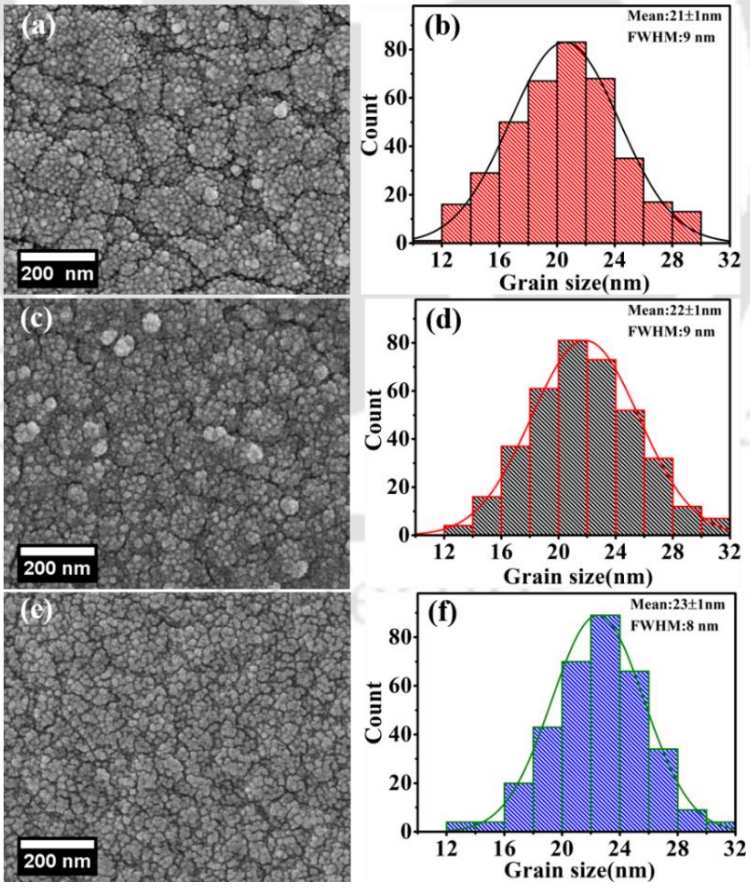

Figure 4.05. FESEM micrographs showing the morphology of heat treated (a) P1, (c) P2, and (e) P3 films. (b, d, and f) grain size distributions for P1, P2, and P3 films, respectively.

Figure 4.05 (a), (c), and (e) portray the FESEM micrographs of heat treated P1, P2, and P3 films. All three electrodeposited films exhibit a granular film morphology, consistent with the surface features observed by Duan *et al.* [DUAN2013] in their study on galvanostatically electrodeposited Co_2FeSn alloy films. They reported a grain size distribution ranging from 10 to 40 nm and explained that the electrodeposited film consists of aggregates which contain many fine grains. Watanabe *et al.* [WATA2015], while investigating electrodeposited Co-Fe-Sn films, found that films with stoichiometric composition were smooth but contained large cracks. They also claimed that the film morphologies are highly affected by V_{dep} and current density applied during the deposition process [WATA2015]. Figure 4.05 (b), (d), and (f) present the grain size distributions for P1, P2, and P3 films, respectively. These grain sizes range from 12 to 32 nm, with mean values of 21±1 nm, 22±1 nm, and 23±1 nm and corresponding FWHM of 9 nm, 9 nm, and 8 nm.

4.4. Magnetic properties of Co_2FeSn alloy films with different thicknesses

Figure 4.06 (a and b) show the variation of in-plane magnetization of P1, P2, and P3 films as a function of applied magnetic field at 5 K and 300 K. Insets of Figure 4.06 (a and b) provide an enlarged view of the data close to the origin. The M_s (H_c) values of P1, P2, and P3 films measured at 5 K are 5.08±0.04 μ_B/f.u. (244 Oe) , 5.14±0.04 μ_B/f.u. (201 Oe), and 5.18±0.04 μ_B/f.u. (270 Oe), respectively. The corresponding values at 300 K are 4.79±0.04 μ_B/f.u. (201 Oe) , 4.81±0.04 μ_B/f.u. (154 Oe), and 4.97±0.04 μ_B/f.u. (249 Oe), respectively. As the thickness of the film is increased, a small increment in magnetic moment is observed, which is a consequence of the improved crystallinity in the films with increasing thickness[PATH2023]. The total magnetic moment estimated from the magnetization *versus* applied magnetic field curves of P1, P2, and P3 films are higher than the previously reported value by Duan *et al.* [DUAN2013] (4.5 μ_B/f.u. at 5 K) for electrodeposited Co_2FeSn film, and Li *et al.* [LITA2013] (4.31 μ_B/f.u. at 300 K) for Co_2FeSn nanoparticles. Better results obtained in the present study are attributed to the higher crystalline order achieved in our heat treated films as compared to the previous studies [PATH2023]. P1, P2, and P3 films show soft ferromagnetic behaviour as observed by other researchers as well [DUAN2013, LITA2013]. The obtained M_s values of the three films are close to the theoretical spin magnetic moment of Co_2FeSn alloy estimated using *ab initio* calculations, which varies between 5.53 μ_B/f.u. and 5.72 μ_B/f.u. as reported by different authors [HUAN2015, MATS2017, PATH2022].

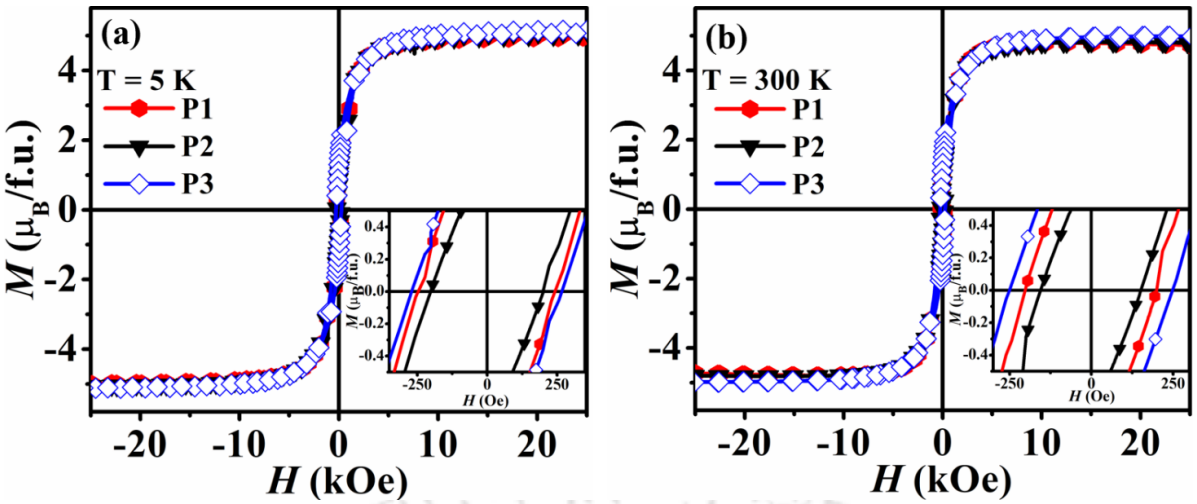

Figure 4.06. Magnetization *versus* applied magnetic field curves of P1, P2, and P3 films recorded at (a) 5 K, and (b) 300 K. Insets depict a magnified view of curves near the origin.

The K_{eff} of P1, P2, and P3 film was estimated from the initial magnetization curve using the law of approach to magnetic saturation (eq. (1.09)) [ANDR1997, FAHN1978, JINZ1998]. K_{eff} values obtained for P1, P2, and P3 films at 5 K are 5.7×10^6 erg/cm^3, 5.7×10^6 erg/cm^3, and 6.4×10^6 erg/cm^3. The corresponding values at 300 K are 3.4×10^6 erg/cm^3, 3.9×10^6 erg/cm^3, and 5.3×10^6 erg/cm^3, respectively. The high K_{eff} values obtained for these electrodeposited films are comparable to those reported for other Co-based HAs nanoparticles by Nehla *et al.* [NEHA2019] (7.6 - 9.0×10^6 erg/cm^3), Srivastava *et al.* [SRIV2023a] (4.87×10^6 erg/cm^3), and for bulk samples by Deka *et al.* [DEKA2014] (6.54 - 11.17×10^6 erg/cm^3). Furthermore, the observed K_{eff} values of P1, P2, and P3 films are slightly higher than the value of 5.1×10^5 erg/cm^3 reported for a sputtered Ni-Mn-Ga film of 3 μm thickness [GOUL2009]. Karim *et al.* [KARI2020] in their investigation on Co_2FeSn alloy films, reported an anisotropy constant of 1.5×10^6 erg/cm^3 and highlighted that the magnetic anisotropies in ordered cubic HAs arise from the coexistence of strong intrinsic magnetocrystalline and uniaxial anisotropies. It is also noteworthy that the K_{eff} values of P1, P2, and P3 samples exhibit only a small decrement when raised to room temperature, a trend also observed by Srivastava *et al.* in the case of Fe_2CoGa nanoparticles [SRIV2022].

Thermomagnetization curves of the heat treated P1, P2, and P3 films, recorded under an applied field of 500 Oe, are displayed in Figure 4.07. The measurements performed in the temperature range of 355 K to 1200 K reveal a second-order phase transition from the ferromagnetic to the isotropic paramagnetic phase at elevated temperatures. The inset in Figure 4.06 depicts the temperature derivative of magnetization (dM/dT), which was employed to

determine the ferromagnetic-paramagnetic phase transition temperature (or Curie temperature). The extremum in the dM/dT curves corresponds to the T_C values of 995 K, 1005 K, and 1123 K for P1, P2, and P3 films, respectively. The observed increment in T_C with film thickness could be due to the slight variation in film composition among the three samples, as well as the improved crystalline order in the thicker films. Such variation in T_C with film thickness is consistent with reports on sputtered Ni-Mn-Sn films [MODA2018b].

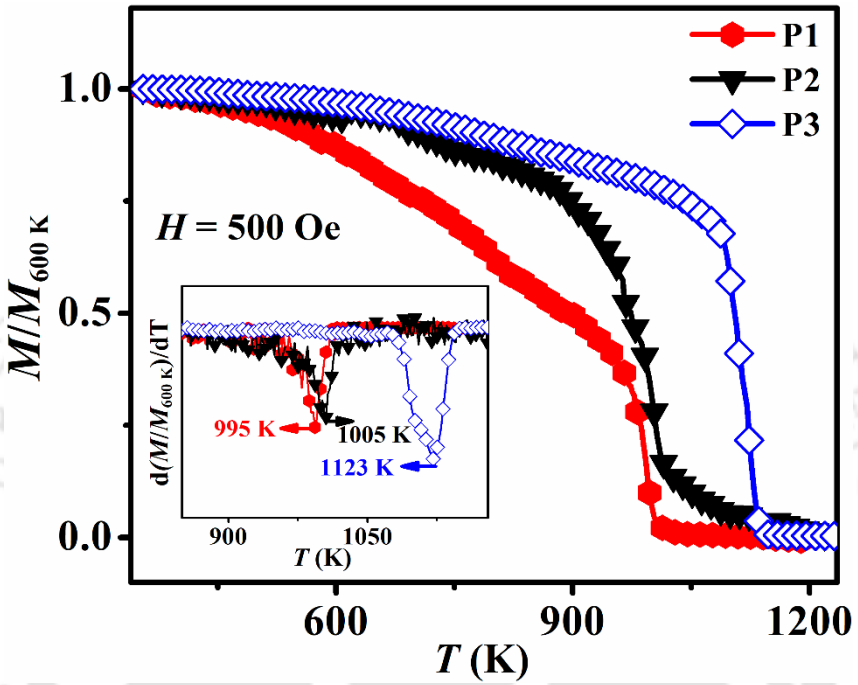

Figure 4.07. Magnetization *versus* temperature curves of P1, P2, and P3 films recorded with an applied field of 500 Oe. The inset depicts the differential of magnetization *versus* temperature curves used to locate T_C.

4.5. Summary

The results obtained in experimental investigations on the thickness-dependent structural, morphological, and magnetic properties of electrodeposited Co_2FeSn HA films are summarized below:

- High-quality electrodeposited Co_2FeSn films of thicknesses ranging from 1400 nm to 320 nm, exhibiting an ordered $L2_1$-type structure and granular film morphology, have been successfully prepared for the first time on polycrystalline Cu substrates by merely varying electrodeposition time (t_{dep}) while keeping all other deposition parameters and electrolyte concentration unchanged.
- All three electrodeposited Co_2FeSn films exhibit soft ferromagnetic behaviour characterized by high M_s ranging from 5.08 to 5.18 μ_B/f.u. at 5 K, elevated T_C between 995 K and 1123 K, and high K_{eff} in the range of 5.7 to 6.4 × 10^6 erg/cc at 5 K.

- The combination of high M_s, elevated T_C, and large K_{eff} in the Co_2FeSn alloy films, along with a small decrement in magnetic properties when scaling down the thickness from micrometer to the nanometer range, makes it a promising material for various micro and nano magnetic applications.

In addition to demonstrating a simple, cost-effective, and non-equilibrium electrodeposition route for synthesizing highly crystalline Co_2FeSn alloy films of varying thicknesses, this study also highlights the potential of electrodeposition for fabricating films with nanometric dimensions.

Chapter 5

Tuning of magnetic properties and half-metallicity in electrodeposited Co-Fe-Sn films by varying composition

As discussed in Chapter 3, Co_2FeSn exhibits high M_s, elevated T_C and substantial P [GALD2020, MARC2018, PATH2022]. However, *ab initio* calculations have indicated that the bandgap in the minority spin channel of Co_2FeSn is 0.05 eV below E_F, making it a non half-metal [PATH2022]. The finite DOS at E_F in the minority spin channel is attributed to the additional valence electron of Fe, which causes the overlapping of the bonding and antibonding hybridized spin-down states of Co at E_F [OZDO2007, PATH2023]. Considering the promising properties of Co_2FeSn HA, inducing half-metallicity in this HA could pave the way to its exciting spintronic device applications. In this context, the key question is whether the finite DOS in the minority spin band at E_F in Co_2FeSn HA can be removed by suppressing the contribution of the additional valence electron of Fe by resorting to off-stoichiometric Co-Fe-Sn alloy compositions. To explore this bandgap engineering route toward achieving half-metallicity, off-stoichiometric Co-Fe-Sn alloy films were synthesized by the electrodeposition route. Their structural, morphological, magnetic, electronic, and half-metallic properties are discussed here.

5.1. Electrodeposition of Co-Fe-Sn alloy films

A set of three Co-Fe-Sn films of different off-stoichiometric compositions were electrodeposited on a cleaned high purity Cu substrate having a thickness of 0.2 mm in potentiostatic mode. Three different electrolytic solutions were prepared in 250 ml of ascorbic acid stabilized DI water for depositing the films, designated as S1, S2, and S3. For the film S1, an electrolytic solution was prepared by taking 7.0878 g of $CoSO_4 \cdot 7H_2O$, 0.1785 g of $SnSO_4$ and 1.7040 g of $FeSO_4 \cdot 7H_2O$ as metal precursors. In addition to this, 30 g of sodium gluconate, 0.0050 g of peptone, 4.1160 g of NaCl , and 4.6380 g of boric acid were utilized as additives. For S2, the electrolytic solution was made of 7.5451 g of $CoSO_4 \cdot 7H_2O$, 1.7538 g $FeSO_4 \cdot 7H_2O$,

and 0.1824 g of $SnSO_4$, while keeping all additives the same as in the case of S1. In the case of sample S3, the electrolyte consisted of 7.7741 g of $CoSO_4 \cdot 7H_2O$, 1.7538 g of $FeSO_4 \cdot 7H_2O$ and 0.1798 g $SnSO_4$ with the same amount of additives as in S1 (and S2). All the electrodepositions were carried out under the pre-optimized V_{dep} of -4.0 V for t_{dep} of 300 s [PATH2022]. The details of the deposition process involved in the formation of Co-Fe-Sn alloy films are mentioned in Chapter 2 of this thesis. The thickness of all films was determined to be 1400 nm using cross-sectional FESEM measurement. The poorly crystallized as-deposited films were gently cleaned with acetone, air dried, and flame sealed under vacuum in fused silica ampoules at a pressure of ~10^{-3} Pa. The sealed ampoules containing films were heat treated at an optimized temperature of 550 ℃ for 1 hour to induce proper crystallization of the alloy films.

5.2. Compositional analysis of Co-Fe-Sn alloy films

The overall elemental composition of the processed films was determined from EDS studies by taking the average of a minimum of 10 individual spectral scans from various regions of S1, S2, and S3 films. The average value of the composition obtained for the S1, S2 and S3 films are $Co_{48.5\pm1.0}Fe_{22.8\pm1.2}Sn_{28.7\pm1.2}$, $Co_{51.7\pm1.1}Fe_{21.6\pm1.3}Sn_{26.7\pm1.2}$, and $Co_{53.8\pm1.0}Fe_{20.6\pm1.4}Sn_{25.6\pm1.2}$, respectively. The variation in film composition was achieved by varying only the metal precursor amount in the electrolyte solution, keeping all other parameters the same. Figure 5.01 (a, b, and c) displays a typical EDS spectrum of the heat treated S1, S2, and S3 films after eliminating the contributions from the Cu substrate, C tape and the conductive Au coating.

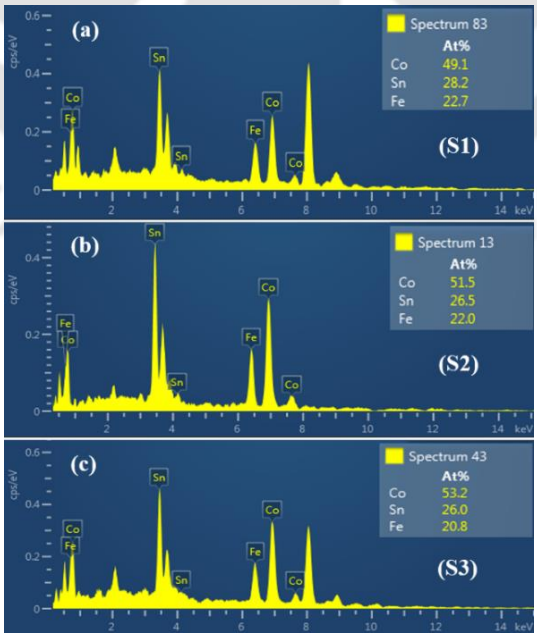

Figure 5.01. Typical EDS spectrum of (a) S1, (b) S2, and (c) S3 alloy films after subtracting the contributions from the copper substrate, conducting carbon tape, and gold coating.

5.3. Structural and morphological analysis of Co-Fe-Sn alloy films

Figure 5.02 (a) represents the XRD patterns of S1, S2, and S3 films along with the simulated pattern generated using $L2_1$-type unit cell. Intense reflections from (220), (400), and (422) planes confirm the formation of the HA structure. Since the intensity of superlattice reflections (111) and (200) are very weak, even in the XRD pattern simulated for S3, these reflections are not discernible in the experimentally obtained XRD patterns. On the other hand, SAED patterns show the existence of superlattice reflections (111) and (200), indicating the presence of a highly ordered $L2_1$-type structure as depicted in Figure 5.03 (a). Figure 5.03 (b and c) present the HRTEM lattice fringe images of (111) and (200) superlattice planes with corresponding ifFT images as insets.

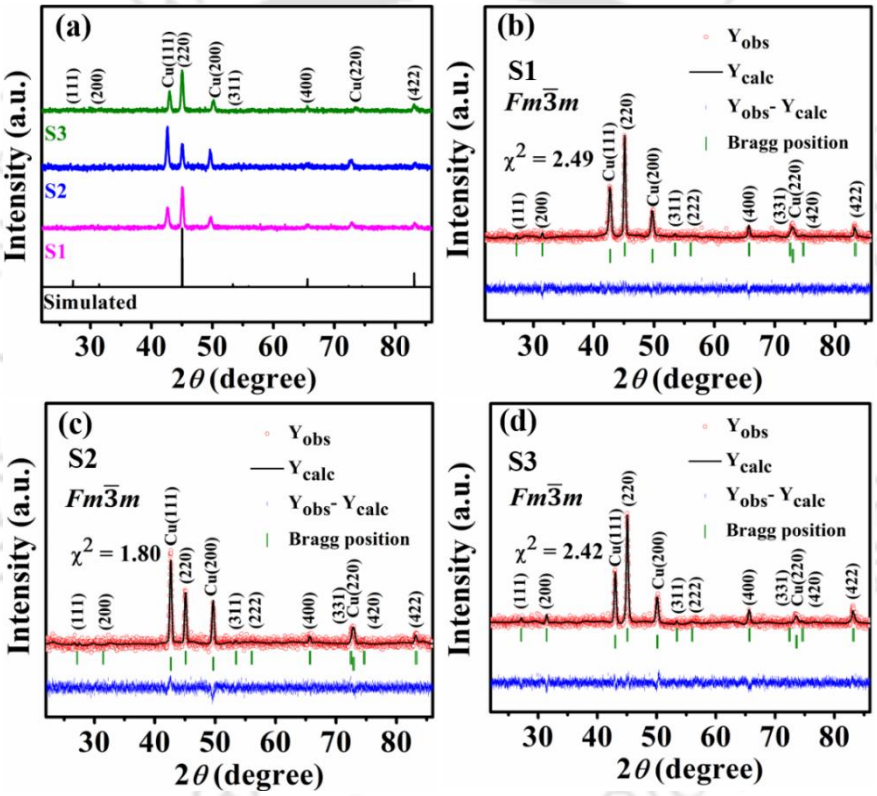

Figure 5.02. (a) XRD patterns of S1, S2 and S3 films along with the simulated one for S3. (b - d) Rietveld refined XRD patterns of S1, S2 and S3 films employing 225 [$Fm\bar{3}m$] space group.

The XRD patterns of S1, S2, and S3 films were refined using the Rietveld method employing an $L2_1$-type unit cell, and the corresponding results are portrayed in Figure 5.02 (b, c, and d). The χ^2 values, which reflect the quality of the refinement, are 2.49 for the S1, 1.80 for the S2, and 2.42 for the S3 films. The corresponding lattice parameters of the three films are 5.6940 Å, 5.6870 Å, and 5.6828 Å, respectively. The observed values of the lattice parameter of S1,

S2, and S3 are in close agreement with the previously reported values on Co-Fe-Sn HA [KARI2020, PATH2022, PATH2023]. D_V of S1, S2, and S3 films estimated using Schërrer's equation (eq. (2.15)) [CULL2014] was found to be 22±1 nm, 23±1 nm, and 23±1 nm, respectively.

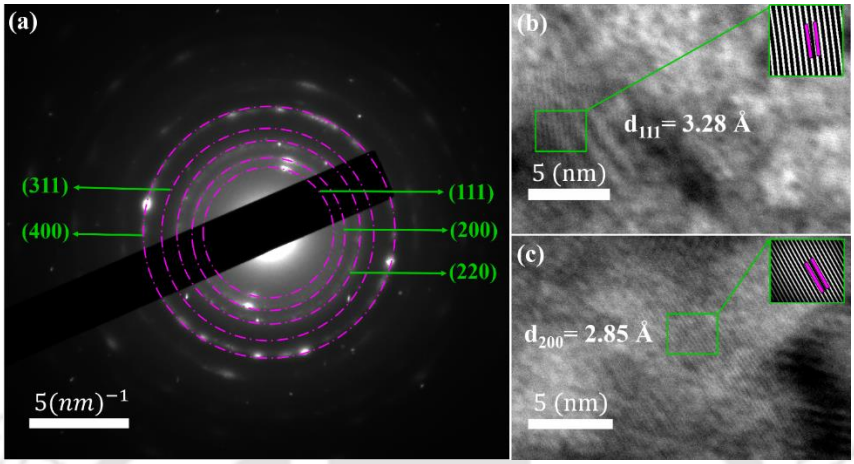

Figure 5.03. (a) SAED pattern of S3 film, and HRTEM image of superlattice planes (b) (111) and (c) (200) with the corresponding ifFT image shown as an inset.

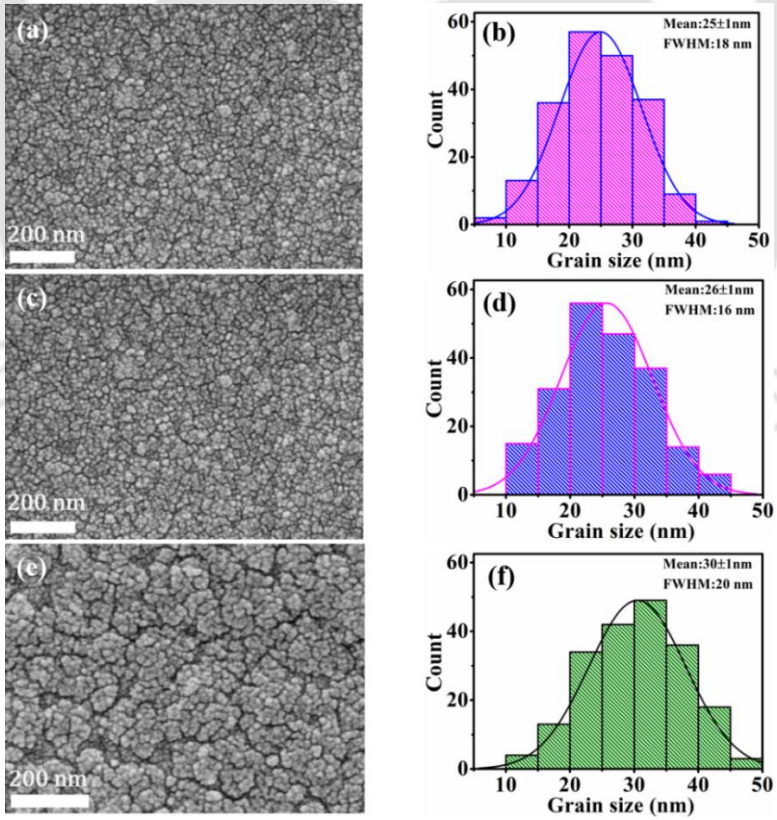

Figure 5.04. FESEM micrographs portraying the morphology of (a) S1, (c) S2, and (e) S3 films. The corresponding grain size distributions are depicted in Figure 5.04 (b, d, and f).

FESEM micrographs of S1, S2, and S3 films are depicted in Figure 5.04 (a, c and e), respectively, with corresponding grain size distributions displayed in Figure 5.04 (b, d, and f). The mean grain sizes are 25±1 nm for S1, 26±1 nm for S2, and 30±1 nm for S3 films, with corresponding FWHM values of 18 nm, 16 nm, and 20 nm, respectively. The granular film morphology observed in all three electrodeposited films is in line with the earlier observations of Duan *et al.* [DUAN2013] and Watanabe *et al.* [WATA2015] on stoichiometric and off-stoichiometric Co-Fe-Sn alloy films. A small amount of clustering of grains, as observed in the micrographs, results in the slightly higher grain size obtained here in comparison with the corresponding D_V of each sample estimated using XRD analysis.

5.4. *Ab initio* studies on Co-Fe-Sn alloys

As mentioned earlier, *ab initio* calculations on stoichiometric Co_2FeSn HA revealed that the bandgap in the minority spin channel is not centred at E_F [PATH2022, PATH2023]. To explore the possibility of inducing half-metallicity in this compound by slightly varying the elemental composition of the Co-Fe-Sn alloy, a 64-atom HA supercell was designed. In the supercell, the substitution of a single atom at its Wyckoff position brings forth a variation of ~1.6 at.% of an element in the unit cell, enabling the fine tuning of the alloy composition. Calculations were carried out for alloy compositions that closely match with those experimentally measured in S1, S2, and S3 films. In all the cases, the Fe concentration was fixed at 21.9 at.%, while the Co and Sn concentrations were systematically varied. To analyze the nature of the minority spin gap, both the TDOS and EDOS were computed for each composition. This was done by incorporating onsite Coulomb repulsion for Co and Fe atoms with U values between 0.0 and 3.0 eV in steps of 0.5 eV. Though there is no firm threshold value for U, it was normally kept within ~3.0 eV to ensure that the calculated magnetic moments are close to M_t calculated from the S-P rule [HUAN2015, PATH2025]. For example, Huang *et al.*[HUAN2015] reported U values of 2.60 eV for Fe and 2.82 eV for Co. Similarly, Khosravizadeh *et al.* [KHOS2009] performed calculations by applying the values in the range of (2.4 - 5.2 eV) for Fe and Co atoms. They suggested that U values up to ~3.0 are enough to generate the M_t close to the values obtained from the S-P rule [HUAN2015]. This is in line with first-principles Hartree-Fock calculations of the effective U parameter, which account for the screening effect in transition metals [KHOS2009]. In case of stoichiometric Co_2FeSn alloy with $L2_1$-type structure, Co atoms occupy the Wyckoff position of 4*c* at (¼, ¼, ¼) and 4*d* at (¾, ¾, ¾), whereas Fe and Sn atoms are positioned at (4*b*)(½, ½, ½) and (4*a*)(0, 0, 0), respectively [MATS2017]. However, in the case of S1 ($Co_{48.4}Fe_{21.9}Sn_{29.7}$ alloy), the concentration of Co

and Fe are lower than the stoichiometric values, whereas Sn is in excess. Consequently, the surplus Sn atoms are expected to occupy the vacant Co and Fe Wyckoff sites in the HA structure. It can be shown that the vacant Co and Fe sites can be occupied by Sn atoms in different ways, as listed in Table 5.01. To choose the stable atomic configuration for sample S1, the one with the minimum free energy has to be identified. Energy minimization of different possible atomic configurations was performed by using $L2_1$-type 64-atom supercell consisting of 31 Co atoms, 14 Fe atoms, and 19 Sn atoms. Table 5.01 presents the free energy values calculated for different atomic configurations of sample S1. As shown, Type-1 exhibits the lowest free energy among all the possible atomic configurations, and hence, it was used for further calculations.

Table 5.01. Different atomic configurations of sample S1 with corresponding free energy.

Configuration	Wyckoff positions				Free energy
	4*c*(¼, ¼, ¼)	4*b*(½, ½, ½)	4*d*(¾, ¾, ¾)	4*a*(0, 0, 0)	(eV)
Type-1	16Co	14Fe, 2Sn	15Co, 1Sn	16Sn	-384.5286
Type-2	16Co	13Fe, 1Co, 2Sn	14Co, 1Fe, 1Sn	16Sn	-384.4668
Type-3	16Co	14Fe, 2Co	13Co, 3Sn	16Sn	-380.3985
Type-4	16Co	13Fe, 2Co, 1Sn	13Co, 1Fe, 2Sn	16Sn	-382.1096

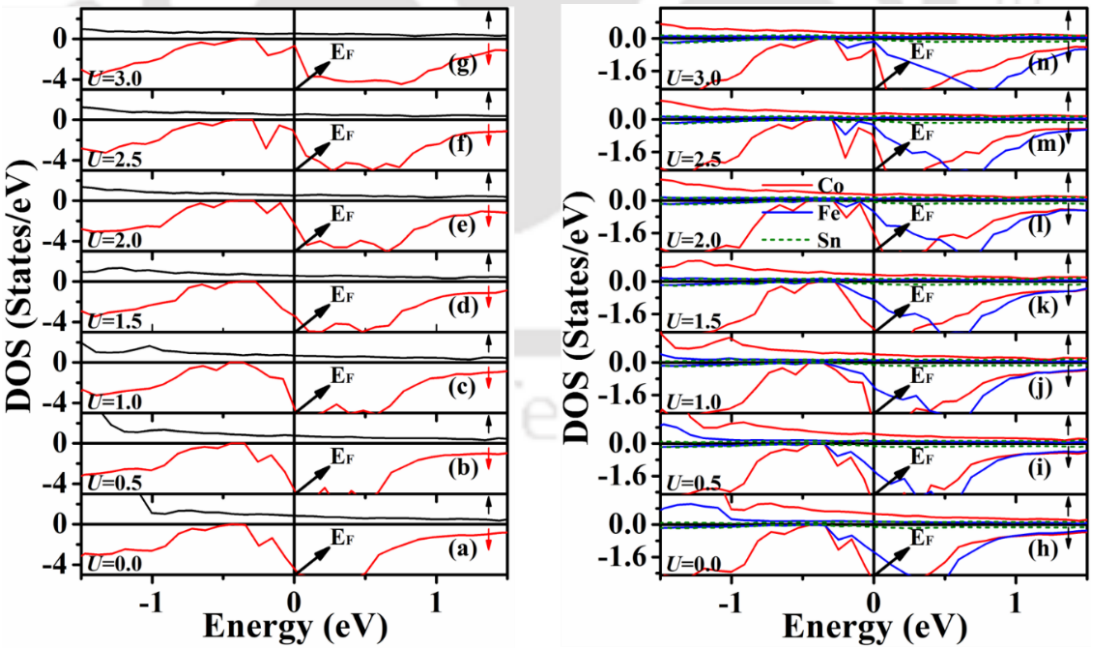

Figure 5.05. (a - g) TDOS near E_F of S1 calculated using $L2_1$-type unit cell with U = 0.0 eV to 3.0 eV in steps of 0.5 eV. (h - n) Corresponding EDOS near E_F of S1 for various U values. In all the figures, 0.0 eV refers to the location of E_F.

Figure 5.05 (a - g) depicts the TDOS of S1 alloy experiencing different extents of electronic correlations. For the alloy with U = 0.0 eV, the gap is not located at E_F. Instead, it is below E_F (~0.43 eV), within the valence band. As the U value is increased incrementally in steps of 0.5 eV from 0.0 eV to 3.0 eV, the gap gradually shifts towards E_F. When U = 3.0 eV, the gap lies below E_F, around 0.27 eV, within the valence band. To get a better picture of the minority states at E_F, the EDOS of each element for the S1 sample was estimated as shown in Figure 5.05 (h - n). It can be seen that the EDOS of the S1 sample near E_F are mainly contributed by Co and Fe states, with a negligible contribution from Sn states, for all U values. It may be noted that the Co states dominate over Fe states for all U values near E_F. Thus, the occurrence of the minority bandgap at E_F in S1 is prevented by the presence of both Co and Fe minority spin states.

In the case of S2 ($Co_{51.6}Fe_{21.8}Sn_{26.6}$) alloy, there are 33 Co atoms, 14 Fe atoms, and 17 Sn atoms. Just as in the case of S1, multiple atomic configurations are possible for S2, too. Additionally, in S2, there may be a chance of Co-Fe (i.e. DO_3-type) type disorder due to excess Co concentration (~51.6 at.%) as compared to the stoichiometric $Co_{50}Fe_{25}Sn_{25}$. Since Co and Fe are neighbouring elements in the periodic table, the difference in their atomic scattering factors is very small. Therefore, it is difficult to identify the presence of DO_3-type disorder in the $L2_1$-type structure from a conventional XRD pattern employing CuKα radiation [BHAT2025, TAKA2010, PATH2025]. Hence, the free energy calculations were also performed for the DO_3-type structure along with the $L2_1$-type structure so that the stable structure for the alloy composition could be correctly identified. From these results, tabulated in Table 5.02, the Type-1 configuration was identified as the lowest energy configuration for S2 sample and was used for further DOS calculations.

Table 5.02. Different atomic configurations with and without DO_3-type disorder of the S2 sample, with corresponding free energy.

Configuration	Wyckoff positions				Free energy (eV)
	4*c*(¼, ¼, ¼)	4*b*(½, ½, ½)	4*d*(¾, ¾, ¾)	4*a*(0, 0, 0)	
Type-1	16Co	14Fe, 1Co, 1Sn	16Co	16Sn	-399.2535
Type-2	16Co	14Fe, 2Co	15Co, 1Sn	16Sn	-396.6752
DO_3-Type-1	12Co, 4Fe	9Co, 7Fe	12Co, 3Fe, 1Sn	16Sn	-394.6728
DO_3-Type-2	12Co, 3Fe, 1Sn	9Co, 7Fe	12Co, 4Fe	16Sn	-394.8185
DO_3-Type-3	13Co, 3Fe	8Co, 7Fe, 1Sn	12Co, 4Fe	16Sn	-397.2117
DO_3-Type-4	12Co, 4Fe	8Co, 7Fe, 1Sn	13Co, 3Fe	16 Sn	-397.2058

Figures 5.06 (a -g) represent the TDOS of S2 alloy with different *U* values in the range of 0.0 to 3.0 eV. With the introduction of *U*, the bandgap in the spin-down channel approaches very close to E_F (~0.04 eV). This position of the minority gap for S2 is closer in comparison to that of stoichiometric Co_2FeSn HA, *i.e.*, at 0.05 eV [PATH2022, PATH2023]. EDOS of S2 alloy are shown in Figure 5.06 (h - n), which clearly indicates that the minority states at E_F are primarily contributed by Fe, with negligible contributions from Co and Sn atoms. Therefore, the deterioration of half-metallicity is primarily attributed to the Fe atoms.

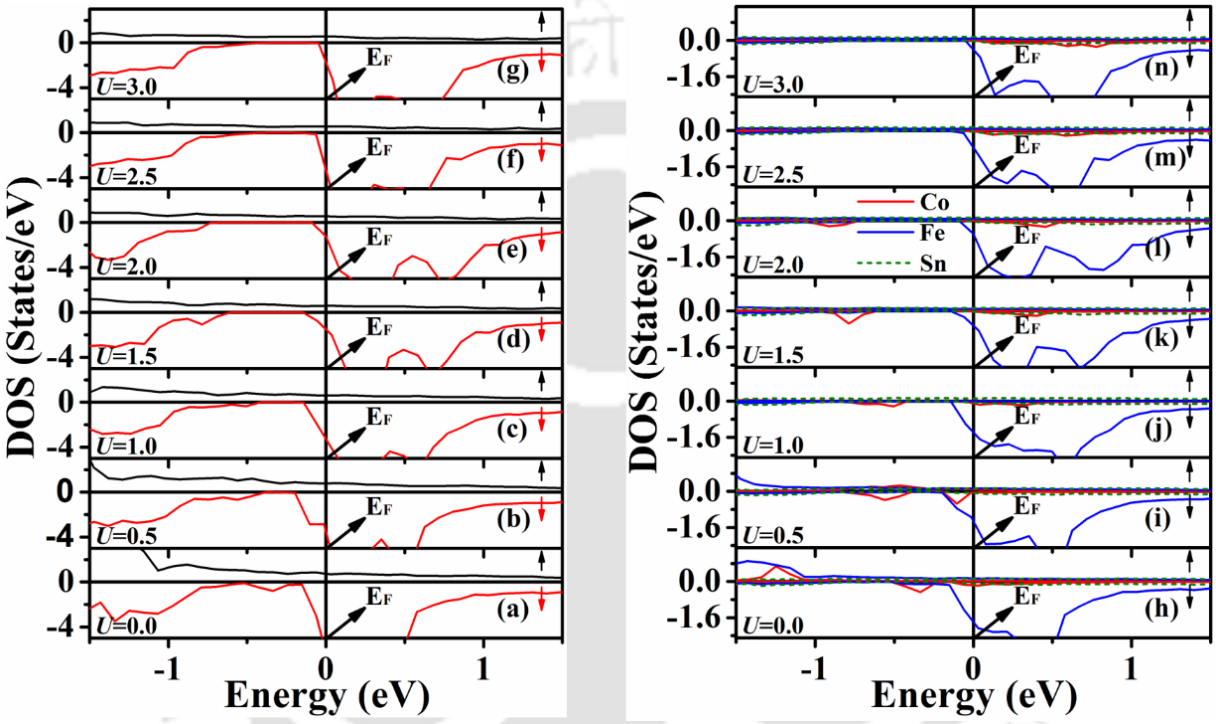

Figure 5.06. (a - g) TDOS near E_F of S2 calculated using $L2_1$-type unit cell with *U* = 0.0 eV to 3.0 eV in steps of 0.5 eV. (h - n) Corresponding EDOS near E_F of S2 for various *U* values. In all the figures, E_F is taken to be at 0.0 eV

In the case of S3 ($Co_{53.1}Fe_{21.9}Sn_{25.0}$) alloy, a stable configuration was determined using 64-atom supercells consisting of 34 Co atoms, 14 Fe atoms, and 16 Sn atoms. The same procedure followed in the case of the S2 sample is also applicable here. Calculated free energy value of each atomic configuration presented in Table 5.03. As portrayed in Table 5.03, Type-1 shows the minimum free energy for the S3 alloy and was therefore selected for further calculations.

Table 5.03. Different atomic configurations of S3 sample with corresponding free energy.

Configuration	Wyckoff positions				Free energy (eV)
	4*c*(¼, ¼, ¼)	4*b*(½, ½, ½)	4*d*(¾, ¾, ¾)	4*a*(0, 0, 0)	
Type-1	16Co	14Fe, 2Co	16Co	16Sn	-404.9206
DO_3-Type-1	12Co, 4Fe	9Co, 7Fe	13Co, 3Fe	16Sn	-402.7540
DO_3-Type-2	13Co, 3Fe	9Co, 7Fe	12Co, 4Fe	16Sn	-402.7577

TDOS plots of sample S3 are shown in Figure 5.07 (a - g) for different values of *U*. By increasing *U* from 0.0 eV to 2.0 eV, the minority gap approaches very close to E_F (-0.026 eV). This means that at *U* = 2.0 eV, there are very small but finite minority states present at E_F. When *U* is increased further, *i.e.*, for *U* = 2.5 and 3.0 eV, the minority states vanish completely, and the system displays a complete half-metallic nature. To understand the contribution from each element, the EDOS of S3 alloy was computed and displayed in Figures 5.07 (h - n). EDOS plots clearly show that up to *U* = 2.0 eV, the gap is destroyed due to the presence of Fe minority states at E_F. However, the value of *U* is increased to 2.5 and 3.0 eV, and the Fe minority states present at E_F completely vanish, making the S3 alloy fully half-metallic.

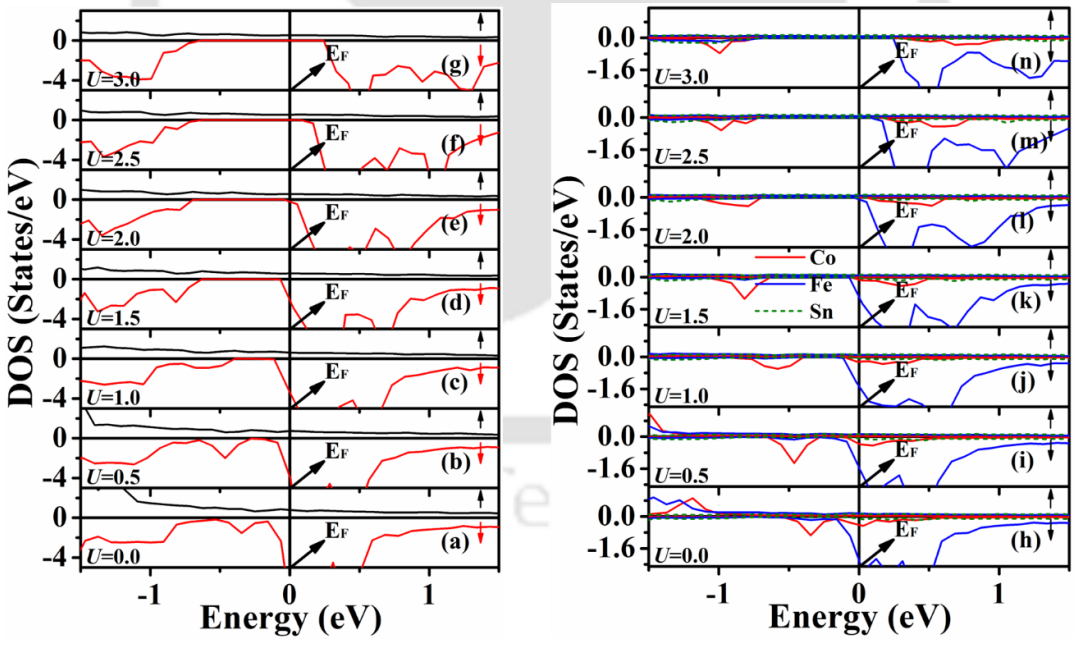

Figure 5.07. (a - g) TDOS in the vicinity of E_F for S3 calculated using the $L2_1$-type unit cell with *U* = 0.0 eV - 3.0 eV. (h - n) Corresponding EDOS of S3 near E_F for different *U* values. In all the figures, 0.0 eV refers to the location of E_F.

In summary, it can be concluded that the system transits from a non-half-metallic to a half-metallic state when the Co concentration is increased from 48.4 at.% (in S1) to 53.1 at.%

(in S3) with a corresponding decrease in Sn concentration from 29.7 at.% (in S1) to 25.0 at.% (in S3), while keeping the Fe concentration nearly constant. The calculations performed on S1, S2, and S3 alloys reveal that, as the U parameter is increased, the minority gap, which was initially below E_F, shifts towards E_F. In contrast to this, in the case of the stoichiometric Co_2FeSn HA, an increase in U up to 1.5 eV causes the minority gap to move towards E_F, and further increments in U make the minority gap move away from E_F [PATH2022, PATH2023]. The theoretically obtained M_t for S1 alloy varies from 4.16 μ_B/f.u. to 5.13 μ_B/f.u. as U increases from 0.0 eV to 3.0 eV. Similarly, M_t ranges from 4.68 μ_B to 5.56 μ_B/f.u. for S2, and from 5.15 μ_B/f.u. and 6.12 μ_B/f.u. for S3.

5.5. Magnetic properties and half-metallicity of Co-Fe-Sn alloys

In-plane magnetization measured as a function of the applied magnetic field for S1, S2, and S3 alloy films at 5 K and 300 K are illustrated in Figure 5.08 (a and b), respectively. Insets in the figures present an enlarged view of data points in the low-field region. At 5 K, film S1 exhibits M_s of 4.58±0.04 μ_B/f.u. and H_c of 309 Oe. Film S2 shows a higher M_s of 5.09±0.04 μ_B/f.u. and a similar H_c of 306 Oe at the same temperature. On the other hand, the S3 film displays a much higher M_s of 5.30±0.04 μ_B/f.u. but lower H_c of 264 Oe as compared to S1 and S2 films. M_s (H_c) values evaluated at 300 K for S1, S2, and S3 films are 4.30±0.04 μ_B/f.u. (242 Oe), 4.76±0.04 μ_B/f.u. (268), and 5.09±0.04 μ_B/f.u. (162 Oe), respectively.

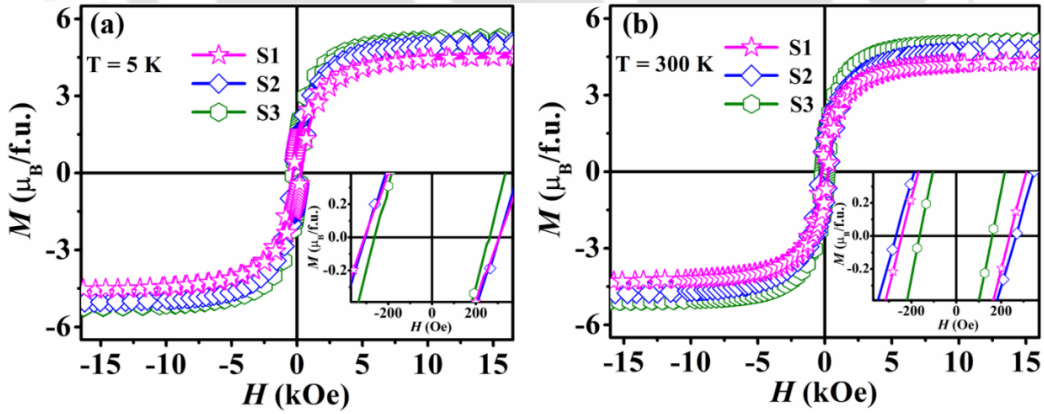

Figure 5.08. Isothermal magnetization curves of S1, S2, and S3 films assessed at (a) 5 K and (b) 300 K. Inset shows a magnified view of data points in the vicinity of the origin.

A slight decrement in M_s values of all three samples is noted at 300 K, aligning with Bloch's law for M_s (T) [HUYN2015, PATH2023]. The relatively small decrease in M_s values at 300 K indicates that S1, S2, and S3 films are well suited for high-temperature device applications with notably high T_C [HUYN2015]. The increment in M_s value of S2 and S3 films,

in comparison to S1 film, can be attributed to the higher concentration of the magnetic elements in these samples. All three films display soft ferromagnetic behaviour in magnetization *versus* applied field curves, consistent with earlier reports on Co-Fe-Sn HA [LITA2013, LIPE2015, PATH2022, PATH2024].

The K_{eff} of S1, S2, and S3 films was estimated from the isothermal initial magnetization curve using the law of approach to magnetic saturation (eq. (1.09)) [ANDR1997, FAHN1978, JINZ1998]. K_{eff} values obtained for S1, S2, and S3 films at 5 K are 6.6×10^6 erg/cm^3, 7.9×10^6 erg/cm^3, and 8.1×10^6 erg/cm^3. The corresponding values at 300 K are 5.8×10^6 erg/cm^3, 6.1×10^6 erg/cm^3, and 7.7×10^6 erg/cm^3, respectively. The estimated K_{eff} values of all three electrodeposited films are consistent with the previously reported values of Co and Fe-based HAs [PATH2022, PATH2023, PATH2024].

Figure 5.09 (a) displays the thermomagnetization curves of S1, S2, and S3 alloy films, measured in the presence of the external magnetic field of 500 Oe. The *M-T* curves indicate the second-order ferromagnetic to paramagnetic phase transformation occurring at temperatures above 1080 K. The inset in Figure 5.09 (a) displays the differential magnetization used for determining T_C. T_C values of S1, S2, and S3 films determined from extremum values of the *M-T* curves shown in the inset of Figure 5.09 (a) are 1084 K, 1092 K, and 1102 K, respectively. An increment in Co concentration with a decrement in Sn concentration has led to an increase in M_s value from 4.58 μ_B/f.u. to 5.30 μ_B/f.u. and a rise in T_C from 1084 K to 1102 K in these alloy films. Such trend in T_C with composition has been observed in other HAs [MAHA2023].

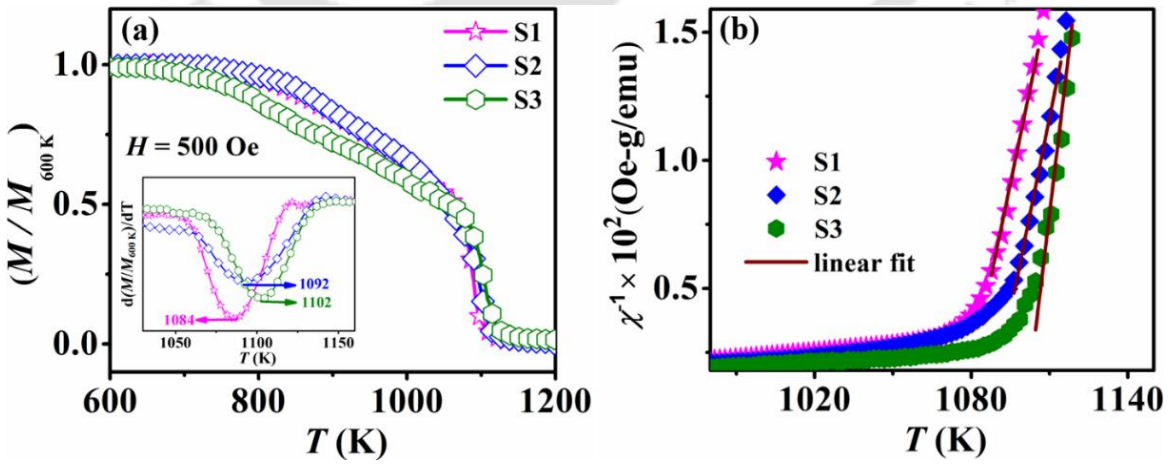

Figure 5.09. (a) *M-T* curves of S1, S2, and S3 films measured under an applied field of 500 Oe. Inset depicts differential magnetization *versus T* curves plotted to locate T_C. (b) χ^{-1} *versus T* plot corresponding to S1, S2, and S3 alloy films, fitted to eq. (2.34).

To understand the nature of spin systems, the Rhodes-Wohlfarth ratio was calculated for S1, S2, and S3 films using eqs. (2.33) and (2.34) [DEKA2015, OTTO1998]. The Rhodes-Wohlfarth ratio derived from χ^{-1}*versus T* fit, as depicted in Figure 5.09 (b), are 1.24 for S1 and 1.10 for S2, indicating itinerant ferromagnetic behaviour, since these values are greater than unity [OTTO1998]. In contrast, the S3 film exhibits a sub-unity Rhodes-Wohlfarth ratio of 0.73, which is considered as a characteristic of half-metallic ferromagnet as per the model given by Otto *et al.* [OTTO1998], as discussed in section 2.2.3 of Chapter 2. This observation is supported by many reports in the literature, in which several half-metallic HAs have been shown to possess Rhodes-Wohlfarth ratios below unity [BHAT2025, DUON2007, SHAM2019, BISW2024]. Thus, the Rhodes-Wohlfarth ratio offers a simple yet effective way to experimentally identify ferromagnetic half-metals, as it can be derived from easily accessible experimental data.

In addition to the Rhodes-Wohlfarth ratio, temperature-dependent electrical resistivity is also a well-established method to illustrate the half-metallicity of a material., Hence, the same was employed to investigate the half-metallicity of S1, S2, and S3 films. Longitudinal resistivity (ρ_{xx}) as a function of temperature was measured in the temperature range of 5 to 300 K for all three films. For detailed analysis of data, the whole range was divided into two regions, *i.e.* 5-70 K (low temperature region) and 70-300 K (high temperature region). In the low temperature regime, the contribution to the resistivity from phonons is negligible. Therefore, ρ_{xx} in this region can be expressed in terms of $\rho_0 + BT^2$ (eq. (2.37)). Here, the T^2 dependence arises from magnonic contributions due to spin-flip scattering, which is characteristic of metallic ferromagnets [CHAT2023, BHAT2025]. However, in the case of half-metallic ferromagnets, the absence of minority (spin-down) states at E_F leads to exponential suppression of spin-flip scattering. As a result, ρ_{xx} can be better described for a half-metallic ferromagnet by the expression, $\rho_0 + BT^2 e^{-\Delta/T}$(eq. (2.38)) [BOMB2013, CHAT2023, BHAT2025]. Here, the parameter Δ is the characteristics temperature (in K) corresponding to the minimum excitation energy (E_g) required for the majority charge carriers to occupy the empty minority states involving spin-flip scattering (*c.f.*, section 2.2.4 of Chapter 2). A high Δ value is a signature of the half-metallic nature of the ferromagnet [BOMB2013, CHAT2023]. In the high temperature region, phononic contribution dominates, leading to linear resistivity behaviour [BOMB2013, CHAT2023]. Figure 5.10 (a, b, and c) illustrate the ρ_{xx} *versus T* plots of S1, S2, and S3 films. The red line represents the fit to eq. (2.37) of the low temperature (< 70 K) resistivity data, whereas the black line corresponds to the fit to the data in the same regime to

eq. (2.38). The insets show a magnified view of data in the low-temperature regime. It can be readily seen from the insets that the red line does not fit well with the low-temperature data of S1, S2, and S3 films. This means that the contributions to the resistivity are not limited to those from electron-magnon alone, but also a significant contribution from the exponential suppression factor in eq. (2.38). This is also asserted by the better fits obtained for all the data for the black line in this region as one moves from S1 to S2 and then to the S3 film, indicating a general decrease in the exponential factor. Having confirmed the relevance of eq. (2.38) to the data in this region for the three samples, let us examine the parameters obtained from the fits. The values of Δ (E_g) obtained by fitting the low-temperature resistivity data of S1, S2, and S3 films are 49.8 K (4.3 meV), 66.7 K (5.8 meV), and 104.3 K (9.0 meV), respectively. The increase in E_g from 4.3 meV (for S1) to 9.0 meV (for S3) reflects a decrease in the exponential term, indicating a corresponding reduction in the spin-flip scattering responsible for the appearance of states in the minority spin channel. Δ (E_g) values reported for half-metallic Co_2MnGe and Co_2FeSi alloys are 79 K (6.8 meV) and 103 K (8.8 meV), respectively [CHAT2023]. Δ (E_g) of S1 and S2 are 49.8 K (4.3 meV), and 66.7 K (5.8 meV), which are considerably lower than the reported values for Co_2MnGe and Co_2FeSi [CHAT2023]. It can be noticed that *P* of S1 is ~14 %, whereas it is ~51 % in the case of S2. The relatively low value of E_g of S1 (4.3 meV) and S2 (5.8 meV) reveals that the chances of spin-flip scattering become less pronounced in S2 as compared to S1. On the other hand, Δ(E_g) obtained for S3 is 104.3 K (9.0 meV), which is very close to those of the reported half-metallic HAs mentioned above [CHAT2023]. It has to be pointed out that $\Delta(E_g)$ deduced for S3 film from experimental data is much smaller than the theoretically estimated value of 2782 K (240 meV) using *ab initio* calculations. This discrepancy between the experimental and theoretical values could be primarily attributed to thermally induced disorder in the synthesized samples occurring at finite measurement temperatures. This should be contrasted with the defect-free $L2_1$-type structure assumed at 0 K in the theoretical calculations [BHAT2025]. In addition to this, unavoidable small deviations in the actual alloy composition from the theoretically assumed one may also contribute to this discrepancy. Such deviation between experimental and theoretically derived E_g is common and has also been observed in other half-metallic ferromagnets [BHAT2025, CHAT2023, BOMB2013].

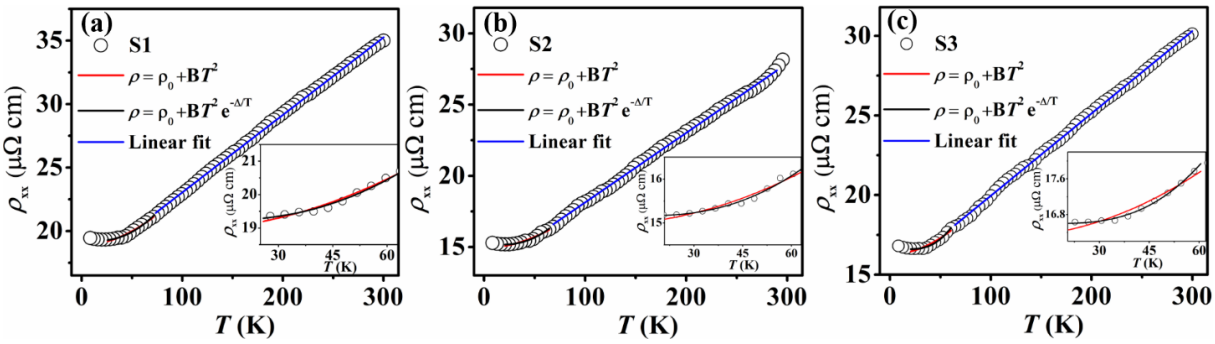

Figure 5.10. Temperature-dependent electrical resistivity curves of (a) S1, (b) S2, and (c) S3 films measured between 5 and 300 K. Red and black colour lines represent fits to the low-temperature data corresponding to eqs. (2.37) and (2.38), respectively. Insets show a magnified view of the fitted curves in the low-temperature region. Blue lines are fits that portray the linear variation of resistivity in the high temperature region.

Thus, analysis of the temperature-dependent electrical resistivity data reveals a progressive enhancement in half-metallic character as we move from S1 to S2, and then to S3, with S3 exhibiting half-metallic nature. In the high-temperature region, all three samples show a linear variation with respect to T as depicted by the blue line in Figure 5.10 (a, b, and c). This behaviour is attributed to the dominant electron-phonon scattering process at high temperatures.

5.6. Summary

The results obtained in investigations on off-stoichiometric Co-Fe-Sn HA films are summarized below:

- Highly crystalline off-stoichiometric Co-Fe-Sn alloy films with $L2_1$-type ordered structure were prepared by varying the precursor amounts while maintaining all other deposition parameters constant.
- Synthesized S1, S2, and S3 films of 1400 nm thickness exhibit granular film morphology with mean grain sizes of 25±1, 26±1, and 30±1 nm, respectively. All the alloy films show soft ferromagnetic behaviour characterized by high M_s ranging from 4.58 to 5.30 μ_B/f.u. at 5 K, elevated T_C between 1084 K and 1102 K, and high K_{eff} in the range of 6.6 to 8.1×10^6 erg/cc at 5 K.
- *Ab initio* study reveals that the minority gap lies just below E_F in S1 and S2 alloys, whereas E_F is well inside the minority gap in S3 alloy. A comparison of the three alloys shows how the minority gap can be tuned towards E_F with judicious choice of composition in Co-Fe-Sn alloys.

- The Rhodes-Wohlfarth ratio of S1 and S2 films show that they behave like itinerant ferromagnets, whereas film S3 acts as a half-metallic ferromagnet. Additionally, low-temperature DC electrical resistivity studies on S1, S2 and S3 films reveal the gradual suppression of spin-flip scattering and the emergence of half-metallic nature in S3 with a large $\Delta(E_g)$ value of 104.3 K (9.0 meV).

In conclusion, this comprehensive study on composition-dependent Co-Fe-Sn alloy films demonstrate a viable way to tune the minority spin gap, enabling a transition from non-half-metallic to a fully half-metallic state. In addition to experimentally validating the theoretically predicted half-metallicity in Co-Fe-Sn alloys, this study also presents a low-cost method for their synthesis.

Chapter 6

Effect of Cr substitution for Fe on the properties of electrodeposited $Co_{48.4}Fe_{21.9}Sn_{29.7}$ alloy film

As discussed in Chapters 3 and 5, the presence of additional valence electrons in Fe as compared to Cr or Mn leads to the emergence of minority spin states at E_F in stoichiometric Co_2FeSn alloy [OZDO2007, PATH2022, PATH2023], thereby disrupting its half-metallicity. One way to suppress these minority states at E_F is by tuning the composition, as demonstrated in Chapter 5. An alternate procedure is to introduce a sufficient amount of a low valence fourth element into the Co-Fe-Sn alloy system to steer the minority spin band gap towards E_F, thereby restoring half-metallicity [OZDO2007, PATH2024]. This chapter explores the possibility of inducing half-metallicity in the non-half-metallic $Co_{48.4}Fe_{21.9}Sn_{29.7}$ alloy through partial substitution of Fe with Cr, which has a lower valency than Fe.

6.1. Electrodeposition of Co-Fe-Sn and Co-Fe-Cr-Sn alloy films

Co-Fe-Sn and Co-Fe-Cr-Sn films were electrodeposited in potentiostatic mode on 0.2 mm thick Cu substrates, following the procedures detailed in Chapter 2. The electrolyte solution for the ternary Co-Fe-Sn film consisted of 7.0878 g of $CoSO_4 \cdot 7H_2O$, 0.1785 g of $SnSO_4$, and 1.7040 g of $FeSO_4 \cdot 7H_2O$ dissolved in 250 ml of DI water. For quaternary Co-Fe-Cr-Sn film, the electrolyte was prepared using 2.6538 g of $FeSO_4 \cdot 7H_2O$, 2.6538 g of $Cr_2(SO_4)_3 \cdot 7H_2O$, 0.3924 g of $SnSO_4$, and 7.0878 g of $CoSO_4 \cdot 7H_2O$, in 250 ml of DI water. Additionally, both electrolytes were supplemented with 30 g of sodium gluconate, 0.0050 g of peptone, 4.1160 g of NaCl, and 4.6380 g of boric acid as additives. All the electrodepositions were carried out under the pre-optimized V_{dep} of -4.0 V for t_{dep} of 150 s [PATH2022, PATH2024]. The thickness of all films was determined to be 780 ± 10 nm using cross-sectional FESEM studies. The poorly crystallized as-deposited films were gently cleaned with acetone, air dried, and flame sealed under vacuum in fused silica ampoules at a pressure of ~10^{-3} Pa. The sealed ampoules

containing films were heat treated at an optimized temperature of 550 ℃ for 1 hour to induce proper crystallization of the alloy films.

6.2. Composition analysis of Co-Fe-Sn and Co-Fe-Cr-Sn alloy films

The overall elemental composition of the processed Co-Fe-Sn and Co-Fe-Cr-Sn films was determined using EDS studies as already described in Chapter 2. The average value of the overall composition obtained for the ternary and quaternary alloy films are $Co_{47.9\pm1.3}Fe_{21.7\pm1.4}Sn_{30.4\pm1.7}$ and $Co_{48.3\pm1.2}Fe_{19.3\pm1.5}Cr_{3.1\pm0.3}Sn_{29.3\pm1.2}$, respectively. Figures 6.01 (a and b) display a representative EDS spectrum of the heat treated Co-Fe-Sn and Co-Fe-Cr-Sn alloy films after eliminating the contributions from the Cu substrate, C tape and the conductive Au coating.

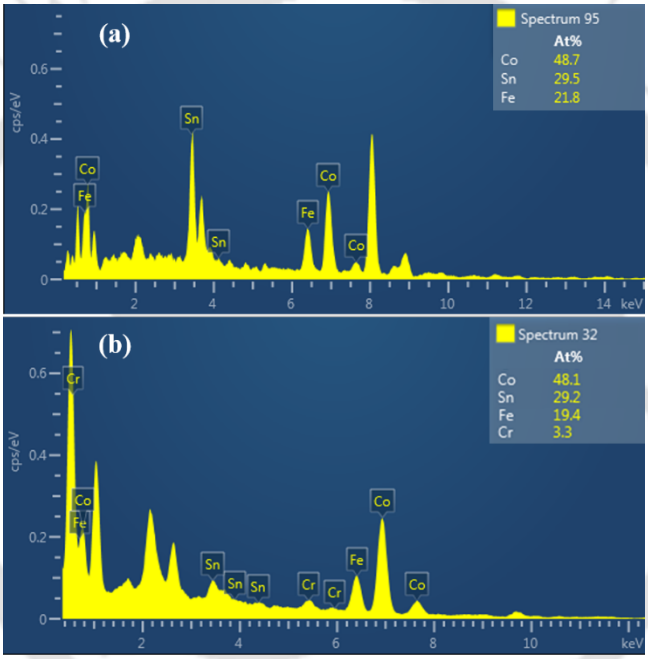

Figure 6.01. Typical EDS spectrum of (a) Co-Fe-Sn and (b) Co-Fe-Cr-Sn film after elimination of Cu, C and Au peaks.

6.3. Structural and morphological analysis of Co-Fe-Sn and Co-Fe-Cr-Sn alloy films

Figure 6.02 (a) displays the simulated XRD pattern of $Co_{48.3}Fe_{19.3}Cr_{3.1}Sn_{29.3}$ alloy film represented in black colour. Since the intensity of characteristic superlattice reflections (111) and (200) are very feeble in the simulated XRD pattern, these reflections are not observable in the experimental XRD patterns of both ternary (olive colour) and quaternary (blue colour) HA films shown in Figure 6.02 (a). In contrast, the SAED pattern presented in Figure 6.03 (a) reveals the superlattice reflections (111) and (200), which confirms the formation of the $L2_1$-type ordered structure in $Co_{48.3}Fe_{19.3}Cr_{3.1}Sn_{29.3}$ film. The ifFT of the lattice fringe for the (111)

and (200) superlattice planes obtained from HRTEM images are depicted in Figure 6.03 (b and c). The XRD patterns of $Co_{47.9}Fe_{21.7}Sn_{30.4}$ and $Co_{48.3}Fe_{19.3}Cr_{3.1}Sn_{29.3}$ films were refined using the Rietveld method employing the $L2_1$-type unit cell, and the results are portrayed in Figure 6.02 (b and c). The χ^2 value, which reflects the quality of the refinement, was found to be 1.66 and 1.52 for $Co_{47.9}Fe_{21.7}Sn_{30.4}$ and $Co_{48.3}Fe_{19.3}Cr_{3.1}Sn_{29.3}$ HA films, respectively. The lattice parameter obtained after the Rietveld refinement for the ternary and quaternary alloy film was found as 5.7253 Å and 5.6813 Å, respectively. The observed *a* value of both films are in close agreement with previously reported values of electrodeposited Co-Fe-Sn alloy films [PATH2022, PATH2024]. D_V of $Co_{47.9}Fe_{21.7}Sn_{30.4}$ and $Co_{48.3}Fe_{19.3}Cr_{3.1}Sn_{29.3}$ films estimated using Schërrer's equation (eq. (2.15)) [CULL2014] are 22±1 nm, 21±1 nm, respectively.

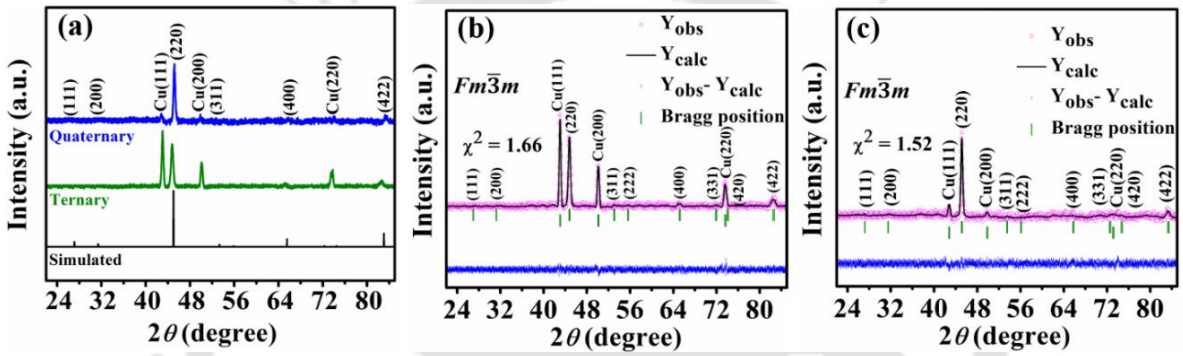

Figure 6.02. (a) Simulated and experimental XRD patterns of $Co_{47.9}Fe_{21.7}Sn_{30.4}$ and $Co_{48.3}Fe_{19.3}Cr_{3.1}Sn_{29.3}$ films. Rietveld refined XRD patterns of (b) $Co_{47.9}Fe_{21.7}Sn_{30.4}$ and (c) $Co_{48.3}Fe_{19.3}Cr_{3.1}Sn_{29.3}$ films performed using unit cells with space group 225 [$Fm\bar{3}m$].

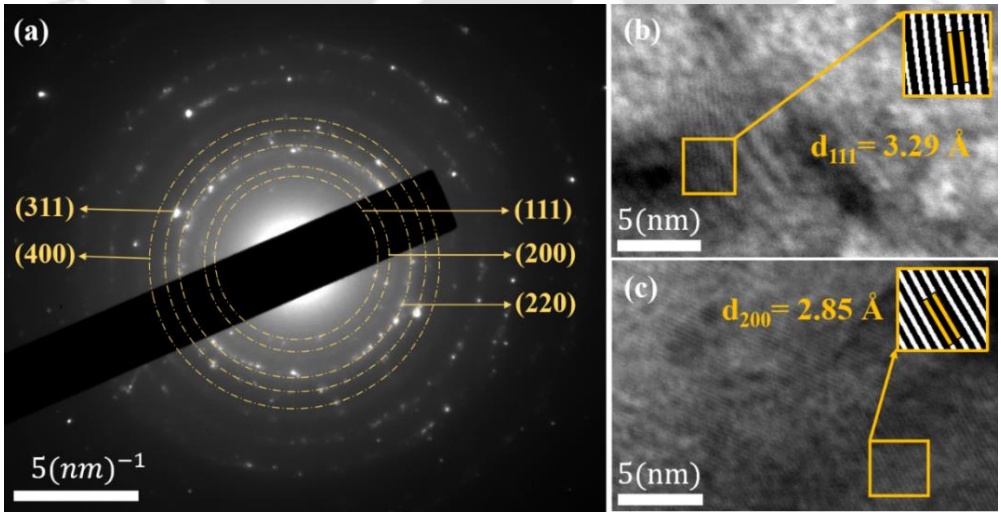

Figure 6.03. (a) SAED pattern of $Co_{48.3}Fe_{19.3}Cr_{3.1}Sn_{29.3}$ film. HRTEM images of superlattice (b) (111) and (c) (200) planes of the film with corresponding ifFT images shown as insets.

The FESEM micrographs of $Co_{47.9}Fe_{21.7}Sn_{30.4}$ and $Co_{48.3}Fe_{19.3}Cr_{3.1}Sn_{29.3}$ films are displayed in Figure 6.04 (a and c) along with the corresponding grain size distributions in Figure 6.04 (b and d). The mean grain size of $Co_{47.9}Fe_{21.7}Sn_{30.4}$ alloy film was found to be 28±1 nm with FWHM of 13 nm, whereas the mean grain size of the $Co_{48.3}Fe_{19.3}Cr_{3.1}Sn_{29.3}$ sample was found to be 25±1 nm with FWHM of 12 nm, as depicted in the plots. The granular film morphology is evident in both the ternary and quaternary alloy films. The mean grain size of these films is consistent with published data on electrodeposited Co-based HA films [DUAN2013, PATH2022, PATH2024]. A small amount of clustering of grains, as observed in the micrographs, results in the slightly higher grain size obtained here in comparison with the corresponding D_V of alloy films estimated using XRD analysis.

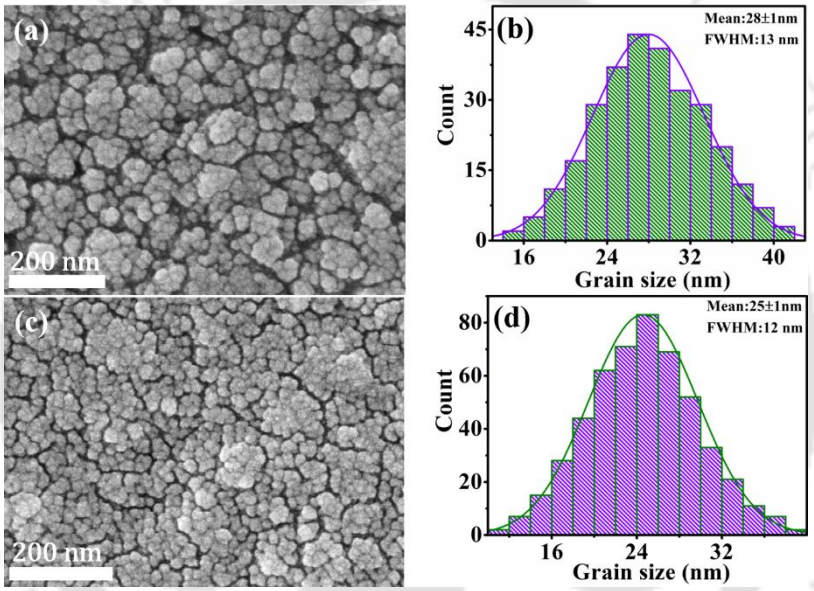

Figure 6.04. FESEM micrographs displaying the morphology of (a) $Co_{47.9}Fe_{21.7}Sn_{30.4}$ and (c) $Co_{48.3}Fe_{19.3}Cr_{3.1}Sn_{29.3}$ films. (b and d) Corresponding grain size distributions.

6.4. Density of electronic states and magnetic moment of $Co_{48.4}Fe_{21.9}Sn_{29.7}$ alloy

In stoichiometric Co_2FeSn alloy with $L2_1$-type structure, Co atoms occupy the Wyckoff position 4*c* at (¼, ¼, ¼) and 4*d* at (¾, ¾, ¾), whereas Fe and Sn atoms are positioned at 4*b*(½, ½, ½) and 4*a*(0, 0, 0), respectively [MATS2017, PATH2022]. In the off-stoichiometric $Co_{47.9}Fe_{21.7}Sn_{30.4}$ alloy, concentrations of Co and Fe are lower than the stoichiometric values, whereas Sn is in excess. Consequently, the surplus Sn atoms are expected to occupy the vacant Co and Fe Wyckoff sites in the HA structure. As discussed in section 5.4 of Chapter 5, vacant Co and Fe sites can be occupied by Sn atoms in four unique ways as listed in Table 6.01. To identify the most stable structure among the possible configurations, energy minimization was

carried out on them. At absolute zero temperature, the total energy corresponds to the free energy [VASP2025]. The calculations on $Co_{48.4}Fe_{21.9}Sn_{29.7}$ alloy (which is very close to the film composition of $Co_{47.9\pm1.3}Fe_{21.7\pm1.4}Sn_{30.4\pm1.7}$) were carried out using an $L2_1$-type unit cell with a 64-atom supercell, comprising 31 Co atoms, 14 Fe atoms, and 19 Sn atoms, which provided a composition resolution of ~1.56 at.% for each element. As shown in Table 6.01, Type-1 configuration exhibits the lowest free energy among all the considered configurations. Hence, the Type-I configuration was used for further calculations as it corresponds to the most stable atomic configuration.

Table 6.01. Different atomic configurations of $Co_{48.4}Fe_{21.9}Sn_{29.7}$ alloy with corresponding free energy.

Configuration	Wyckoff positions				Free energy (eV)
	4*c*(¼, ¼, ¼)	4*b*(½, ½, ½)	4*d*(¾, ¾, ¾)	4*a*(0, 0, 0)	
Type-1	16Co	14Fe, 2Sn	15Co, 1Sn	16Sn	-387.7060
Type-2	16Co	13Fe, 1Co, 2Sn	14Co, 1Fe, 1Sn	16Sn	-387.6306
Type-3	16Co	14Fe, 2Co	13Co, 3Sn	16Sn	-383.6375
Type-4	16Co	13Fe, 2Co, 1Sn	13Co, 1Fe, 2Sn	16Sn	-385.2437

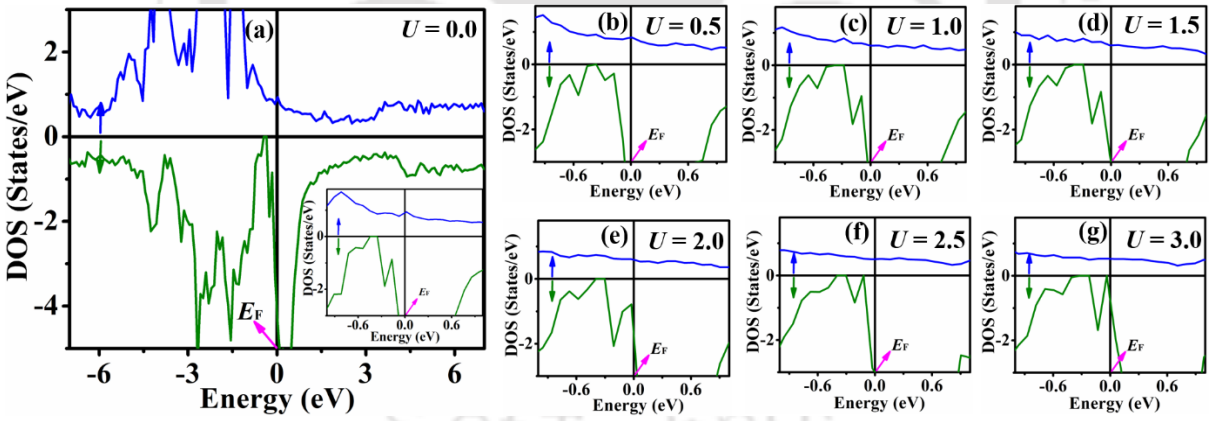

Figure 6.05. (a) TDOS of $Co_{48.4}Fe_{21.9}Sn_{29.7}$ alloy computed with U = 0.0 eV. Inset provides an enlarged view of the data near E_F. (b - g) Expanded view of TDOS of the alloy near E_F computed with U values ranging from 0.5 to 3.0 eV in steps of 0.5 eV. In all the figures, 0.0 eV refers to the location of E_F.

To obtain a clear account of the electron states near the minority spin gap, the TDOS and EDOS were then calculated. In all the calculations, the U was implemented from 0.0 eV to 3.0 eV incrementally in 0.5 eV steps. The U values were limited to 3.0 eV to ensure that the

estimated M_t are close to the S-P value [HUAN2015]. Figure 6.05 (a) presents the TDOS of $Co_{48.4}Fe_{21.9}Sn_{29.7}$ alloy computed with U = 0.0 eV. The inset in the figure shows the magnified view of the TDOS near E_F. Figure 6.05 (b - g) portray the expanded view of TDOS plots obtained with U = 0.5 - 3.0 eV. When U is 0.0 eV, the gap in the minority spin band lies nearly 0.35 eV below E_F in the valence band. As the U value is gradually increased in steps of 0.5 eV from 0.0 to 3.0 eV, the gap progressively shifts toward E_F. When U = 3.0 eV, the gap lies very close (~0.03 eV) below E_F. To illustrate the contribution of the minority spin states corresponding to each constituent element at E_F, the EDOS of $Co_{48.4}Fe_{21.9}Sn_{29.7}$ alloy is depicted in Figure 6.06 (a - g).

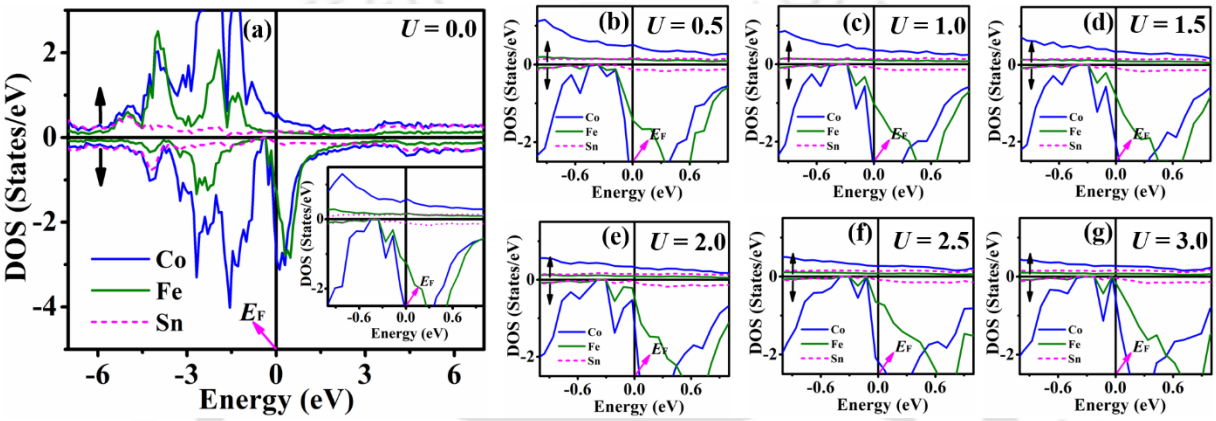

Figure 6.06. (a) EDOS of $Co_{48.4}Fe_{21.9}Sn_{29.7}$ alloy computed with U = 0.0 eV. Inset in the figure provides an enlarged view near E_F. (b - g) Expanded view of EDOS near E_F obtained with U ranging from 0.5 to 3.0 eV. In all the figures, 0.0 eV refers to the location of E_F.

The EDOS plot obtained with U = 0.0 eV, shown in Figure 6.06 (a), indicates that minority states at E_F are mainly due to Co and Fe, with negligible contribution from Sn. It can be noted that the Co states are more pronounced than the Fe states for all U values near E_F. Thus, the minority bandgap at E_F, which is the signature of half-metallicity, is destroyed due to the presence of both Co and Fe minority spin states. The reason for the destruction of the half-metallic gap in $Co_{48.4}Fe_{21.9}Sn_{29.7}$ alloy is due to the presence of both Co and Fe states. The calculated M_t varies from 4.25 to 5.19 μ_B/f.u. as the U value increases from 0.0 to 3.0 eV. Analysis of the electronic structure of $Co_{48.4}Fe_{21.9}Sn_{29.7}$ alloy reveals that a slight deviation from the stoichiometric composition $Co_{50}Fe_{25}Sn_{25}$ to $Co_{48.4}Fe_{21.9}Sn_{29.7}$ results in the minority spin gap shifting from ~0.05 eV [PATH2022] to ~0.03 eV below E_F within the valence band. Thus, a slight deviation from stoichiometric $Co_{50}Fe_{25}Sn_{25}$ to $Co_{48.4}Fe_{21.9}Sn_{29.7}$ does not entirely

suppress the minority spin states at E_F but only reduces them from 5.76 states/eV [PATH2022] to 0.75 states/eV.

6.5. Density of electronic states and magnetic moment of Cr substituted $Co_{48.4}Fe_{21.9}Sn_{29.7}$ alloy

In the ternary $Co_{48.4}Fe_{21.9}Sn_{29.7}$ alloy, the minority spin bandgap lies ~0.03 eV below E_F within the valence band, as discussed earlier. This results in the presence of finite minority spin states at E_F, thereby imparting a non-half-metallic character to the system. To suppress these minority states, partial substitution of low-valent Cr for Fe was explored. A 64-atom supercell comprising 31 Co, 12 Fe, 2 Cr, and 19 Sn atoms providing an elemental resolution of ~1.56 at.% was attempted. This yields the quaternary $Co_{48.4}Fe_{18.8}Cr_{3.1}Sn_{29.7}$ alloy composition, obtained by replacing two Fe atoms (~3.1 at.%) with Cr in the $Co_{48.4}Fe_{21.9}Sn_{29.7}$ ternary alloy composition. This composition is very close to the film composition of $Co_{48.3\pm1.2}Fe_{19.3\pm1.5}Cr_{3.1\pm0.3}Sn_{29.3\pm1.2}$. As discussed in section 5.4 of Chapter 5, when the ternary $Co_{48.4}Fe_{21.9}Sn_{29.7}$ alloy deviates from the stoichiometric $Co_{50}Fe_{25}Sn_{25}$ composition, the constituent atoms can arrange themselves in four possible unique atomic configurations. Similarly, in the case of the quaternary $Co_{48.4}Fe_{18.8}Cr_{3.1}Sn_{29.7}$ alloy formed by substituting two Cr atoms for Fe in the ternary composition, four distinct atomic configurations are possible, which are presented in Table 6.02. To identify the most stable structural configuration amongst these, free energy calculations were performed on each atomic configuration, and the results are presented in Table 6.02. The last column of the table shows that the Type-2 configuration has the lowest free energy and was therefore chosen for further computations. Since $Co_{48.4}Fe_{18.8}Cr_{3.1}Sn_{29.7}$ alloy contains transition metals Co, Fe, and Cr, onsite Coulomb repulsion between 3*d* electrons must be considered by including the *U* in the calculations [HUAN2015, PATH2022, PATH2023]. The *U* values were limited to 3.0 eV in the calculations to ensure that the estimated magnetic moment value is close to the M_t calculated from the S-P rule [HUAN2015].

Table 6.02. Free energy of various atomic configurations of $Co_{48.4}Fe_{18.8}Cr_{3.1}Sn_{29.7}$ alloy.

Configuration	Wyckoff positions				Free energy (eV)
	4*c*(¼, ¼, ¼)	4*b*(½, ½, ½)	4*d*(¾, ¾, ¾)	4*a*(0, 0, 0)	
Type-1	16Co	12Fe, 2Cr, 2Sn	15Co, 1Sn	16Sn	-385.7631
Type-2	16Co	12Fe, 1Cr, 3Sn	15Co, 1Cr	16Sn	-387.9329
Type-3	16Co	12Fe, 3Co, 1Sn	12Co, 2Cr, 2Sn	16Sn	-382.3970
Type-4	16Co	12Fe, 1Co, 3Sn	14Co, 2Cr	16Sn	-387.3436

Figure 6.07 (a) presents the TDOS of $Co_{48.4}Fe_{18.8}Cr_{3.1}Sn_{29.7}$ alloy with U = 0.0 eV. The inset in the figure provides a magnified view of TDOS near E_F. Figure 6.07 (b - g) portrays the expanded view of TDOS near E_F for U = 0.5 - 3.0 eV. When U = 0.0 eV, the minority gap lies below E_F at ~0.39 eV in the valence band. As the U value is increased, the minority gap shifts towards E_F, and at U = 2.5 eV, the minority gap reaches very close to E_F (~0.06 eV) with an extremely small number (~0.05 states/eV) of states at E_F. Further, increase in U to 3.0 eV leads to the appearance of the full minority gap at E_F. The calculated EDOS of $Co_{48.4}Fe_{18.8}Cr_{3.1}Sn_{29.7}$ alloy is shown in Figure 6.08 (a - g). EDOS of $Co_{48.4}Fe_{18.8}Cr_{3.1}Sn_{29.7}$ alloy depicted in Figure 6.08 (a) reveals that at U = 0.0 eV, Co minority states dominate over Fe with negligible contribution from Cr and Sn minority states at E_F. As the U value is increased, the minority DOS contributions from both Co and Fe decrease with the dominance of Co over Fe up to U = 2.0 eV, as portrayed in Figure 6.08 (b - e). As the U value reaches 2.5 eV, the contributions from both Co and Fe minority DOS at E_F become very small, with nearly zero contributions from Cr and Sn states shown in Figure 6.08 (f). On further increment of U, *i.e.* at U = 3.0 eV, minority DOS contributions from all elements become zero, which results in the appearance of a half-metallic gap at E_F as depicted in Figure 6.08 (g).

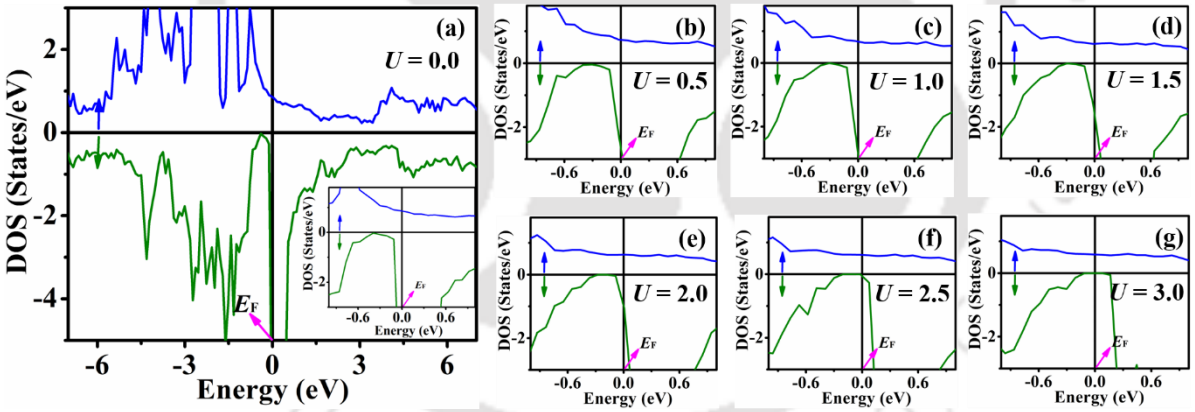

Figure 6.07. (a) TDOS of $Co_{48.4}Fe_{18.8}Cr_{3.1}Sn_{29.7}$ alloy calculated with U = 0.0 eV. The inset in the figure shows the enlarged view near E_F. (b - g) Enlarged view of TDOS near E_F obtained with U values ranging from 0.5 to 3.0 eV. In all the figures, 0.0 eV refers to the location of E_F.

Thus, $Co_{48.4}Fe_{21.9}Sn_{29.7}$ transforms from a non-half-metal to a fully half-metallic $Co_{48.4}Fe_{18.8}Cr_{3.1}Sn_{29.7}$ alloy when ~3.1 at.% of low valent Cr atom is substituted in place of Fe atom. The theoretically calculated magnetic moment of the $Co_{48.4}Fe_{18.8}Cr_{3.1}Sn_{29.7}$ alloy increases from 4.08 to 4.94 μ_B/f.u. as the U parameter is increased from 0.0 to 3.0 eV. When U = 3.0 eV, the theoretically estimated magnetic moment equals the M_t calculated from the S-P rule.

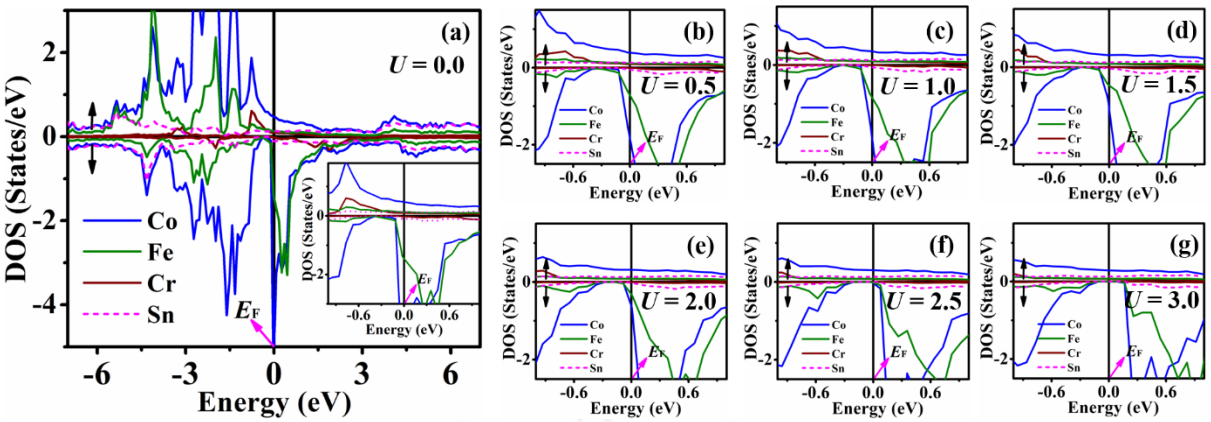

Figure 6.08. (a) EDOS of $Co_{48.4}Fe_{18.8}Cr_{3.1}Sn_{29.7}$ evaluated with U = 0.0 eV. Inset provides an enlarged view near E_F. (b - g) shows an enlarged view of EDOS near E_F with U = 0.5 - 3.0 eV. In all the figures, E_F is taken to be at 0.0 eV.

6.6. Magnetic properties and half-metallicity of the ternary and quaternary alloys

Figure 6.09 (a and b) display the isothermal magnetization *versus* field curves, recorded at 5 K and 300 K for $Co_{47.9}Fe_{21.7}Sn_{30.4}$ and $Co_{48.3}Fe_{19.3}Cr_{3.1}Sn_{29.3}$ alloy films, respectively. The inset in both figures offers an enlarged view of the curves close to the origin. The M_s (H_c) values of the ternary $Co_{47.9}Fe_{21.7}Sn_{30.4}$ alloy film are 4.52±0.04 μ_B/f.u. (233 Oe) at 5 K and 4.45±0.04 μ_B/f.u. (192 Oe) at 300 K, respectively. For the quaternary $Co_{48.3}Fe_{19.3}Cr_{3.1}Sn_{29.3}$ alloy film, the corresponding values of M_s (H_c) are 4.48±0.04 μ_B/f.u. (220 Oe) at 5 K, and 4.42±0.04 μ_B/f.u. (190 Oe) at 300 K, respectively. The electrodeposited films show soft ferromagnetic properties, which are consistent with previous reports in the literature on electrodeposited Co-based HAs [DUAN2013, PATH2022, PATH2024, WATA2015]. A small reduction in M_s (~1.5%) in the case of $Co_{47.9}Fe_{21.7}Sn_{30.4}$ and ~1.3% in the case of $Co_{48.3}Fe_{19.3}Cr_{3.1}Sn_{29.3}$ film was observed at 300 K as compared to 5 K, which is consistent with Bloch's law for $M_s(T)$ [PATH2023, SRIV2024]. The minimal reduction in M_s observed at the ambient temperature in both the films is indicative of their high T_C and their suitability in high-temperature applications [GELL2013, PATH2023, SRIV2024].

K_{eff} of $Co_{47.9}Fe_{21.7}Sn_{30.4}$ and $Co_{48.3}Fe_{19.3}Cr_{3.1}Sn_{29.3}$ films were estimated from the isothermal initial magnetization curve using the law of approach to magnetic saturation (eq. (1.9)) [ANDR1997, FAHN1978, JINZ1998]. K_{eff} value obtained for the $Co_{47.9}Fe_{21.7}Sn_{30.4}$ film at 5 K (300 K) is 3.0×10^6 erg/cc (1.7×10^6 erg/cc). The corresponding value for $Co_{48.3}Fe_{19.3}Cr_{3.1}Sn_{29.3}$ film is 5.8×10^6 erg/cc (4.7×10^6 erg/cc). K_{eff} values for both $Co_{47.9}Fe_{21.7}Sn_{30.4}$ and $Co_{48.3}Fe_{19.3}Cr_{3.1}Sn_{29.3}$ electrodeposited films are consistent with the

previously reported values of Co and Fe-based electrodeposited HA films [PATH2022, PATH2023, PATH2024].

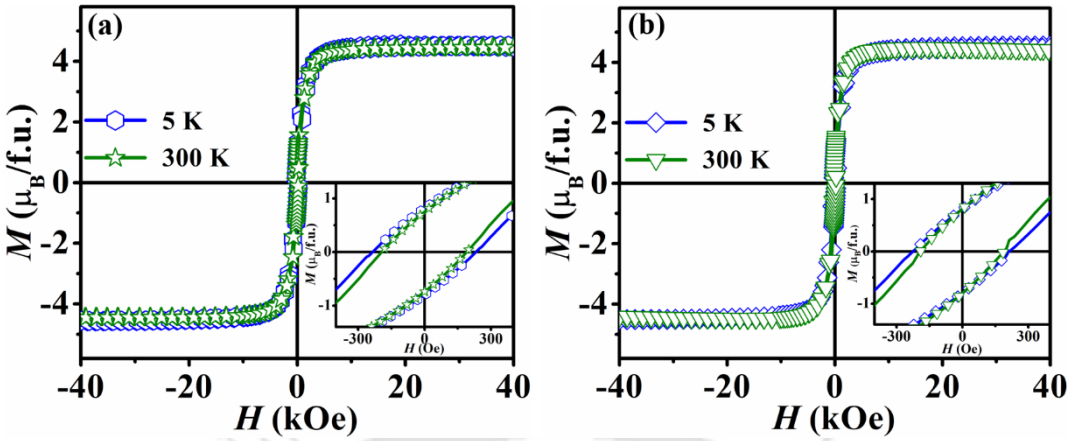

Figure 6.09. *M-H* loops of (a) $Co_{47.9}Fe_{21.7}Sn_{30.4}$ and (b) $Co_{48.3}Fe_{19.3}Cr_{3.1}Sn_{29.3}$ films recorded at 5 K and 300 K. Inset shows an enlarged view of the data points near the origin.

Temperature-dependent electrical resistivity offers a simple procedure to illustrate the half-metallic nature of a material. Hence, the same was employed to investigate the occurrence of half-metallicity in $Co_{48.3}Fe_{19.3}Cr_{3.1}Sn_{29.3}$ alloy film. ρ_{xx} as a function of temperature was measured in the temperature range of 5 to 300 K for the $Co_{48.3}Fe_{19.3}Cr_{3.1}Sn_{29.3}$ alloy film. For detailed analysis of data, the whole range was divided into two regions, *i.e.*, 5-70 K (low temperature region) and 70-300 K (high temperature region). In the low temperature regime, the contribution to the resistivity from phonons is negligible. Therefore, ρ_{xx} in this region can be expressed in terms of $\rho_0 + BT^2$ (eq. (2.37)). Here, the T^2 dependence arises from magnonic contributions due to electron-magnon spin-flip scattering, which is characteristic of metallic ferromagnets [CHAT2023]. However, in the case of half-metallic ferromagnets, the absence of minority (spin-down) states at E_F leads to exponential suppression of electron-magnon spin-flip scattering. As a result, ρ_{xx} can be better described for a half-metallic ferromagnet by the expression, $\rho_0 + BT^2 e^{-\Delta/T}$(equation (2.38)) [BHAT2025, BOMB2013, CHAT2023]. Here, the parameter Δ is the characteristic temperature (in K) corresponding to the minimum excitation energy (E_g) required for the majority charge carriers to occupy the empty minority states involving spin-flip scattering (*c.f.*, section 2.2.4 of Chapter 2). A high Δ value is a signature of the half-metallic nature of the ferromagnet [BHAT2025,BOMB2013, CHAT2023, PATH2025]. In the high temperature region, phononic contribution dominates, leading to linear resistivity behaviour [BOMB2013, CHAT2023]. Figure 6.10 illustrates the ρ_{xx} *versus T* plot obtained for the $Co_{48.3}Fe_{19.3}Cr_{3.1}Sn_{29.3}$ alloy film. The inset in the figure provides a

magnified view of the low-temperature regime, which clearly shows that the red coloured fitted line corresponding to the electron-magnon spin-flip scattering formula without exponential suppression is a poor fit to the low-temperature data. On the other hand, by incorporating exponential suppression in the magnonic term, eq. (2.38) makes a significantly improved fit to the low-temperature data as shown in Figure 6.10. This is affirmed by the improved fit to data points as depicted by the black colour fitted line. An enlarged view of the data is presented as an inset in Figure 6.10. E_g (Δ) extracted from the fitting is 7.1 meV (82.6 K), which is comparable to the $E_g(\Delta)$ value of 6.8 meV (79 K) of the well-stablished half-metallic Co_2MnGe HA [CHAT2023]. Hence, it is evident that the electrodeposited $Co_{48.3}Fe_{19.3}Cr_{3.1}Sn_{29.3}$ alloy film demonstrates half-metallic character, which validates the prediction from *ab initio* calculations. In the high-temperature region (*i.e.*, 70 K - 300 K), the $Co_{48.3}Fe_{19.3}Cr_{3.1}Sn_{29.3}$ sample shows a linear variation of $\rho_{xx}$with respect to temperature as depicted by the violet fitted curve in Figure 6.10. This behaviour is attributed to electron-phonon scattering as expected at high temperatures.

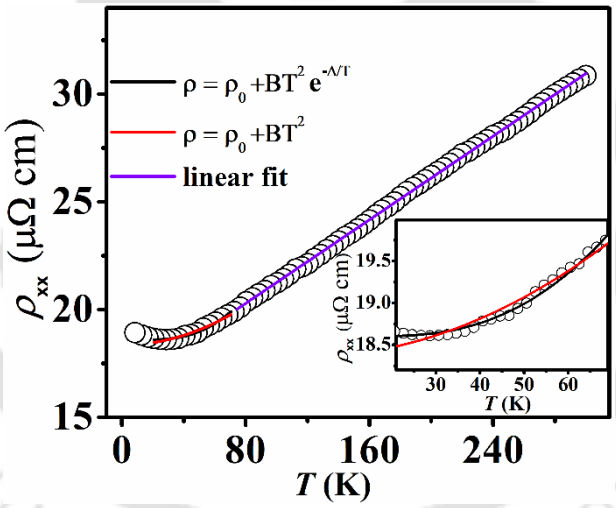

Figure 6.10. Temperature-dependent electrical resistivity curve of $Co_{48.3}Fe_{19.3}Cr_{3.1}Sn_{29.3}$ alloy film recorded from 5 to 300 K. The red and black lines represent fits to the low-temperature data using eqs. (2.37) and (2.38), respectively. The violet line depicts the linear variation of resistivity in the high temperature range (70 K - 300 K). The inset offers an enlarged view of the two fitted curves in the low temperature region.

6.7. Summary

The results obtained from the investigations on the processed $Co_{47.9}Fe_{21.7}Sn_{30.4}$ and $Co_{48.3}Fe_{19.3}Cr_{3.1}Sn_{29.3}$ alloy films are summarized below:

- Highly crystalline ternary $Co_{47.9}Fe_{21.7}Sn_{30.4}$ and quaternary $Co_{48.3}Fe_{19.3}Cr_{3.1}Sn_{29.3}$ alloy films with $L2_1$-type ordered structure, having a thickness of 780±10 nm, were obtained after heat treatment of the films electrodeposited on low-cost Cu substrate.
- Heat treated $Co_{47.9}Fe_{21.7}Sn_{30.4}$ and $Co_{48.3}Fe_{19.3}Cr_{3.1}Sn_{29.3}$ alloy films exhibit granular film morphology with the mean grain size of 28±1 and 25±1 nm, respectively. Both the alloy films show soft ferromagnetic behaviour characterized by high M_s of 4.52 μ_B/f.u. for $Co_{47.9}Fe_{21.7}Sn_{30.4}$ and 4.48 μ_B/f.u. for $Co_{48.3}Fe_{19.3}Cr_{3.1}Sn_{29.3}$ at 5 K and high K_{eff} in the range of 3.0 to 5.8 × 10^6 erg/cc at 5 K.
- *Ab initio* calculations performed on $Co_{48.4}Fe_{21.9}Sn_{29.7}$ alloy revealed its non-half-metallic nature due to the extra valence electrons of Fe. Substitution of ~3.1 at.% of lower-valent Cr in the place of Fe leads to the appearance of a minority band gap at E_F in the $Co_{48.4}Fe_{18.8}Cr_{3.1}Sn_{29.7}$ alloy.
- Low temperature electrical resistivity measurements conducted on $Co_{48.3}Fe_{19.3}Cr_{3.1}Sn_{29.3}$ alloy film revealed an exponential suppression of electron-magnon scattering, characterized by $\Delta(E_g)$ of 82.1 K (7.1 meV), which supports the half-metallicity predicted by *ab initio* calculations.

Thus, a small substitution of low valent Cr for Fe atoms invokes half-metallicity in the non-half-metallic $Co_{48.4}Fe_{21.9}Sn_{29.7}$ HA by effectively suppressing the minority DOS at E_F without causing significant variation in magnetic properties. In addition to experimentally validating the theoretically predicted half-metallicity in Co-Fe-Cr-Sn alloys, this study provides a cost-effective and facile technique to synthesize the quaternary HA films.

Chapter 7

Investigations on electrodeposited Fe_2CoSn alloy

After a detailed investigation of the structural, morphological, magnetic, electrical, electronic, thickness-dependent, and compositional properties of Co-Fe-Sn HAs, the next goal is to explore another promising alloy with the same constituent elements, *i.e.* Fe_2CoSn. As discussed in Chapter 1, this alloy exhibits high M_s, elevated T_C, and significant P [PATH2023]. However, the synthesis of Fe_2CoSn alloy using conventional methods poses considerable challenges, necessitating the use of alternative approaches [ZHAN2005, PATH2023]. Gao *et al.* [GAOS2015] were the first to report the fabrication of Fe_2CoSn HA films using non-equilibrium electrodeposition technique, which is particularly well-suited for synthesizing alloys that are difficult to obtain through conventional methods [DUAN2013, WATA2015, PATH2022]. Their electrodeposited films had a thickness of ≥2 μm and crystallized in *A*2-type disordered structure, exhibiting M_s of 3.5 μ_B/f.u. which is substantially lower than the theoretically predicted value of 5.54 μ_B/f.u. [MATS2017]. This discrepancy was attributed to the poor crystalline ordering in their electrodeposited films [PATH2023]. Despite its potential for superior properties, Fe_2CoSn remains a relatively unexplored HA. Notably, its electronic DOS in the most energetically stable configuration has yet to be explored. The only available DOS study on this alloy as reported by Khan *et al.* [KHAN2018], focused on the $L2_1$-type full HA structure, which is not the energetically favourable configuration for this alloy [MATS2017]. Therefore, the realization of single-phase, stoichiometric Fe_2CoSn films with enhanced structural and magnetic properties, along with the exploration of their electronic characteristics of the most stable structural configuration, is essential for harnessing the full potential of this compound. In this chapter, the successful synthesis of *X*-type ordered Fe_2CoSn films on polycrystalline Cu substrates *via* electrodeposition at room temperature, followed by vacuum heat treatment, is presented. This includes a comprehensive discussion of the film's elemental composition, surface morphology, crystal structure, and magnetic properties. These

experimental results are further supported by theoretical calculations to evaluate the magnetic and electronic properties of the alloy.

7.1. Electrodeposition of Fe_2CoSn alloy film

Fe_2CoSn HA film was deposited on high-purity (99.99%) polycrystalline Cu substrate by the potentiostatic electrodeposition process already explained in Chapter 2. Optimized amounts of metal sulphates, *viz*., $FeSO_4.7H_2O$ (7.8608 g), 3.7238 g of $CoSO_4.7H_2O$, and 0.3207 g of $SnSO_4$, were used as precursors in 250 ml of ascorbic acid stabilized DI water. 4.6380 g boric acid, 41160 g of NaCl, 30 g of sodium gluconate, and 0.0050 g of peptone were used as additives. The film deposition was carried out using potentiostatic mode with an optimized V_{dep} of -4.0 V [PATH2022, PATH2023] for t_{dep} of 75 s. The details of the deposition process are mentioned in section 2.1.1.1 of Chapter 2. The thickness of the film was determined to be 320±5 nm using cross-sectional FESEM measurement. The poorly crystallized as-deposited film was thoroughly cleaned with acetone, air dried, and vacuum flame sealed in fused silica ampoules at a pressure of ~10^{-3} Pa. The sealed ampoules containing films was heat treated at an optimized temperature of 550 °C for 1 hour to induce proper crystallization in the alloy film.

7.2. Compositional analysis of Fe_2CoSn alloy film

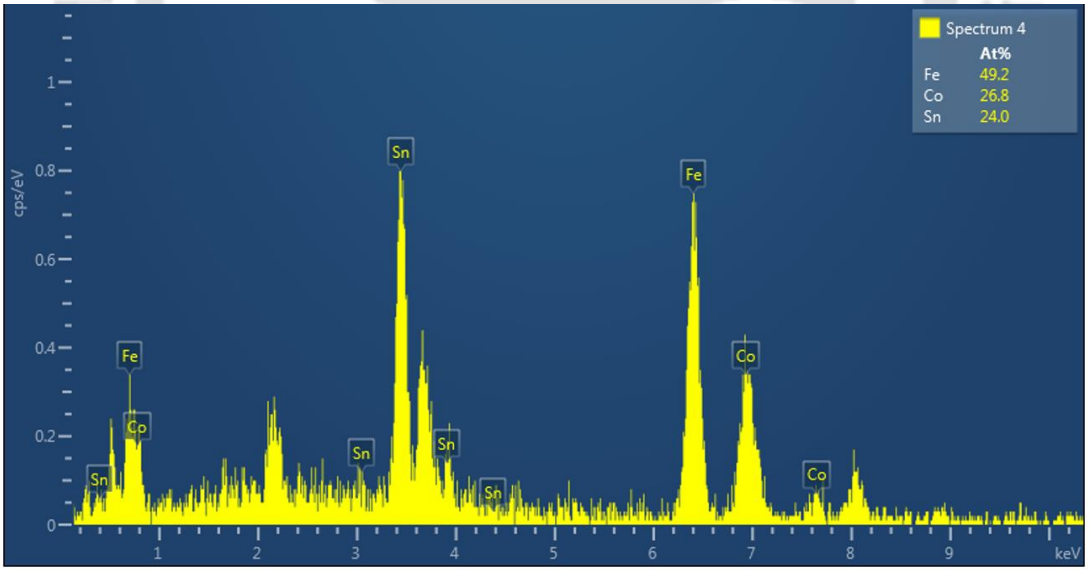

Figure 7.01. Reduced EDS data of Fe_2CoSn alloy film after subtraction of Cu, C and Au peaks.

Figure 7.01 displays a typical raw EDS spectrum of the heat treated Fe_2CoSn alloy film. The detected peaks in the spectrum other than those of the constituent elements (Fe, Co, and Sn) originate from the Cu substrate, the C tape used to mount the sample on the electrode, and the

Au coating applied on the film surface to prevent charging effects. After excluding the Cu, C, and Au contributions from the raw data, the actual elemental composition of the specimen was determined as illustrated in Figure 7.01. From the figure, it is clear that Fe, Co, and Sn are the only constituents present, and their concentrations (in at.%) are 49.2, 26.8, and 24.0, respectively. The overall composition of the films was evaluated by taking the average of 10 such individual spectral scans. The average elemental composition of the deposited film, determined by EDS analysis, was $Fe_{49.8\pm1.1}Co_{26.2\pm1.2}Sn_{24.0\pm1.2}$, which is close to the stoichiometric $Fe_{50.0}Co_{25.0}Sn_{25.0}$ composition.

7.3. Structure and morphology of Fe_2CoSn alloy film

As discussed in Chapter 1, the X_2YZ alloys possess the stable $L2_1$-type full HA structure if the atomic number of the X element is higher than that of the Y element [YINM2015, BHAT2025]. However, if the atomic number of the Y element is higher than that of the X element, the resulting structure is referred to as *X*-type inverse HA structure [YINM2015, BHAT2025]. Though this definition categorizes Fe_2CoSn as an inverse HA, one needs to ascertain the same by ensuring that this atomic configuration has the lowest energy. Figure 7.02 presents the energy *versus* unit cell volume plots to identify the most stable atomic configuration for Fe_2CoSn alloy. Energy *versus* volume curve corresponding to *X*-type unit cell lies significantly below that of the $L2_1$-type unit cell, thereby confirming the *X*-type structure as the energetically favourable configuration for Fe_2CoSn HA. This is in line with the assignment of *X*-type inverse HA structure to Fe_2CoSn by Matsushita *et al.* [MATS2017] and Faleev *et al.* [FALE2017].

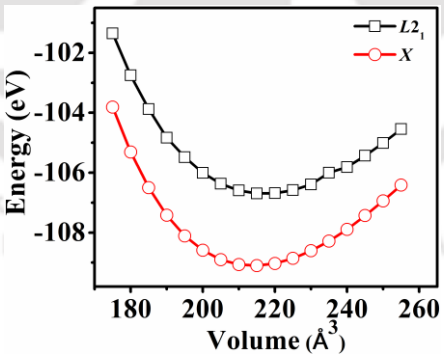

Figure 7.02. Energy *versus* unit cell volume curves for Fe_2CoSn HA using $L2_1$ and *X*-type unit cells.

Figure 7.03 (a) represents the simulated and experimental XRD patterns (as-deposited, as well as heat treated) of the Fe_2CoSn alloy film. The simulated XRD pattern was generated using the *X*-type inverse HA unit cell of Fe_2CoSn using CaRIne crystallography 3.1 software. The film, in its as-deposited state, exhibits a notably weak (220) reflection, which appears as a

shoulder to the strong (111) reflection emerging from the copper substrate. The presence of the (220) reflection suggests the *A*2-type HA phase formation in the as-deposited state. However, its low intensity in comparison to the copper peaks indicates poor crystallization of the HA phase. The XRD pattern of the heat treated film reveals reflections from (220), (400), and (422) planes associated with the HA phase. The absence of the superlattice (111) and (200) reflections in the XRD pattern of the heat treated film can be attributed to the inherently low intensity of these two reflections even in the simulated pattern, as depicted in Figure 7.03 (a).

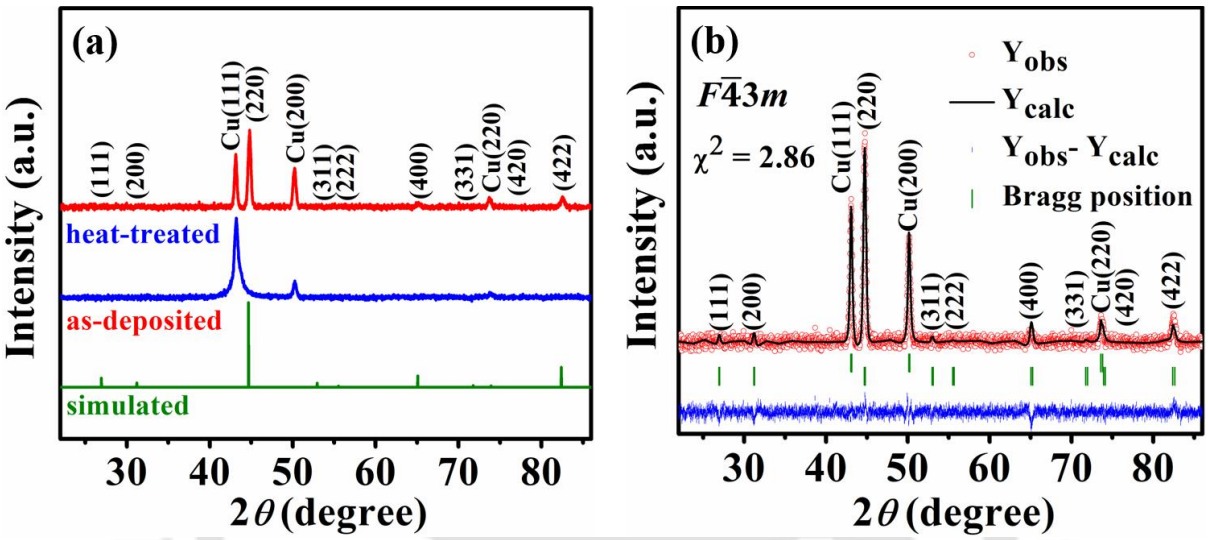

Figure 7.03. (a) XRD patterns of simulated, as-deposited and heat treated Fe_2CoSn films. (b) Rietveld refined XRD pattern of heat treated Fe_2CoSn film using space group 216 [$F\bar{4}3m$].

However, the SAED pattern of the heat treated Fe_2CoSn film reveals the presence of both the (111) and (200) reflections as illustrated in Figure 7.04 (a). Additionally, Figure 7.04 (b, and c) provide HRTEM images displaying lattice fringes corresponding to the two superlattice planes (111) and (200). The insets in Figure 7.04 (b, and c) display the ifFT of the lattice planes. These confirm the formation of the stable *X*-type inverse HA structure in the heat treated Fe_2CoSn film. It is worthy to point out that the only previous report on Fe_2CoSn films by Gao *et al.*[GAOS2015] reported *A*2-type disordered structure in their as-deposited films, due to their high deposition rate [GAOS2015, PATH2023]. The lattice parameter obtained from the Rietveld refinement of XRD data of the heat treated Fe_2CoSn film is 5.7293 Å, which lies within the range of experimental values of 5.6900 - 5.7500 Å reported for Fe_2CoSn nanowires [KHAN2018]. D_v of the heat treated Fe_2CoSn film was estimated using the Schërrer's equation (eq. (2.15)), yielding a value of 22±1 nm.

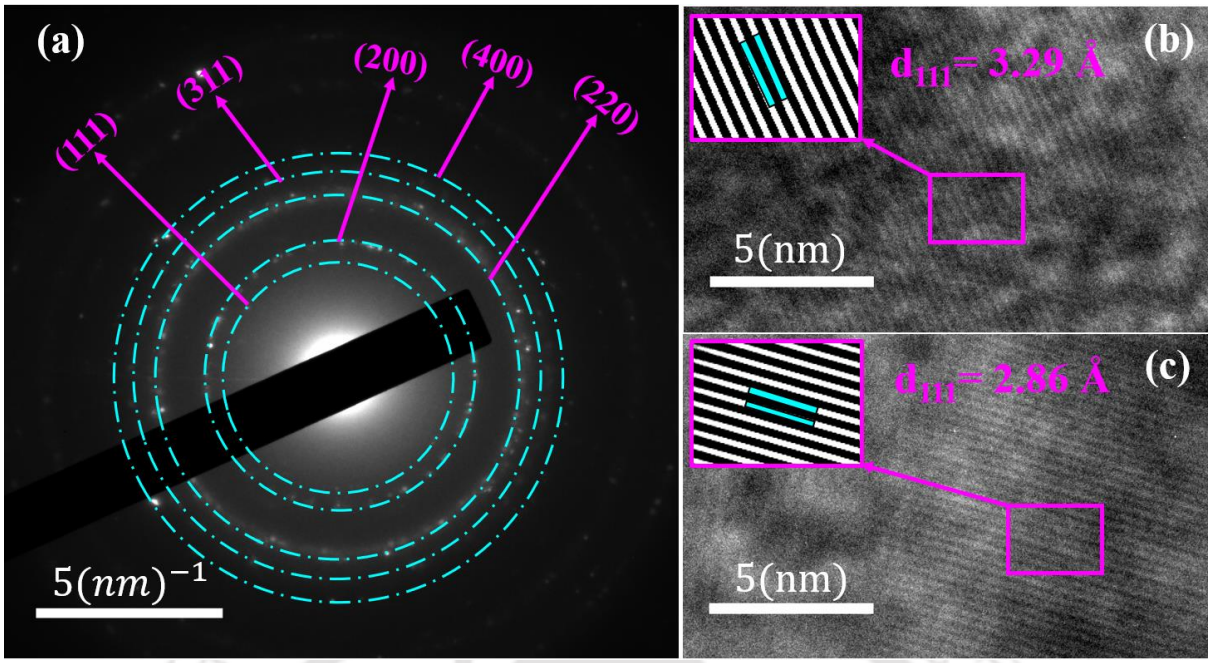

Figure 7.04. (a) SAED pattern of heat treated Fe_2CoSn alloy film, along with HRTEM image of superlattice planes (b) (111) and (c) (200) with corresponding ifFT images shown as insets.

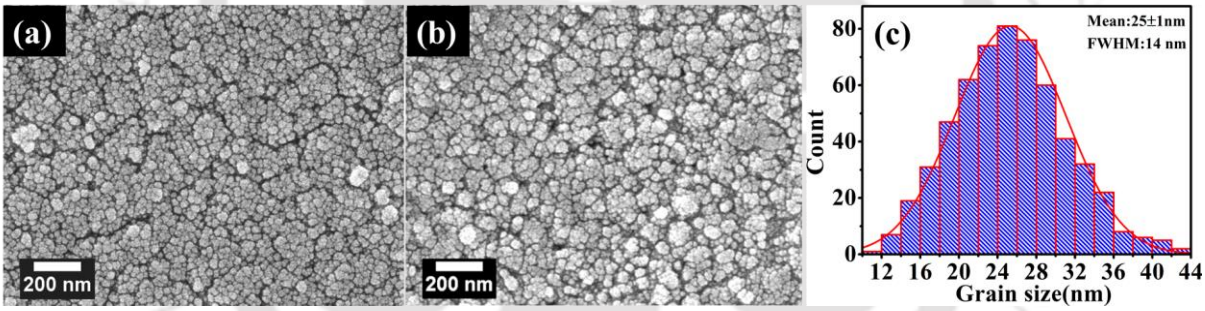

Figure 7.05. FESEM micrographs showing granular morphology of (a) as-deposited and (b) heat treated Fe_2CoSn films. (c) Grain size distribution of heat treated Fe_2CoSn film.

Figure 7.05 (a, and b) portray the FESEM micrographs of as-deposited and heat treated Fe_2CoSn films, respectively. Both the as-deposited and heat treated films show granular film morphology. Grain growth and aggregation of grains can be observed in the heat treated film as compared to the as-deposited film. Figure 7.05 (c) portrays the grain size distribution of heat treated Fe_2CoSn film, which ranges between 10 and 44 nm, with a mean grain size of 25±1 nm and FWHM of 14 nm. Gao *et al.* [GAOS2015] observed similar morphology with a grain size distribution of 20 - 30 nm in their electrodeposited Fe_2CoSn alloy film.

7.4. Magnetic properties of Fe_2CoSn alloy film

In-plane isothermal magnetization curves of as-deposited and heat treated Fe_2CoSn films recorded at 5 K and 300 K are displayed in Figure 7.06 (a and b), respectively. The enlarged view of the data near the origin in Figure 7.06 (a and b) helps in assessing the H_c and M_r of the synthesized films with better accuracy. The lower M_s and H_c of the as-deposited film are attributed to poor crystalline order due to its *A*2-type disordered structure. An enhancement in M_s and H_c is observed upon heat treatment due to enhancement in the crystalline order (*X*-type structure), which further improves the long-range ferromagnetic interactions.

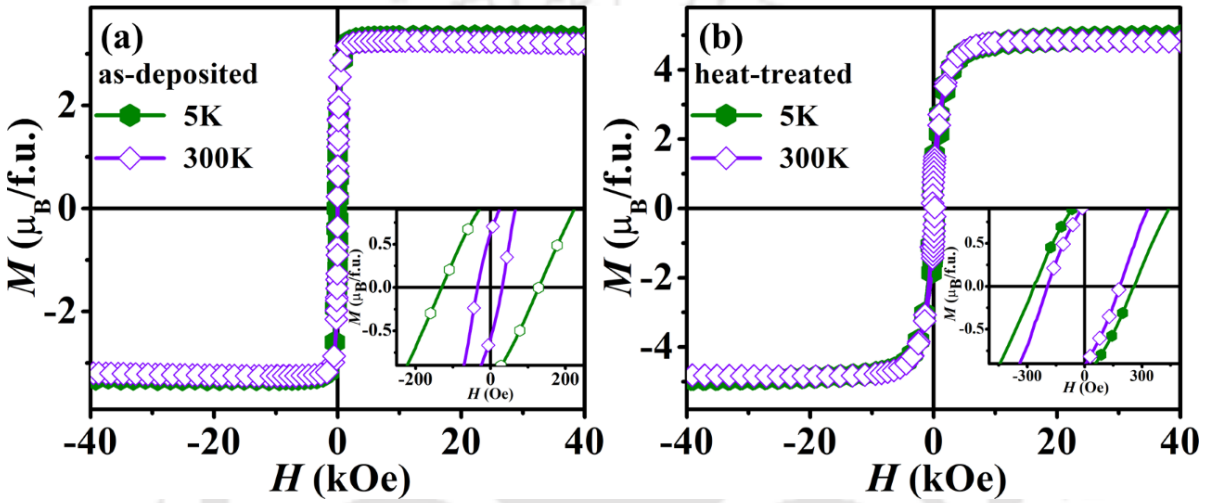

Figure 7.06. *M-H* curves recorded at 5 K and 300 K for (a) as-deposited and (b) heat treated Fe_2CoSn films. Insets provide an enlarged view of the data close to the origin.

The M_s and H_c values of the as-deposited Fe_2CoSn film at 5 K (300 K) are 3.33±0.02 μ_B/f.u. and 128 Oe (3.25±0.02 μ_B/f.u. and 33 Oe), and the corresponding values of the heat treated film are 4.98±0.04 μ_B/f.u. and 266 Oe (4.82±0.04 μ_B/f.u. and 190 Oe), respectively. The obtained M_s values in the present study are higher than the value of 3.5 μ_B/f.u reported by Gao *et al.* [GAOS2015] for their *A*2-type Fe_2CoSn films. This enhancement in M_s value of the synthesized films is attributed to the higher crystalline order and better morphology of the present films [PATH2023]. A slight decrement in M_s (~3%) was observed at 300 K compared to 5 K, which is accordance with Bloch's law of M_s (T) [PATH2023, SRIV2024]. The small reduction in M_s indicates the suitability of Fe_2CoSn in high-temperature applications [GELL2013, PATH2023, SRIV2024].

K_{eff} of the Fe_2CoSn film was estimated from the initial magnetization curve using the law of approach to magnetic saturation (equation (1.9)) [ANDR1997, FAHN1978, JINZ1998]. For the as-deposited Fe_2CoSn film, K_{eff} was found to be 3.2×10^6 erg/cc at 5 K and 3.0×10^6 erg/cc

at 300 K, and the corresponding values for the heat treated film were 9.3×10^6 erg/cc and 5.2×10^6 erg/cc, respectively. Since there are no prior reports on K_{eff} values of Fe_2CoSn alloy in the literature, the obtained values could only be compared with those reported for other Fe and Co based HA nanoparticles. These include Co_2FeGa (2.99 - 10.2×10^6 erg/cc [XUYY2018]; 7.5 - 9.0×10^6 erg/cc [NEHL2019]; 2.93 - 4.87×10^6 erg/cc [SRIV2023a]), Fe_2CoGa (5.68 - 8.62×10^6 erg/cc) [SRIV2022], and Fe_2CoAl (8.06 - 10.24×10^6 erg/cc) [SRIV2023b]. A decrement in both the H_c and K_{eff} at higher temperatures observed for both the Fe_2CoSn films is expected because of the breaking of the magnetic alignments by the disruption caused by the thermal energy, facilitating easier reorientation of the magnetic domains along the direction of the magnetic field [PATH2023]. The decrement of H_c with increasing temperature follows Kneller's law [KNEL1963] for the temperature dependence of H_c.

Thermomagnetization curve of heat treated Fe_2CoSn film, recorded under an applied field of 500 Oe, is shown in Figure 7.07. It is evident from the inset in Figure 7.07 that the Fe_2CoSn film exhibits a high T_C of 983 K. T_C of Fe_2CoSn film can be compared with those reported for Fe_2CoAl (830 - 990 K) [AHMA2021, LIYK2017, SAIT2018] and Fe_2CoGe (925 K) HA [GASI2013] to understand the role of the Z element in the Fe_2CoZ alloy [PATH2023].

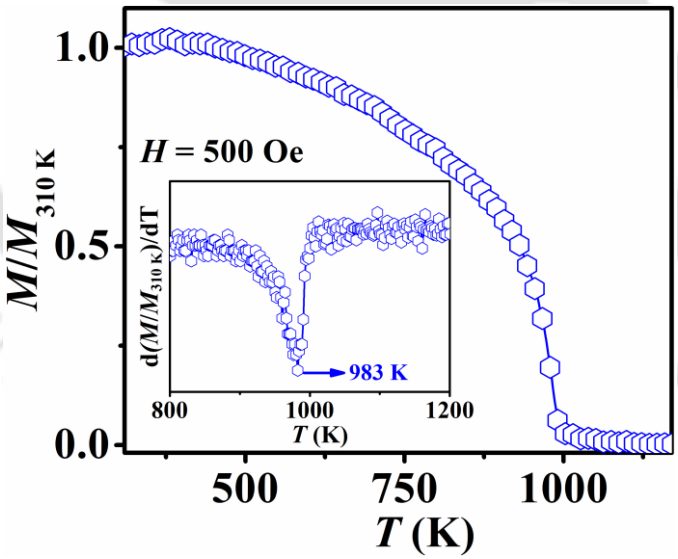

Figure 7.07. *M-T* curve of heat treated Fe_2CoSn film recorded with an applied magnetic field of 500 Oe. The inset depicts the differential of the magnetization curve plotted to locate the T_C.

To explore the nature of minority DOS near E_F and to estimate the M_t of Fe_2CoSn alloy, *ab initio* calculations were performed, which are discussed in the next section of this chapter.

7.5. Density of electronic states and magnetic moment of Fe_2CoSn alloy

A Fe_2CoSn supercell consisting of 16 atoms (8 Fe, 4 Co, and 4 Sn) was used in the *ab initio* calculations. Ideally, the atoms in the unit cell occupy the designated Wyckoff position of the inverse HA structure, *i.e.* Sn (0, 0, 0) 4*a*, Co (¼, ¼, ¼) 4*c*, Fe (½, ½, ½) 4*b* and Fe (¾, ¾, ¾) 4*d*, respectively [MATS2017]. The lattice constant obtained from Rietveld refined XRD data was used in the calculations. The detailed methodology followed in the *ab initio* calculations are discussed in section 2.3 of Chapter 2. Previous *ab initio* studies by Faleev *et al.* [FALE2017] and Matsushita *et al.* [MATS2017] on the Fe_2CoSn alloy, based on the GGA scheme, primarily focused on evaluating the stability of the inverse cubic *X*-type structure and estimating the lattice constant and magnetic moment. Khan *et al.* [KHAN2018] investigated the total and partial DOS for the energetically less favourable $L2_1$-type structure and reported the absence of half-metallicity, attributing it to the presence of Fe 3*d* states at the at E_F. However, DOS calculations for Fe_2CoSn alloy in its stable *X*-type structure have not yet been reported. Moreover, a comprehensive analysis of *d*-orbital hybridizations and the role of electron correlation effects in this strongly correlated system remains unexplored. To address these gaps in the literature, *ab initio* calculations based on the GGA + *U* approach were performed on Fe_2CoSn alloy, using the *X*-type unit cell and the experimentally determined lattice constant value to gain deeper insight into its electronic structure. Figure 7.08 presents the total DOS of Fe_2CoSn alloy. The figure shows that the valence band has contributions from both majority and minority states, whereas the conduction band has main contribution from minority states. The non-zero minority DOS at E_F classifies Fe_2CoSn as non-half-metallic. However, one can notice from Figure 7.08 that E_F resides in the low DOS region in both spin channels, which indicates the higher stability of this compound [SRIV2022, PATH2023]. Figure 7.08(a) portrays the presence of a full energy gap ~1.39 eV below E_F in the valence band and a pseudo gap (0.85 states/eV) at E_F in the minority spin band for U = 0.0 eV. As the U value is increased, the pseudo gap starts to shift toward the conduction band, and the full minority energy gap shifts toward E_F for U values up to 2.0 eV (Figure 7.08 (b - e)). At U = 2.0 eV, the full minority gap is situated ~1.10 eV below E_F in the valence band (Figure 7.08 (e)).

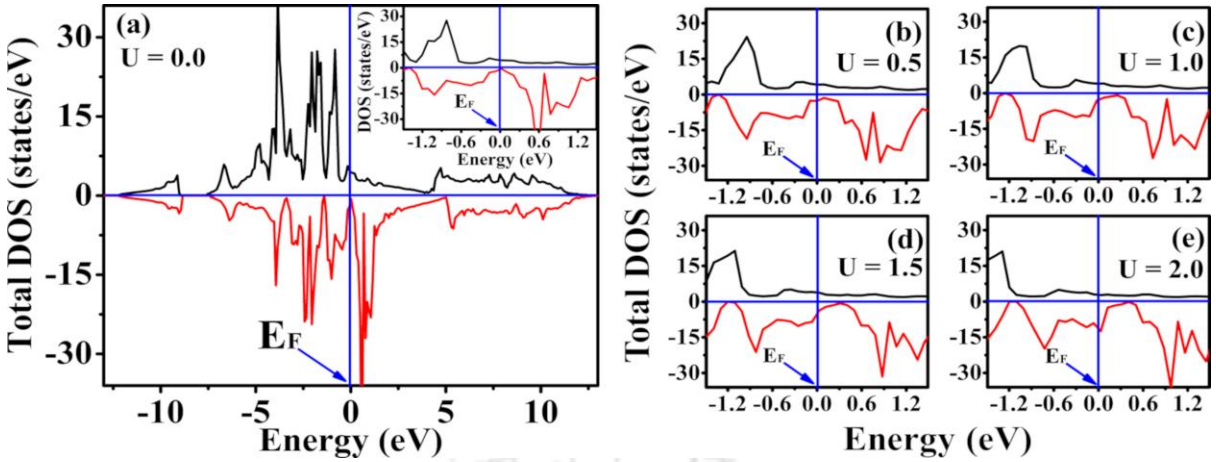

Figure 7.08. (a - e) total DOS *versus* energy plot of Fe_2CoSn alloy near E_F calculated using *X*-type unit cell with U = 0.0 - 2.0 eV. In all the figures, E_F is taken to be at 0.0 eV.

Figure 7.09 (a - e) present the partial DOS of Fe_2CoSn HA for U values ranging between 0.0 to 2.0 eV. When U = 0.0 eV (Figure 7.09 (a)), the minority spin states near E_F arising from Fe, Co, and Sn are very small, resulting in the formation of a pseudo gap at E_F. As the U value increases from 0.5 to 2.0 eV, the pseudo gap gradually shifts towards the conduction band, leading to an increase in the minority states at E_F. These states primarily originate from Co and Fe(II) atoms, with negligible contributions from Fe(I) and Sn, as shown in Figures 7.09 (b - e). These factors ultimately contribute to the loss of half-metallicity in this compound.

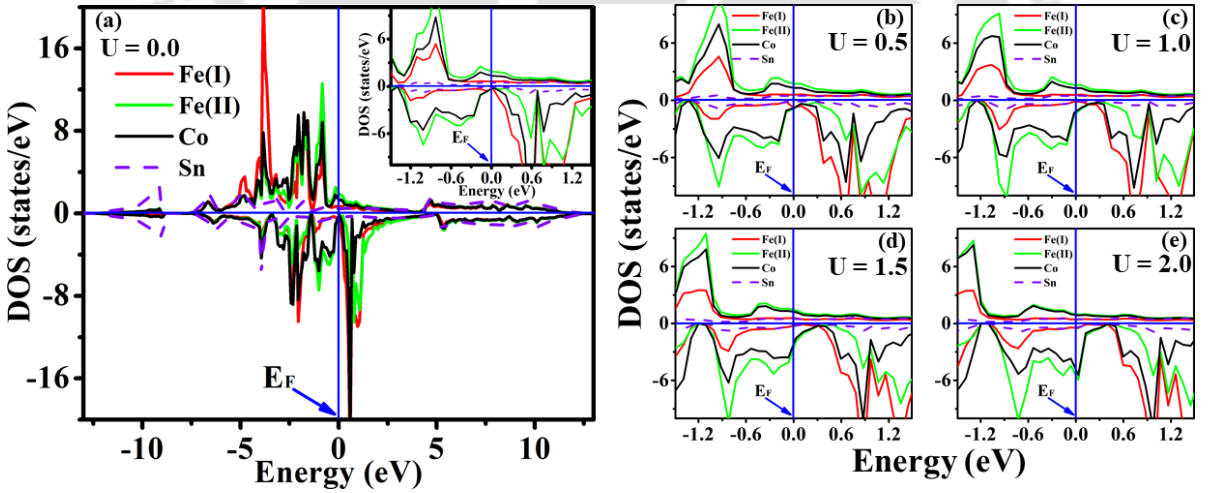

Figure 7.09. (a - e) DOS *versus* energy plot of Fe (I), Fe(II), Co and Sn in Fe_2CoSn alloy near E_F calculated using *X*-type unit cell with U = 0.0 - 2.0 eV. In all the figures, E_F is taken to be at 0.0 eV.

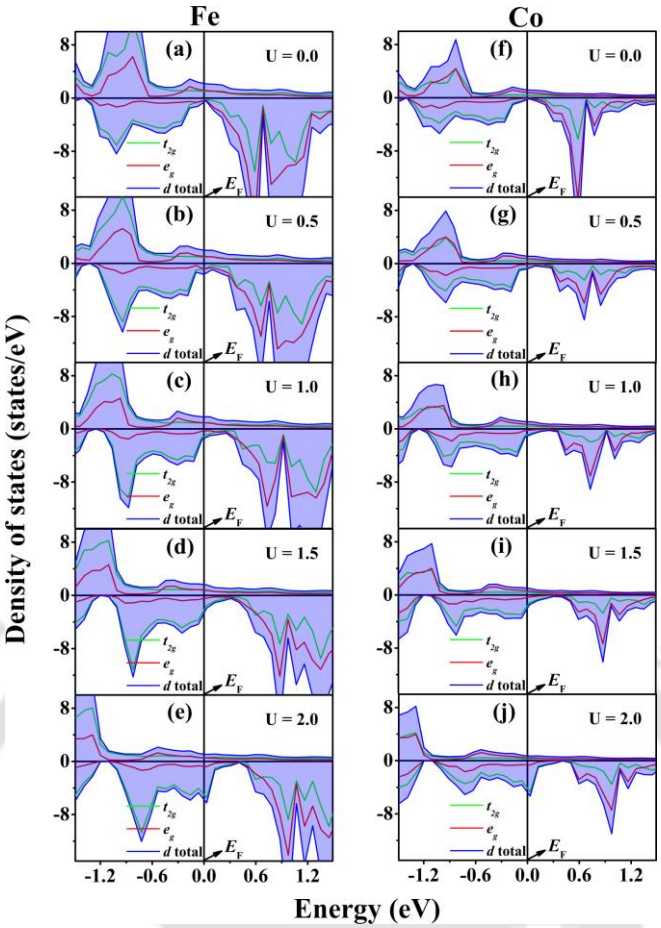

Figure 7.10. Projected partial DOS of *d*-orbital with e_g and t_{2g} orbitals of Fe with U = (a) 0.0, (b) 0.5, (c) 1.0, (d) 1.5, and (e) 2.0 eV, and Co with (f) U = 0.0, (g) U = 0.5, (h) U = 1.0, (i) U = 1.5, (j) U = 2.0 eV. In all the figures, E_F is taken to be at 0.0 eV.

Figure 7.10 (a - j) portray the partial *d* orbitals DOS due to doubly degenerate t_{2g} and triply degnerate e_g of Fe and Co as a function of U parameter near E_F, It is evident from Figure 7.10 (a) (U = 0.0 eV) that contributions to states at E_F in the minority spin channel from both t_{2g} and e_g states of Fe and Co are very small, which leads to the formation of a pseudo energy gap. As the U value is increased from 0.0 eV, E_F starts to shift towards the valence band, thereby increasing the t_{2g} states at E_F in the minority spin channel of Fe and Co. This rapid enhancement of t_{2g} states increases the total DOS in the minority ($D_\downarrow$) channel at E_F. At the same time, both Fe and Co, e_g and t_{2g} states in the majority channel start to decrease upon introduction of U, which in turn decreases the total DOS in the majority ($D_\uparrow$) channel at E_F. The P value calculated for U = 0.0 eV using eq. (1.06) was found to be 65 %. As discussed earlier, increasing the value of U results in a decrease in $D_\uparrow$ and a simultaneous increase in $D_\downarrow$. This leads to a reduction in P for U values up to 1.0 eV, beyond which P begins to increase, as

summarized in Table 7.01 (trend shown in Figure 7.11). These observations indicate that the *U* parameter has a significant influence on the *P* of Fe_2CoSn alloy. It should be remembered that the *ab initio* calculations performed in the present study are mainly applicable to bulk Fe_2CoSn alloy with a fully ordered *X*-type structure at 0 K. Any reduction in dimensions of the bulk alloy, say., to 2-d, 1-d, 0-d, can change the state of half-metallicity and hence *P* for the alloy as observed by Galdun *et al.* [GALD2020]. They observed an enhancement in the experimentally determined *P* for the 1-d Co_2FeSn alloy as compared to its bulk counterpart. Thus, there is a possibility for realizing higher *P* in nanogranular Fe_2CoSn films.

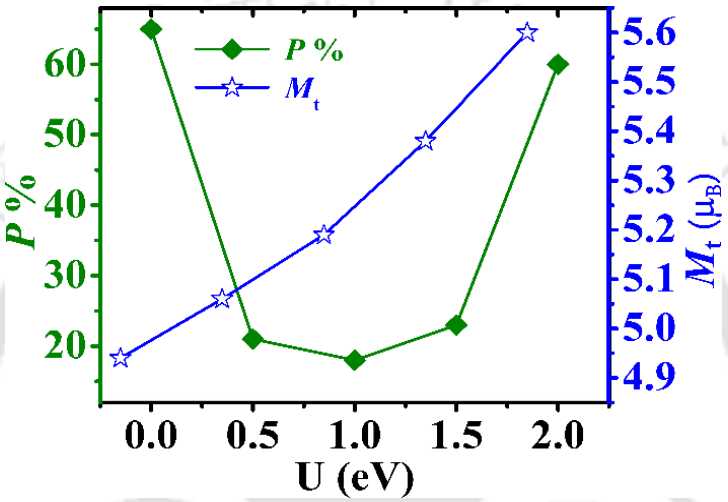

Figure 7.11. Variation of *P* and M_t with different *U* values for Fe_2CoSn alloy.

Table 7.01. Calculated total and atom-resolved magnetic moments and electronic DOS at E_F of Fe_2CoSn HA for different values of *U*.

U (eV)	M_t (μ_B/f.u.)	Atomic Moment (μ_B/f.u.)				$D_\uparrow(E_F)$ (States/eV)	$D_\downarrow(E_F)$ (States/eV)	P(%)
		Fe (I)	Fe (II)	Co	Sn			
0.0	4.94	2.62	1.50	0.92	-0.10	4.43	-0.85	65
0.5	5.06	2.69	1.57	0.92	-0.12	4.22	-2.34	21
1.0	5.19	2.74	1.66	0.93	-0.14	4.15	-2.58	18
1.5	5.38	2.80	1.78	0.96	-0.16	3.82	-5.52	23
2.0	5.60	2.86	1.91	1.00	-0.17	2.78	-11.35	60

The theoretically estimated M_t of Fe_2CoSn alloy varies from 4.94 - 5.60 μ_B/f.u. upon increasing U from 0.0 to 2.0 eV as listed in Table 7.01 (also see Figure 7.11). These values are close to the M_t values reported in the literature [FALE2017, MATS2017]. In the *X*-type structure, both Fe (I) (Wyckoff position (½ ½ ½)) and Fe (II) (Wyckoff position (¾ ¾ ¾)) have non-identical environments. Hence, the M_t value of Fe(I) and Fe(II) atoms are different as shown in Table 7.01. It is clear from Table 7.01 that Fe (I) possesses a higher M_t value compared to Fe (II) [PATH2023]. The reason for this discrepancy in the M_t of both the Fe atoms lies in their specific atomic positions and the resulting magnetic interactions. Here, Fe (I), positioned at (½ ½ ½), will be surrounded by 4 Co atoms at (¼ ¼ ¼) and 4 Fe (II) atoms at (¾ ¾ ¾). Thus, Fe (I) with only Co and Fe as its nearest neighbors will experience higher magnetic interaction, resulting in its higher spin magnetic moment [PATH2023]. On the other hand, Fe (II), being positioned at (¾ ¾ ¾), will be surrounded by 4 Sn atoms at (0 0 0) and 4 Fe (I) atoms at (½ ½ ½) as its nearest neighbourhood. Thus, Fe (II) will experience less magnetic interaction as it has only Fe at one of its nearest Wyckoff sites and non-magnetic Sn at the other nearest Wyckoff site, resulting in a lower M_t value [PATH2023].

7.6. Summary

The combined experimental and theoretical investigations on the structural and magnetic properties of electrodeposited Fe_2CoSn HA films yield the following results:

- A highly ordered 320 nm thick *X*-type structured Fe_2CoSn HA film with granular morphology has been synthesized on a low-cost polycrystalline Cu substrate by the electrodeposition route.
- The electrodeposited Fe_2CoSn films exhibit soft ferromagnetic behaviour with high M_s (4.98 μ_B/f.u. at 5 K), elevated T_C (983 K), and a high K_{eff} (9.3×10^6 erg/cc at 5 K). M_s observed for the heat treated film is the highest reported to date for this compound (in film form) and is closest to its theoretical value.
- DOS calculations performed using the GGA+*U* approach offer deeper insights into the minority DOS near E_F and the variation of *P* value with the *U* parameter.
- The combination of high M_s, elevated T_C, large K_{eff}, and the presence of a minority pseudo gap at E_F makes the Fe_2CoSn HA a promising candidate for various nanomagnetic applications.

Apart from demonstrating a simple, economical, and non-equilibrium electrodeposition route for the synthesis of stoichiometric Fe_2CoSn alloy films with high crystalline ordering, this study highlights the superior magnetic properties of the prepared films.

Chapter 8

Summary and scope for future work

This chapter summarizes the key findings and conclusions related to the compositional, structural, morphological, magnetic, electronic, and electrical properties of electrodeposited Co and Fe based Heusler alloy films. The key outcomes of the investigations are presented, along with potential directions for future research.

8.1. Summary of the key results

This thesis has described the successful synthesis of stoichiometric Co_2FeSn, off-stoichiometric Co-Fe-Sn, stoichiometric Fe_2CoSn, and Co-Fe-Cr-Sn quaternary Heusler alloys in single phase without any impurity phase in thin film form using a non-equilibrium electrodeposition technique. The significance of this work is apparent since it is difficult to prepare these alloys in pure single phase using conventional alloy preparation techniques like arc-melting. The single-phase polycrystalline alloy films with excellent control on their composition were deposited on polycrystalline Cu substrates using this cost-effective technique. The as-deposited films, which exhibited poor crystallinity, were annealed at 550 °C for 1 hour under vacuum (~10^{-3} Pa) to achieve well-crystallized and ordered Heusler alloy structure. The formation of highly ordered $L2_1$ or *X*-type Heusler alloy structure was confirmed by structural analysis involving powder X-ray and electron diffraction data and Rietveld refinement technique. *Ab initio* calculations have been extensively used to predict the atomic configurations in these alloys, validate the structural data and infer the role of atomic defects in these alloys with a complex crystal structure. EDS data confirmed that the composition of the films closely matched the target compositions, while morphological studies revealed a granular morphology across all the films. To explore the half-metallic character in Co and Fe based Heusler alloys, the nature of the minority spin gap near E_F was investigated by *ab initio* calculations. Isothermal magnetic measurements revealed the soft ferromagnetic behaviour in all the electrodeposited films. The dependence of M_s, H_c, T_C, and K_{eff} on the alloy composition and film thickness has been systematically examined in Co-Fe-Sn alloy films. Additionally, the itinerant and half-metallic ferromagnetic nature of the synthesized alloy film samples were

validated by calculating the Rhodes-Wohlfarth ratio using temperature dependent magnetic data. To further support the theoretical predictions of half-metallicity, temperature-dependent DC electrical resistivity measurements have also been conducted.

Electrodeposited stoichiometric Co_2FeSn alloy film exhibits the highest M_s (5.18 μ_B/f.u. at 5 K) and T_C (1123 K) as revealed by comparing with published literature. *Ab initio* calculations performed using the GGA + *U* approach reveal the presence of the minority spin gap near E_F (~0.05 eV below E_F) and its variation as a function of *U* in this compound. The capability to obtain $L2_1$-type Co_2FeSn films in the thickness range of 320 nm to 1400 nm by merely varying t_{dep} while keeping all other deposition parameters and electrolyte concentration unchanged is an interesting outcome which is of technological importance. The electrodeposited films exhibited high M_s ranging from 5.08 to 5.18 μ_B/f.u. at 5 K, an elevated T_C between 995 K and 1123 K, and high K_{eff} in the range of 5.7 to 6.4×10^6 erg/cc at 5 K. The combination of high M_s, elevated T_C, and large K_{eff} in the Co_2FeSn alloy films, along with a small decrement in magnetic moment upon scaling down the thickness from micrometer to the nanometer scale, making them a promising material for various micro and nano magnetic applications. Following the investigation of stoichiometric Co_2FeSn alloy films, a composition dependent study was conducted on Co-Fe-Sn alloys by varying the Co concentration from ~48.4 to 53.1 at.% and Sn concentration from ~29.8 to 25.0 at.%, while keeping the Fe concentration constant. This was aimed at tuning the position of the minority spin gap, lying at ~0.05 eV below E_F in the stoichiometric Co_2FeSn alloy. Structural analysis confirmed the formation of highly ordered $L2_1$-type structure in all the off-stoichiometric films. Isothermal magnetic measurements revealed soft ferromagnetic behaviour, characterized by high M_s ranging from 4.58 to 5.30 μ_B/f.u. at 5 K, elevated T_C between 1084 K and 1102 K, and high K_{eff} in the range of 6.6 to 8.1×10^6 erg/cc at 5 K. *Ab initio* studies revealed that the minority spin gap lies just below E_F in $Co_{48.4}Fe_{21.8}Sn_{29.8}$ and $Co_{51.6}Fe_{21.8}Sn_{26.6}$ alloys, whereas the minority spin gap lies at E_F in the case of $Co_{53.1}Fe_{21.9}Sn_{25.0}$ alloy. This study highlights the strategy of tuning the minority gap towards E_F through compositional adjustment in Co-Fe-Sn alloys. The Rhodes-Wohlfarth ratio indicates itinerant ferromagnetic behaviour in $Co_{48.5}Fe_{22.8}Sn_{28.7}$ and $Co_{51.7}Fe_{21.6}Sn_{26.7}$ films, while the $Co_{53.8}Fe_{20.6}Sn_{25.6}$ film exhibits the characteristics of a half-metallic ferromagnet. Furthermore, low temperature DC electrical resistivity measurements highlighted exponential suppression of spin-flip scattering in $Co_{53.8}Fe_{20.6}Sn_{25.6}$ alloy film apart from revealing a large spin energy gap $\Delta(E_g)$ value of 104.3 K (9.0 meV), confirming its half-metallic nature. These findings underscore the potential of compositionally tuned Co-Fe-Sn

alloy films to facilitate a transition from non-half-metallic to fully half-metallic behaviour, paving the way for their application in spintronic devices. The stoichiometric Co_2FeSn alloy exhibits non-half-metallic behaviour due to the presence of additional valence electrons in Fe compared to Cr or Mn, which leads to the emergence of minority spin states at E_F, thereby disrupting its half-metallicity. One approach to suppress these minority states at E_F is through compositional tuning as demonstrated above. An alternative strategy involves introducing a fourth element with lower valency into the Co-Fe-Sn system in the place of Fe, to shift the minority spin band gap toward E_F, thus restoring half-metallicity. As proof of this hypothesis, half-metallicity was achieved in a non-half-metallic $Co_{48.4}Fe_{21.9}Sn_{29.7}$ alloy by partially substituting Fe with Cr. Electrodeposited $Co_{47.9}Fe_{21.7}Sn_{30.4}$ and $Co_{48.3}Fe_{19.3}Cr_{3.1}Sn_{29.3}$ alloy films exhibit $L2_1$-type ordered structure. Both alloy films portray soft ferromagnetic behaviour characterized by high M_s of 4.52 μ_B/f.u. for $Co_{47.9}Fe_{21.7}Sn_{30.4}$ and 4.48 μ_B/f.u. for $Co_{48.3}Fe_{19.3}Cr_{3.1}Sn_{29.3}$ at 5 K and elevated K_{eff} in the range of 3.0 to 5.8×10^6 erg/cc at 5 K. Low temperature DC electrical resistivity studies conducted on $Co_{48.3}Fe_{19.3}Cr_{3.1}Sn_{29.3}$ alloy film revealed an exponential suppression of electron-magnon scattering, characterized by high $\Delta(E_g)$ value of 82.1 K (7.1 meV), which supports the half-metallicity predicted by *ab initio* calculations. Thus, a small (~3.1 at.%) amount of substitution of low valent Cr for Fe atoms induces half-metallicity in the non-half-metallic $Co_{48.4}Fe_{21.9}Sn_{29.7}$ Heusler alloy by effectively suppressing the minority DOS at E_F without causing significant variation in magnetic properties. In addition to experimentally validating the theoretically predicted half-metallicity in $Co_{48.3}Fe_{19.3}Cr_{3.1}Sn_{29.3}$ alloy, this study provides a cost-effective and facile methodology to synthesize quaternary alloy films by electrodeposition route. After detailed investigations on Co-Fe-Sn alloys, another promising alloy film with the same constituent elements, *i.e.* Fe_2CoSn, was explored. Since this alloy has the same constituents as Co-Fe-Sn, its synthesis *via* conventional techniques is difficult. Therefore, a highly ordered 320 nm thick *X*-type structured Fe_2CoSn HA film with granular morphology was synthesized on low-cost polycrystalline Cu substrate by the electrodeposition route. The electrodeposited Fe_2CoSn films exhibit soft ferromagnetic behaviour with high M_s (4.98 μ_B/f.u. at 5 K), elevated T_C (983 K), and a high K_{eff} (9.3×10^6 erg/cc at 5 K). M_s observed for the heat treated film is the highest reported to date for this compound and is closest to its theoretical value. DOS calculations performed using the GGA+*U* approach offer deeper insights into the minority DOS near E_F value with the *U* parameter. The combination of high M_s, elevated T_C, large K_{eff}, and the presence of a minority pseudo gap at E_F makes the Fe_2CoSn alloy film a promising

candidate for various nanomagnetic applications. Apart from demonstrating a simple, economical, and non-equilibrium electrodeposition route for the synthesis of stoichiometric Fe_2CoSn alloy films with high crystalline ordering, this study also highlights the superior magnetic properties of the prepared films. Hence, the systematic study on electrodeposited stoichiometric Co_2FeSn, off-stoichiometric Co-Fe-Sn and stoichiometric Fe_2CoSn film, along with the quaternary Co-Fe-Cr-Sn film, showcases the path for developing new and novel Heusler alloy films which are difficult to prepare *via* conventional techniques.

8.2. Scope for future work

As discussed in Chapter 1, Heusler alloys have garnered significant interest due to their potential to exhibit a wide range of exceptional properties, including half-metallicity, spin-gapless semiconducting behaviour, shape memory effect, magnetocaloric effect, thermoelectricity, and superconductivity. Despite their potential, many Heusler alloys have remained unexplored because of thermodynamic instability, which limits their synthesis through conventional alloy preparation techniques. Electrodeposition offers a promising and cost-effective alternative for fabricating non-equilibrium alloys in film form, enabling the realization of stochiometric and off-stoichiometric alloy compositions. Such alloys can exhibit properties, including high P, elevated M_s, large K_{eff}, and high T_C. The present study demonstrates several enhanced features of electrodeposited ternary and quaternary Heusler films, including high M_s, elevated T_C, large K_{eff}, low H_c, and substantial P, highlighting their suitability for high temperature magnetic and spintronic applications. Furthermore, the improved structural and magnetic characteristics observed in these electrodeposited films open new avenues for exploration of multicomponent alloys such as quaternary, quinary, and senary using a non-equilibrium, low-cost electrodeposition route. Apart from magnetic applications, this approach also offers opportunities for developing multicomponent alloys such as high entropy alloys for corrosion resistance, and electrocatalytic performance. There is also ample scope for adapting or modifying the electrodeposition technique, such as exploring other substrates in the place of Cu, using non-aqueous electrolytes, etc., which can expand the versatility of this technique.

References

[AHMA2021] Ahmad A, Mitra S, Srivastava S. K, Das, A. K, Structural, magnetic, and magnetocaloric properties of Fe_2CoAl Heusler nanoalloy., J. Magn. Magn. Mater., **540**, 168449 (2021).

[ANDR1997] Andreev S. V, Bartashevich M. I, Pushkarsky V. I, Maltsev V. N, Pamyatnykh, L. A, Tarasov E. N, Kudrevatykh N. V, Goto T, Law of approach to saturation in highly anisotropic ferromagnets application to Nd-Fe-B melt-spun ribbons., J. Alloys Compd., **260**, 196 (1997).

[ARAV2022] Aravindan V, Rajarajan A. K, Vijayanarayanan V, Mahendran M, First-principles calculations on novel Co-based Equiatomic Quaternary Heusler Alloys for Spintronics., MAT SCI SEMICON PROC., **150**, 106909 (2022).

[BAIZ2013] Bai Z, Shen L, Han G, Feng Y. P, Data storage: review of Heusler compounds., Spin, **2**, 1230006 (2012).

[BHAT2025] Bhat M. M, Alagarsamy P, Srinivasan A, Effect of Ti substitution for Co on structural, magnetic, and electronic properties of Co_2FeAl Heusler alloy., Intermetallics., **182**, 108783 (2025).

[BISW2024] Biswas S, Alagarsamy P, Srinivasan A, Influence of atomic substitution on the structural stability and half-metallicity of $Fe_{2-x}Cr_xCoSi$ (x = 0 to1) alloys., J. Magn. Magn. Mater., **612**, 172648 (2024).

[BOMB2013] Bombor D, Blum C. G. F, Volkonskiy O, Rodan S, Wurmehl S, Hess C, Büchner B, Half-metallic ferromagnetism with unexpectedly small spin splitting in the Heusler Compound Co_2FeSi. Phys. Rev. Lett., **110**, 066601 (2013).

[BRAD1934] Bradley A. J, Rodgers J. W, The Crystal structure of Heusler alloys., Proc. R. Soc. London., **144**, 340 (1934).

[BRAT1989] Bratsch S. G, Standard electrode potentials and temperature coefficients in water at 298.15 K., J. Phys. Chem. Ref. Data, **18**, 1,(1989).

[BREN1963] Brenner A, Electrodeposition of alloys: principles and practice., Academic Press, New York., **1**, 691 **(**1963).

[CARV2000] Rodriguez-Carvajal, J. FULLPROF-A program for Rietveld, profile matching and integrated intensities refinement of X-ray and/or neutron data, Laboratoire Leon Brillouin: CEA-Saclay, France., **5**, 1 (2000).

[CHAD2010] Chadov S, Qi X, Kübler J, Fecher G. H, Felser C, Zhang, S. C, Tunable multifunctional topological insulators in ternary Heusler compounds., Nat. Mat., **9**, 54 (2010).

[CHAT2023] Chatterjee S, Samanta S, Ghosh B, Mandal K, Half-metallic ferromagnetism and intrinsic anomalous Hall effect in the topological Heusler Compound Co_2MnGe. Phys. Rev. B., **108**, 205108 (2023).

[CHIS2007] Chisholm C, Kuzmann E, El-sharif M, Doyle O, Stichleutner S, Preparation and characterisation of electrodeposited amorphous Sn-Co-Fe ternary alloys., Appl. Surf. Sci., **253**, 4348 (2007).

[COEY2001] Coey J. M. D, Magnetism in future. J. Magn. Magn. Mater., **226**, 2107 (2001).

[CULL2009] Cullity B. D, Graham C. D, Introduction to magnetic materials., JOHN WILEY & SONS INC, USA., **2**, 537 (2009).

[CULL2014] Cullity B. D, Stock S. R, Elements of X-ray diffraction., Pearson education limited, Harlow., **3**, 656 (2014).

[DEKA2014] Deka B, Chakraborty D, Srinivasan A, Magnetic properties of $Co_2Fe(Ga_{1-x}Si_x)$ alloys., Phys. B., **448**, 173 (2014).

[DEKA2015] Deka B, Kundu A., Ghosh S., and Srinivasan A., Experimental and *ab initio* studies on sub-lattice ordering and magnetism in $Co_2Fe(Ge_{1-x}Si_x)$ alloys, J. Appl. Phys. 133906, **118** (2015).

[DEKA2016a] Deka B, Modak R, Paul P, Srinivasan A, Effect of atomic disorder on magnetization and half-metallic character of Cr_2CoGa alloy., J. Magn. Magn. Mater., **418**, 107 (2016).

[DEKA2016b] Deka B, Kundu A, Ghosh S, Srinivasan A, Effect of electron-electron correlation and site disorder on the magnetic moment and half-metallicity of $Co_2FeGa_{1-x}Si_x$ alloys., Mater. Chem. Phys., **177**, 564 (2016).

[DOBR2006] Dobrzański L. A, Significance of materials science for the future development of societies., J. Mater. Process. Technol., **175**, 133 (2006).

[DUYX2013] Du Y, Xu G. Z, Zhang X. M, Liu Z. Y, Yu S. Y, Liu E. K, Wang W. H, Wu G. H., Crossover of magnetoresistance in the zero-gap half-metallic Heusler alloy Fe_2CoSi., EPL., **103**, 37011 (2013).

[DUAN2013] Duan J, Kou X, Effect of Current Density on the Microstructure and Magnetic Properties of Electrodeposited Co_2FeSn Heusler Alloy., J. Electrochem. Soc., **160**, D471 (2013).

[DUBO2007] Dubowik J., Gościańska I., Szlaferek A., Kudryavtsev Y. V., Films of Heusler alloys, Mater. Sci. - Pol. **25**, 583 (2007).

[DUDA1998] Dudarev S. L, Botton G. A, Savrasov S. Y, Humphre C. J, Sutton A. P, Electron-energy-loss spectra and the structural stability of nickel oxide: An LSDA+U study, Phys. Rev. B., **57**, 1505 (1998).

[FAHN1978] Fahnle M, Kronmuller, The influence of spacially random magnetostatic, magnetocrystalline, magnetostrictive and exchange fluctuations on the law of approach to ferromagnetic saturation of amorphous ferromagnets., J. Magn. Magn. Mater., **8**, 149 (1978).

[FALE2017] Faleev S. V, Ferrante Y, Jeong J, Samant M. G, Jones B, Parkin S. S. P, Origin of the Tetragonal Ground State of Heusler Compounds., Phys. Rev. Appl., **7**, 034022 (2017).

[FELS2007] Felser C, Fecher G. H, Balke B, Spintronics: A challenge for materials science and solid-state chemistry., Angew. Chem. Int. Ed., **46**, 668 (2007).

[FELS2016] Felser C, Hirohata A, Heusler Alloys : Properties, Growth, Applications, Springer Series in Materials Science, London., **222**, 479 **(**2016).

[FONG2013] Fong C. Y, Pask J. E, Yang L. H, Half-metallic materials and their properties., Imperial College Press London., **2**, 289 (2013).

[FUJI1995] Fuji S, Ishida S, Asano S, A half-metallic band structure and Fe_2MnZ (Z = Al, Si, P)., J. Phys. Soc. Jpn., **64**, 185 (1995).

[FUJI2022] Fujiwara K, Shibata K, Nishimura S, Shiogai J, Tsukazaki A, L 21ordering of Co_2FeSn thin films promoted by high-temperature annealing. AIP Adv., **12**, 065030 (2022).

[GALA2002] Galanakis I, Dederichs P. H, Papanikolaou N, Slater-Pauling behavior and origin of the half-metallicity of the full-Heusler alloys., Phys. Rev. B., **66**, 174429 (2002).

[GALA2006] Galanakis I, Mavropoulos P, Dederichs P. H, Electronic structure and Slater-Pauling behaviour in half-metallic Heusler alloys calculated from first principles., J. Phys. D Appl. Phys., **39**, 765–775 (2006).

[GALD2020] Galdun L, Szabo P, Vega V, Barriga-Castro E. D, Mendoza-Reséndez R, Luna, C, Kovac J, Milkovic O, Varga R, Prida V. M, High spin polarization in Co_2FeSn Heusler nanowires for spintronics., ACS Appl. Nano Mater., **3**, 7438 (2020).

[GAOS2015] Gao S, Liu Y, Kou X, Effect of electrolyte pH and deposition time on the microstructure and magnetic properties of electrodeposited Fe_2CoSn Heusler alloy., Int. J. Electrochem. Sci., **10**, 8727 (2015).

[GASI2013] Gasi T, Ksenofontov V, Kiss J, Chadov S, Nayak A. K, Nicklas M, Winterlik J, Schwall M, Klaer P, Adler P, Felser C, Iron-based Heusler compounds Fe_2YZ: Comparison with theoretical predictions of the crystal structure and magnetic properties., Phys. Rev. B., **87**, 064411 (2013).

[GELL2013] Gellesch M, Dimitrakopoulou M, Scholz M, Blum C. G. F, Schulze M, Brink J. Van den, Hampel S, Wurmehl S, Buchner B, Facile Nanotube-Assisted Synthesis of Ternary Intermetallic Nanocrystals of the Ferromagnetic Heusler Phase Co_2FeGa., Cryst. Growth Des., **13**, 2707 (2013).

[GILL2009] Gilleben M, Dronskowski R, A combinatorial study of full Heusler alloys by first-principles computational methods., J. Comput. Chem., **30**, 1290 (2009).

[GOLU2009] Golub V, Reddy K. M, Chernenko V, Müllner P, Punnoose A, Ohtsuka M, Ferromagnetic resonance properties and anisotropy of Ni-Mn-Ga thin films of different thicknesses deposited on Si substrate., J. Appl. Phys., **105**, 07A942 (2009)

[GRIF1999] Griffiths D. J, Introduction to Electrodynamics, Prentice-Hall, Inc., New Jersey, **1**, 537 (1999).

[GROO1983] de Groot R. A, Mueller F. M, van Engen P. G, Buschow K. H. J, New class of materials: half-metallic ferromagnets., Phys. Rev. Lett., **50**, 2024 (1983).

[HEYA2020] He Y, Fecher G. H, Fu C, Pan Y, Manna K, Kroder J, Jha A, Wang X, Hu Z, Agrestini S, Herrero-Martín J, Valvidares M, Skourski Y, Schnelle W, Stamenov P, Borrmann H, Tjeng L. H, Schaefer R, Parkin S. S. P, Felser C, A new highly anisotropic Rh-based Heusler compound for magnetic recording., Adv. Mater., **32**, 2004331(2020).

[HEUS1903] Heusler F, No Title, Verh Dtsch. Phys., Gellschaft., **5** 219 (1903).

[HEUS1934] O. Heusler, Kristallstruktur und ferromagnetismus der mangan-aluminium-kupferlegierungen., Ann. Phys. **411**, 155 (1934).

[HINT2019] Hinterleitner B, Knapp I, Poneder M, Shi Y, Müller H, Eguchi G, Eisenmenger-Sittner C, Stöger-Pollach M, Kakefuda Y, Kawamoto N, Guo Q, Baba T, Mori T, Ullah S, Chen X. Q, Bauer E, Thermoelectric performance of a metastable thin-film Heusler alloy., Nature, **576**, 85 (2019).

[HIRO2006] Hirohata A, Kikuchi M, Tezuka N, Inomata K, Claydon J. S, Xu Y. B, Lan G. van der, Heusler alloy/semiconductor hybrid structures., Curr Opin Solid State Mater Sci., **10**, 93 (2006).

[HUKU2023] Hu K, Xie R, Shen C, Peng H, Liu H, Zhang H, High-throughput design of Co-based magnetic Heusler compounds., Acta Mater., **259**, 119255 (2023).

[HUAN2015] Huang H-L, Tung J-C, Guo G-Y, Anomalous Hall effect and current spin polarization in Co_2FeX Heusler compounds (X = Al, Ga, In, Si, Ge, and Sn): A systematic *ab initio* study., Phys. Rev. B., **91**, 134409 (2015).

[HUMM2004] Hummel R. E, Understanding Materials Science, history, properties, applications., Springer-Verlag New York, LLC., **15**, 427 (1999).

[HUYN2015] Huynh L. T, Bonvicini S. N, Pinon A. C, Trudel S, Nanocrystalline alloys: Synthesis and characterization of non-stoichiometric Co_2FeAl nanocrystals., Can. J. Chem., **94,** 1 (2015)

[INIE2015] Iniewski K, High speed devices and circuits with THz Applications., CRC Press, London., **1**, 23 (2015).

[INIG1999] Iniguez B, Fjeldly T. A, Shur M. S, Thin-film transistor modelling., IJHSES., **9**, 703 (1999).

[JAGG1978] Jaggi N. K, Rao K. R. P. M, Grover A. K, Gupta L. C, Vijayarghavan R, Khoi, L. D, Mossbauer and NMR study of site preference, local environment and effects in Co_2FeGa & Fe_2CoGa ., North Holland Pub. Co., **4**, 402 (1978).

[JINZ1998] Jin Z. Q, Tang W, Zhang J. R, Qin H. X, Du Y. W, Effective magnetic anisotropy of nanocrystalline Nd-Fe-Ti-N hard magnetic alloys., Eur. Phys. J. B., **3**, 41 (1998).

[JOUR2014] Jourdan M, Minár J, Braun J, Kronenberg A, Chadov S, Balke B, Gloskovskii A, Kolbe M, Elmers H. J, Schönhense G, Ebert H, Felser C, Kläui M, Direct observation of half-metallicity in the Heusler compound Co_2MnSi., Nat. Commun., **5**, 1 (2014).

[KARI2020] Karim M. R, Panda D, Adhikari A, Sharangi P, Mandal P, Ghosh S, Bedanta S, Barman A, Sarkar I, Electrodeposited Heusler alloy films with enhanced magneto-optical property., Mater. Today Commun., **25**, 101678 (2020).

[KARI2021] Karim M. R, Adhikari A, Panda S. N, Sharangi P, Kayal S, Manna G, Kumar P. S. A, Bedanta S, Barman A, Sarkar I, Ultrafast spin dynamics of electrochemically grown Heusler alloy films. J. Phys. Chem. C., **125**, 10483 (2021).

[KARI2022a] Karim M. R, development of low dimensional cobalt- iron based Heusler alloys systems for magnetic and magneto-optical applications., INST, Punjab, india **1**, 125 (2022).

[KARI2022b] Karim M. R, Panda S. N, Barman A, Sarkar I, Strain and crystallite size controlled ordering of Heusler nanoparticles having high heating rate for magneto-thermal application., Nanotechnology., **33**, 235701(2022).

[KHAN2018] Khan S, Ahmad N, Ahmed N, Safeer A, Iqbal J, Han X. F, Structural, magnetic and transport properties of Fe-based full Heusler alloy Fe_2CoSn

nanowires prepared by template-based electrodeposition., J. Magn. Magn. Mater., **465**, 462 (2018).

[KHOS2009] Khosravizadeh S, Hashemifar S. J, Akbarzadeh H, First-principles study of the $Co_2FeSi(001)$ surface and $Co_2FeSi/GaAs(001)$ interface., Phys. Rev. B., **79**, 235203 (2009).

[KNEL1963] Kneller E. F, Luborsky F. E, Particle size dependence of coercivity and remanence of single-domain particles., J. Appl. Phys., **34**, 656 (1963).

[KOBA2004] Kobayashi K, Umetsu R. Y, Kainuma R, Ishida K, Oyamada T, Fujita A, Fukamichi K, Phase seperation and magnetic properties of half-metal-type $Co_2Cr_{1-x}Fe_xAl$ alloys., Appl. Phys. Lett., **85**, 4684 (2004).

[KOSH2022] Koshkid'ko Y. S, Dilmieva E. T, Kamantsev A. P, Cwik J, Rogacki K, Mashirov A. V, Khovaylo V. V, Mejia C. S, Zagrebin M. A, Sokolovskiy V. V, Buchelnikov, V. D, Ari-Gur P, Bhale P, Shavrov V. G, Koledov V. V, Magnetocaloric effect and magnetic phase diagram of Ni-Mn-Ga Heusler alloy in steady and pulsed magnetic fields., J. Alloys Compd., **904**, 164051 (2022).

[KREE1999] Kreese G, Joubert D, from ultrasoft pseudopotentials to the projector augmented-wave method., Phys. Rev. B., **59**, 1758 (1999).

[KUAN2008] Kuanr B. K, Maat S, Chandrashekariaih S, Veerakumar V, Camley R. E, Celinski Z, Determination of exchange and rotational anisotropies in IrMn/Fe(t)/IrMn exchange coupled structures using dynamic and static techniques: Application to microwave devices., J. Appl. Phys., **103**, 07C107 (2008).

[KURF2003] Kurfiß M, Anton R, Structural and magnetic properties of vapour deposited thin films of the Heusler alloy NiMnIn., J. Alloys Compd. **361**, 36 (2003).

[LITA2013] Li T, Duan J, Yang C, Kou X, Synthesis, microstructure and magnetic properties of Heusler Co_2FeSn nanoparticles., Micro Nano Lett., **8**, 143 (2013).

[LIPE2015] Li P, Kou X, Diffusion-assisted synthesis of Co_2FeSn Heusler nanoparticles and their magnetic properties., Chem. Lett., **44**, CL-150819 (2015).

[LIYK2017] Li Y, Kou X, Hou N, Synthesis, microstructure and magnetic properties of Fe_2CoAl nanofibers., Funct. Mater. Lett., **10**, 1750035 (2017).

[LINZ2020] Lin Z, Progress Review on Topological Properties of Heusler Materials., E3S Web Conf., **213**, 02016 (2020).

[LUHO2018] Lu H, Liu Y, Kou X, Communication-Electrodeposition, Microstructure and Magnetic Properties of Co_2FeSn Heusler Alloy Nanowires., J. Electrochem. Soc., **165**, D813 (2018).

[MAHA2023] Mahata D, Srivastava M, Srinivasan A, Synthesis and Characterization of Single Phase γ-$Co_{46-x}Ni_{22+x}Al_{32}$ (x = 0, 10, 20) Heusler Alloy Nanoparticles., IEEE Trans. Magn., **59**, 2500605 (2023).

[MAHA2024] Mahata D, Srinivasan A, Stabilization of various structural phases and magnetic properties of chemically synthesized Co-Ni-Ga nanoparticles., Materialia, **35**, 102116 (2024).

[MALA2016] Malaman B, Le Caër, G, Costa B. F. O, *B*2 long-range order in mechanically alloyed $Fe_{53.3-0.6x}Co_{46.7-0.4x}Sn_x$ ($2 \leq x \leq 26$) annealed at moderate temperatures. J. Mater. Sci., **51**, 5775 (2016).

[MARC2018] Marchenkov V. V, Perevozchikova Y. A, Kourov N. I, Irkhin V. Y, Eisterer M, Gao T, Peculiarities of the electronic transport in half-metallic Co-based Heusler alloys., J. Magn. Magn. Mater., **459**, 21 (2018).

[MARI2012] Mariappan R, Ponnuswamy V, Ragavendar M, Characterization of $CdS_{1-x}Se_x$ thin films by chemical bath deposition technique., Optik., **123,** 1196 (2012).

[MATS2017] Matsushita Y. I, Madjarova G, Dewhurst J. K, Shallcross S, Felser C, Sharma S, Gross E. K. U, Large magnetocrystalline anisotropy in tetragonally distorted Heuslers: A systematic study., J. Phys. D: Appl. Phys., **50**, 095002 (2017).

[MCCA2005] McCandless B. E., Glancing incidence X-Ray diffraction of polycrystalline thin films. Mater. Res. Soc. Symp. Proc., **865**, 75 (2005).

[MIUR2006] Miura Y, Shirai M, Nagao K, Ab initio study on stability of half-metallic Co-based full-Heusler alloys., J. Appl. Phys., **99**, 08J112 (2006).

[MODA2017] Modak R, Samantaray B, Mandal P, Srinivasan A, Thickness dependent structural, magnetic and magneto-dynamic properties of Mn rich Ni-Mn-Sn Films., J. Alloys Compd., **692**, 529 (2017).

[MODA2018a] Modak R, Structural , magneto-static and magneto- dynamic properties of Ni- Mn-Z and Ni-Mn-X-Z (X = Cu , Fe , Co ; Z = Sn , In) thin films., IIT Guwahati India., **1**, 175 (2018).

[MODA2018b] Modak R, Raja M. M, Srinivasan A, Enhanced magneto-caloric effect upon Co substitution in Ni-Mn-Sn thin films., J. Magn. Magn. Mater., **448**, 146 (2018).

[MONK1976] Monkhorst H. J, Pack J. D, Special points for Brillouin-zone integrations., Phys. Rev. B., **13**, 5188 (1976).

[NASI2017] Nasirpouri F, Electrodeposition of nanostructured materials., Springer International Publishing, Switzerland., **62**, 75 (2017).

[NEHL2019] Nehla P, Ulrich C, Dhaka R. S, Investigation of the structural, electronic, transport and magnetic properties of Co_2FeGa Heusler alloy nanoparticles., J. Alloys Compd., **776**, 379 (2019).

[NEPA2020] Nepal S, Dhakal R, Galanakis I, Ab initio study of the half-metallic full-Heusler compounds Co_2ZAl [Z= Sc, Ti, V, Cr, Mn, Fe]; the role of electronic correlations, Mater. Today Commun., **25**, 101498, (2020).

[NOKY2018] Noky J, Gooth J, Felser C, Sun Y, Characterization of topological band structures away from the Fermi level by the anomalous Nernst effect., Phys. Rev. B., **98**, 241106R (2018).

[OHRI1992] Ohring M, Material science of thin films., Academic Press London., **1**, 689 (1992).

[OKE2022] Oke J. A, Jen T. C, Atomic layer deposition and other thin film deposition techniques: from principles to film properties., J. Mater. Res. Technol., **21**, 2481 (2022)

[OTTO1989] Otto M. J, Woerden van R. A. M, Valk van der P. J, Wijngaard J, Bruggen van C. F, Hass C, Buschow K. H. J, Half-metallic ferromagnets: I. Structure

and magnetic properties of NiMnSb and related inter-metallic compounds., **1**, 2341 (1989).

[OUAR2013] Ouardi S, Fecher G. H, Felser C, Kübler J, Realization of spin gapless semiconductors: The Heusler compound Mn_2CoAl. Phys. Rev. Lett., **110**, 100401 (2013).

[OZDO2007] Özdoğan K, Aktaş B, Galanakis I, Şaşioğlu E, Influence of mixing the low-valent transition metal atoms (Y, Y* = Cr, Mn, Fe) on the properties of the quaternary Co2[$Y_{1-X}Y^*_X$]Z (Z=Al, Ga, Si, Ge, or Sn) Heusler compounds., J. Appl. Phys., **101**, 073910 (2007).

[PATH2022] Pathak P, Bisht G. S, Srinivasan A, Enhanced Magnetic Properties of Electrodeposited Co_2FeSn film with high structural order., J. Electrochem. Soc., **169**, 092508 (2022).

[PATH2023] Pathak P, Srivastava M, Bisht G. S, Srinivasan A, Electrodeposited Fe_2CoSn thin film with enhanced structural and magnetic properties., J. Electrochem. Soc., **170**, 122504 (2023).

[PATH2024] Pathak P, Bisht G. S, Srinivasan A, Thickness dependence of structural and magnetic properties of electrodeposited Co_2FeSn films. Thin Solid Films, **795**, 140311 (2024).

[PATH2025] Pathak P, Srinivasan A, Tuning of magnetic properties and half-metallicity of electrodeposited Co-Fe-Sn Heusler alloy films by varying elemental composition. Materialia, **42**, 102487 (2025).

[PATR2019] Patra N, Prajapat C. L, Babu P. D, Rai S, Kumar S, Jha S. N, Bhattacharyya D, Pulsed laser deposited Co_2FeSi Heusler alloy thin films: Effect of different thermal growth processes., J. Alloys Compd., **804**, 470 (2019).

[PERD1996] Perdew J. P., Burke K., and Ernzerhof M., Generalized gradient approximation made simple, Phys. Rev. Lett. 3865, **77** (1996).

[QIAO2013] Qiao S, Gao H, Nie S, Zhao J, Zhang X, The magnetic switching process in MBE-grown Co_2MnAl Heusler alloy film., Solid State Commun., **163**, 33 (2013).

[SAIT2018] Saito T, Nishio-Hamane D, Magnetic and thermoelectric properties of melt-spun ribbons of Fe_2XAl (X = Co,Ni) Heusler compounds., J. Appl. Phys., **124**, 075105 (2018).

[SCHE2016] Scheunert G, Heinonen O, Hardeman R, Lapicki A, Gubbins M, A review of high magnetic moment thin films for microscale and nanotechnology applications., Appl. Phys. Rev., **3**, 011301, (2016).

[SHAK2021] Shakil M, Arshad H, Aziz S, Gillani S. S. A, Rizwan M, Zafar M, Determination of phase stability, half metallicity, mechanical and thermal behavior of Fe based quaternary Heusler alloys., J. Alloys Compd., **856**, 157370 (2021).

[SHAM2019] Shambhu K. C, Mahat R, Regmi S, Mukherjee A, Padhan P, Datta R, Butler W. H, Gupta A, LeClair P, Tunable properties and potential half-metallicity in $(Co_{2-x}Ti_x)FeGe$ Heusler alloys: An experimental and theoretical investigation., Phys. Rev. Mater., **3**, 114406 (2019).

[SHEN2018] Sheng P, Wang B, Li R, Flexible magnetic thin films and devices., J. Semicond., **39**, 011006 (2018).

[SKAF2013] Skaftouros S, Özdoğan K, Şaşioğlu E, Galanakis I, Generalized Slater-Pauling rule for the inverse Heusler compounds., Phys. Rev. B., **87**, 024420 (2013).

[SRIV2022] Srivastava M, Sahariah M. B, Srinivasan A, Size-dependent properties of single domain Fe_2CoGa nanoparticles prepared by a facile template-less chemical route., J. Mater. Chem. C., **10**, 11946 (2022).

[SRIV2023a] Srivastava M, Bisht G. S, Srinivasan A, Single domain Co_2FeGa nanoparticles with high crystalline order synthesised by template-less chemical method., J. Alloys Compd., **949**, 169848 (2023).

[SRIV2023b] Srivastava M, Saha P, Srinivasan, Single-domain Fe_2CoAl nanoparticles and their crystallite size dependent properties., J. Phys. Chem. C., **127**, 1021 (2023).

[SRIV2024] Srivastava M, Saha P, Srinivasan A, Highly ordered single domain $Fe_{2-x}Co_{1+x}Ga$ ($0 \leq x \leq 1$) nanoparticles synthesized by a template-less chemical route., Mater. Res. Bull., **172**, 112659 (2024).

[SUHA2010] Suharyadi E, Hori T, Mibu K, Seto M, Kitao S, Mitsui T, Yoda Y, Nuclear resonant time spectra for ^{119}Sn in Co_2TiSn Heusler Alloy Films., J. Magn. Magn. Mater., **322**, 158 (2010).

[SUKE2014] Sukegawa H, Wen Z. C, Kasai S, Inomata K, Mitani S, Spin transfer torque switching and perpendicular magnetic anisotropy in full Heusler alloy Co_2FeAl-based tunnel junction., Spin., **4**, 1440023 (2014).

[SUZU2004] Suzuki R. O, Kyono T, Thermoelectric properties of Fe_2TiAl Heusler alloys., J. Alloys Compd., **377**, 38 (2004).

[TAKA2010] Takamura Y, Nakane R, Sugahara S, Quantitative analysis of atomic disorders in full-Heusler alloy thin films using x-ray diffraction with Co *K*α and Cu *K*α sources., **107**, 09B111 (2010).

[TANA2012] Tanaka M. A, Ishikawa Y, Wada Y, Hori S, Murata A, Horii S, Yamanishi Y, Mibu K, Kondou K, Ono T, Kasai S, Preparation of Co_2FeSn Heusler alloy films and magnetoresistance of Fe/MgO/Co_2FeSn magnetic tunnel junctions., Appl. Phys., **111**, 053902 (2012).

[TEIC2015] Teichert N, Boehnke A, Behler A, Weise B, Waske A, Hütten A, Exchange bias effect in martensitic epitaxial Ni-Mn-Sn thin films applied to pin CoFeB/MgO/CoFeB magnetic tunnel junctions., Appl. Phys. Lett., **106**, 192401 (2015).

[TICK1999] Tickle R., James R. D, Shield T, Wuttig M, Kokorin V. V, Ferromagnetic shape memory in the NiMnGa system. IEEE Trans. Magn., **35**, 430 (1999).

[VASP2025] VASP manual, https://www.vasp.at/wiki (2025)

[WATA2015] Watanabe N, Sano K, Tasugi N, Yamaguchi T, Yamamoto A, Ueno M, Sumiyoshi R, Arakawa T, Koiwa I, Preparation of Co_2FeSn Heusler alloys by electrodeposition method. APL Mater., **3**, 041804 (2015).

[WATT2000] Watts S. M, Wirth S, Molna´r S von, Evidence for two-band magnetotransport in half-metallic chromium dioxide., Phys. Rev. B., **61**, 9621 (2000).

[WEBS1973] Webster P. J, Ziebeck K. R. A, Magnetic and chemical order in Heusler alloys containing cobalt and titanium. J. Phys. Chem. Solids., **34**, 1647 (1973).

[WERN1983] Wernick J. H, Hull G. W, Geballe T. H, Bernardini J. E, Waszczak J. V, Superconductivity in ternary Heusler intermetallic compounds., Mater. Lett., **2**, 90 (1983).

[WURM2005] Wurmehl S, Fecher G. H, Kandpal H. C, Ksenofontov V, Felser C, Lin H. J, Investigation of Co_2FeSi: The Heusler compound with highest Curie temperature and magnetic moment and calculations., Phys. Rev. B., **88**, 184434 (2005).

[WURM2006] Wurmehl S, Fecher G. H, Kandpal H. C, Ksenofontov V, Felser C, Lin H. J, Investigation of Co_2FeSi: The Heusler compound with highest Curie temperature and magnetic moment., Appl. Phys. Lett., **88**, 032503 (2006).

[XUYY2018] Xu Y, Yang D, Luo Z, Wu F, Chen C, Liu M, Yi L, Piao H-G, Yu G, Fabrication and magnetic properties of structure-tunable Co_2FeGa-SiO_2 Heusler nanocompounds., AIP Adv., **8**, 055107 (2018).

[YINM2013] Yin M, Chen S, Nash P, Enthalpies of formation of selected Co_2YZ Heusler compounds., J. Alloys Compd., **577**, 49 (2013).

[YINM2015] Yin M, Nash P, Chen S, Enthalpies of formation of selected Fe_2YZ Heusler compounds., Intermetallics., **57**, 34 (2015).

[ZANG2015] Zangari G, Electrodeposition of alloys and compounds in the era of microelectronics and energy conversion technology., Coatings., **5**, 195 (2015).

[ZHAN2005] Zhang W, Jiko N, Mibu K, Yoshimura K, Effect of substitution of Mn with Fe or Cr in Heusler alloy of Co_2MnSn., J. Phys. Condens. Matter., **17**, 6653 (2005).

[ZHAN2008] Zhang S, Li L, Kumar A, Materials characterization Techniques. CRC Press, Taylor & Francis Group, Boca Raton., **1**, 319 (2008).

Publications/Presentations

List of publications from the thesis work:

[1] P. Pathak, G. S. Bisht, A. Srinivasan, Enhanced magnetic properties of electrodeposited Co_2FeSn film with high structural order, J. Electrochem. Soc. **169** (2022) 092508. https://doi.org/10.1149/1945-7111/ac8d76.

[2] P. Pathak, M. Srivastava, G. S. Bisht, A. Srinivasan, Electrodeposited Fe_2CoSn thin film with enhanced structural and magnetic properties, J. Electrochem. Soc. **170** (2023) 122504. https://doi.org/10.1149/1945-7111/ad155b.

[3] P. Pathak, G. S. Bisht, A. Srinivasan, Thickness dependence of structural and magnetic properties of electrodeposited Co_2FeSn films, Thin Solid Films **795** (2024)140311. https://doi.org/10.1016/j.tsf.2024.140311.

[4] P. Pathak, A. Srinivasan, Tuning of magnetic properties and half-metallicity of electrodeposited Co-Fe-Sn Heusler alloy films by varying elemental composition, Materilia **42** (2025) 102487. https://doi.org/10.1016/j.mtla.2025.102487.

[5] P. Pathak, A. Srinivasan, Effect of Cr substitution for Fe on the magnetic and electronic properties of electrodeposited $Co_{48.4}Fe_{21.9}Sn_{29.7}$ alloy film, Phys. Scr. PHYSSCR-147190 Under review.

Presentations in conferences:

[1] Pushpesh Pathak and Ananthakrishnan Srinivasan, Role of electrode potential in the growth of ternary alloy film by electrodeposition, International Conference on Advanced Materials and Mechanical Characterization (ICAMMC 2021), 2-4 December 2021, SRM Institute of Science and Technology, (Poster).

[2] Pushpesh Pathak and Ananthakrishnan Srinivasan, Thickness dependent structural and magnetic properties of electrodeposited Co_2FeSn Heusler alloy film, IEEE INTERMAG-2023, 15-19 May 2023, Sendai, Japan. (Poster)

[3] Pushpesh Pathak and Ananthakrishnan Srinivasan, Composition-dependent structural and magnetic properties of electrodeposited Co-Fe-Sn Heusler alloy film, International Conference on Magnetic Materials and Applications (ICMAGMA-2023), 4-6 December 2023, Hyderabad. (Oral)

****